Forschungszentrum Karlsruhe
Technik und Umwelt
Wissenschaftliche Berichte
FZKA 5806

Tests on Fast Heating for the Regeneration Process of ITER Cryopumps

Chr. Day, B. Kammerer, A. Mack

Hauptabteilung Ingenieurtechnik
Projekt Kernfusion

Oktober 1996

Forschungszentrum Karlsruhe
Technik und Umwelt
Wissenschaftliche Berichte
FZKA 5806

Tests on Fast Heating for the Regeneration Process of ITER Cryopumps

Chr. Day, B. Kammerer, A. Mack
Hauptabteilung Ingenieurtechnik
Projekt Kernfusion

Forschungszentrum Karlsruhe GmbH, Karlsruhe
1996

Forschungszentrum Karlsruhe GmbH
Postfach 3640, 76021 Karlsruhe

ISSN 0947-8620

ABSTRACT

Within the framework of the European Fusion Technology Programme, a primary vacuum pump for the ITER reactor is being developed. As the tritium accumulated by the pumps must be limited, short pumping cycles are necessary and as a consequence to that regeneration times of about 4 min only are required by the intermittently working cryopumps; approximately 60 s are available for the heating process from LHe temperature (4.2 K) to LN_2 temperature (77 K).

Methods for fast heating were tested in component tests. The heating tests were performed at the TITAN test facility. According to the basic planning, the LHe-cooled panel consisted of seven flow channels in quilted design (500 x 350 mm^2); the detailed planning meanwhile showed that a smaller numbers of channels per panel will be sufficient. The panel was mounted in a LN_2-cooled rig, which worked as first pumping stage. After having worked out a screening study comprehensive test series with three different heating methods were performed.

At first fast heating using infrared radiation was investigated. The energetic coupling turned out to be too weak and the thermal inertia of the heating rods was found to be too high in order to ensure short regeneration cycles.

Good results were obtained with forced flow of warm helium gas in the cooling channels of the panel; the panel was driven at flow rates up to 5.5 g/s and elevated pressures up to 13 bar. Depending on the position of the temperature sensor, heating times of less than 50 s were determined.

Another method of fast heating was realized using resistance heaters, which were directly installed on the panel surface. Electric output was maximum 3 kW. It could be shown that even with reduced power of 2 kW, short heating times of less than 30 s were reached without any difficulty.

It could be demonstrated by these studies that fast regeneration of ITER cryopanels using appropriate methods is feasible and technical problems appear to be solvable. The electrical heating technique combines high flexibility and a very good controlling performance.

Tests zum schnellen Heizen für die Regeneration von ITER-Kryopumpen

---

KURZFASSUNG

Im Rahmen des 'European Fusion Technology Programme' werden Arbeiten zur Entwicklung einer Primärvakuumpumpe für den ITER-Reaktor durchgeführt. Weil das in den Pumpen akkumulierte Tritiuminventar begrenzt werden muß, sind kurze Pumpzyklen nötig. Somit ergeben sich für die diskontinuierlich arbeitenden Kryopumpen Regenerationszeiten von nur ca. 4 min; davon stehen für die Heizung von LHe-Temperatur (4.2 K) auf LN_2-Temperatur (77 K) etwa 60 s zur Verfügung.

In Komponententests wurden dazu schnelle Heiztechniken getestet. Die Versuche fanden in der Anlage TITAN statt. Wie im ursprünglichen Konzept festgelegt, wurde als Testgegenstand ein aus 7 Strömungskanälen bestehendes LHe-gekühltes Panel in 'quilted design' (500x350 mm^2) verwendet. Im weiteren Planungsfortschritt ergab sich inzwischen, daß Panels mit weniger Kanälen ausreichen. Das Testpanel wurde in einer Umgebung bei LN_2-Temperatur eingebaut, die als erste Pumpstufe wirkt. Nach dem Erstellen einer Vorstudie wurden ausführliche Testreihen mit drei verschiedenen Heizverfahren durchgeführt.
Zunächst wurde die schnelle Erwärmung mit Infrarotstrahlung untersucht. Hier erwies sich die Ankopplung als zu schwach und die thermische Trägheit der Heizstäbe als zu groß, um kurze Regenerationszyklen zu gewährleisten.
Gute Ergebnisse wurden zum einen bei erzwungener Strömung mit warmem He-Gas in den Kühlkanälen des Panels erzielt. Dabei wurden Durchsätze bis etwa 5.5 g/s bei erhöhten Drücken bis etwa 13 bar gefahren. Abhängig von der Position des Meßfühlers wurden typische Aufheizzeiten unter 50 s ermittelt.
Zum anderen wurde die schnelle Erwärmung durch Widerstandsheizelemente erzeugt, die direkt auf der Paneloberfläche angebracht waren. Die elektrische Leistung betrug maximal etwa 3 kW. Es konnte gezeigt werden, daß schon mit einer reduzierten Heizleistung von 2 kW problemlos Heizzeiten kleiner 30 s erreicht werden.

Die Untersuchungen belegen, daß die schnelle Regeneration von ITER-Kryopanels bei Verwendung geeigneter Heizmethoden technisch problemlos zu bewerkstelligen ist. Die elektrische Methode verbindet eine hohe Flexibilität mit einer sehr guten Regelbarkeit.

Contents **Page**

1 Introduction

Within the European Fusion Technology Programme, the Karlsruhe Research Center (FZK) has been charged with the development of a vacuum pumping system. For the International Thermonuclear Experimental Reactor (ITER), a fusion machine of tokamak type, a reliable high-speed vacuum pump system is required to perform leak-testing, condition the torus walls and evacuate the torus during the various operation modes foreseen. The ITER requirements are highly demanding (in-vessel location at heavy thermal radiation evoking the necessity for high reliability, very high gas throughput, very large number of cycles because of the limitation of the accumulated tritium inventory) [1].

To meet these conditions, it is necessary to develop fast regeneration methods. The present report describes the development of fast heating techniques, which are part of the regeneration process for cryopanels. The cryopump concept for vacuum generation offers the great advantage of very high pumping speeds at low pressure, the achievement of extremely low final pressures and an especially clean, hydrocarbon-free ultra high vacuum, as the pumped species are confined onto the cryosurface.

Studies have been carried out in the TITAN test facility ('Tief Temperatur Adsorption', that means low temperature adsorption facility) available at FZK. The results are presented and discussed. A final recommendation for the optimum heating concept to be used for ITER is given.

2 Physical principle of cryopumping

Cryopumping presents the most direct way to produce vacuum [2]. Gas molecules hitting a sufficiently cold surface lose their kinetic energy in the collision and stick there; hence, they are removed from the gas-containing volume. The probability of sticking on the cold surface is very high and mainly depends on the surface temperature and the dominating binding mechanism. In principle, four different mechanisms can be distinguished [3]:

- Cryocondensation (sticking via phase change),
- cryosorption (sticking via physiosorption),
- cryotrapping (sticking via incorporation in porous structures, e.g. Ar frost) and
- cryogettering (sticking via chemical interaction).

The physical mechanism, which is used to solve a vacuum pumping problem, depends significantly on the kind of gas that is intended to be pumped. The ITER exhaust gas is specified only within a very broad composition range, depending on the various operation modes that are planned for ITER experiments [4]. The design relevant gas composition is related to the burn and dwell mode, leading to a gas mixture that consists up to 90 mol-% of deuterium and tritium. Besides that, large fractions of He and Ne must also be pumped. On a 4.2 K LHe-cooled surface (boiling point of He at atmospheric pressure), all relevant gases can be pumped by condensation, except for He itself. The ultimate pressure is determined by the sublimation pressure of the gases. In Figure 1 the sublimation pressure curves for four gas species, which are most difficult to pump by phase transition, are shown.

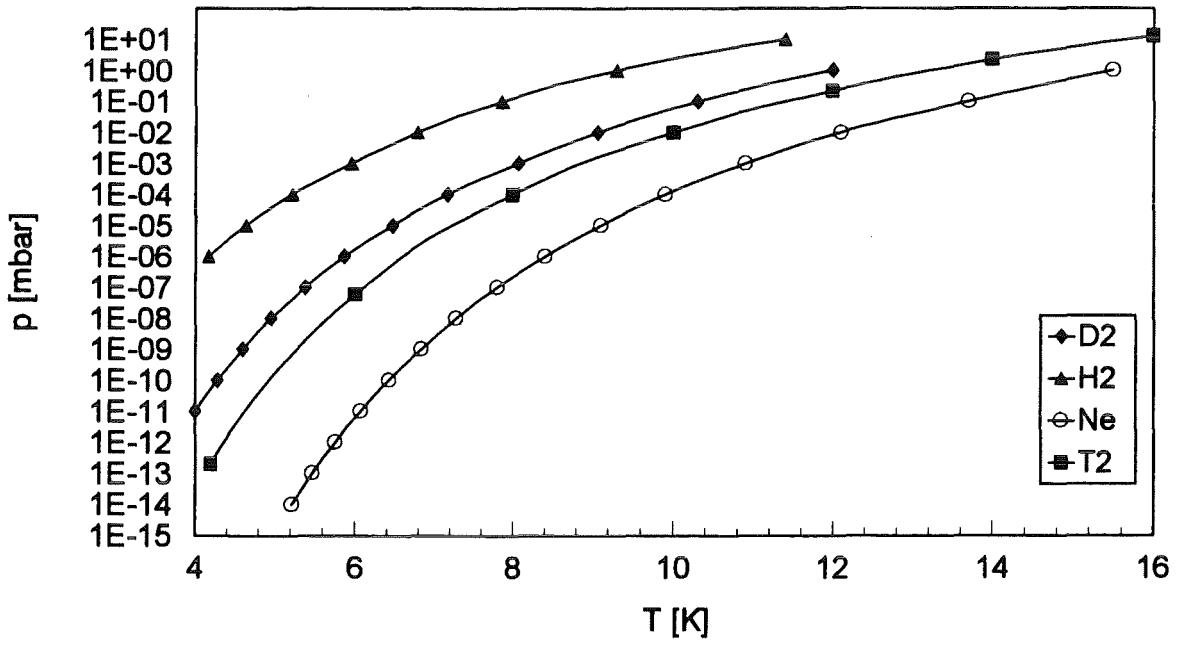

Figure 1: Sublimation pressure curves for cryogenic gases. Data taken from [2, 5].

If He shall be pumped or if lower equilibrium pressures shall be reached (for H_2 for example), a second physical concept has to be used in addition. For this purpose, the cryogettering mechanism is not applicable. It is based on chemical interaction and does not work for chemically inactive gases like He, Ne or Ar [2, 6, 7]. In a comparative study we investigated cryosorption on various sorbent materials [8, 9] and cryotrapping on Ar frost [10], finding out that cryosorption on activated charcoal is a feasible technique for pumping He and supports the pumping of other gases

(especially H_2), too. By a combination strategy of cryosorption and cryocondensation, equilibrium pressures for He and H_2 of 10^{-9} mbar (referring to a LHe-cooled surface) have been measured at the TITAN facility.

As mentioned above, the pumping performance depends significantly on the temperature of the cryosurface. During the growing of a solid layer, condensed gas on the panel leads to an increasing resistance to heat transfer from the LHe inside the panel, the surface temperature is continuously rising. Consequently, the pumping speed of the panel becomes worse and finally the desired values for the ultimate pressure in the vessel cannot be attained any more. The pumping speed also vanishes when the sorbent active sites are fully covered. At this level of operation the cryopanel is loaded at its saturation capacity and has to be regenerated. Within the regeneration process the cryopanel is heated to achieve a sufficient thermal gas release and the pumped gas is removed by backing pumps. Finally, the panel is cooled down again and, thus, the cryopump is ready to be used for the next pumping period. Because of this working principle, cryopumping is definitely a batchwise process.
To overcome this drawback, an intelligent pumping concept has been developed for the ITER machine. The technical background of this strategy shall be discussed in the next section.

3 Cryopump concept and technical objective

For torus exhaust pumping of ITER, N=16 cryopumps with cyclic regeneration have been selected which are located in the divertor ports of the torus. A schematic representation is given in Figure 2. Together with a set of mechanical forepumps, they constitute the ITER torus primary pumping system.
The cryopumps will be required to operate in the following modes [4]:

- Evacuation of the torus to high vacuum, following cross over from the torus roughing pumps,
- pumping of the torus during bake-out, conditioning and burn,
- evacuation of the torus during dwell and
- pumping of the torus during leak testing.

However, the main function of the cryopumps is the pumping of all hydrogen isotopes and helium plasma exhaust. Contrary to the conventional cryopump performance, which is limited by the charcoal saturation capacity, the operation of the ITER cryopumps is limited to a gas load much less than saturation for reasons of safety.

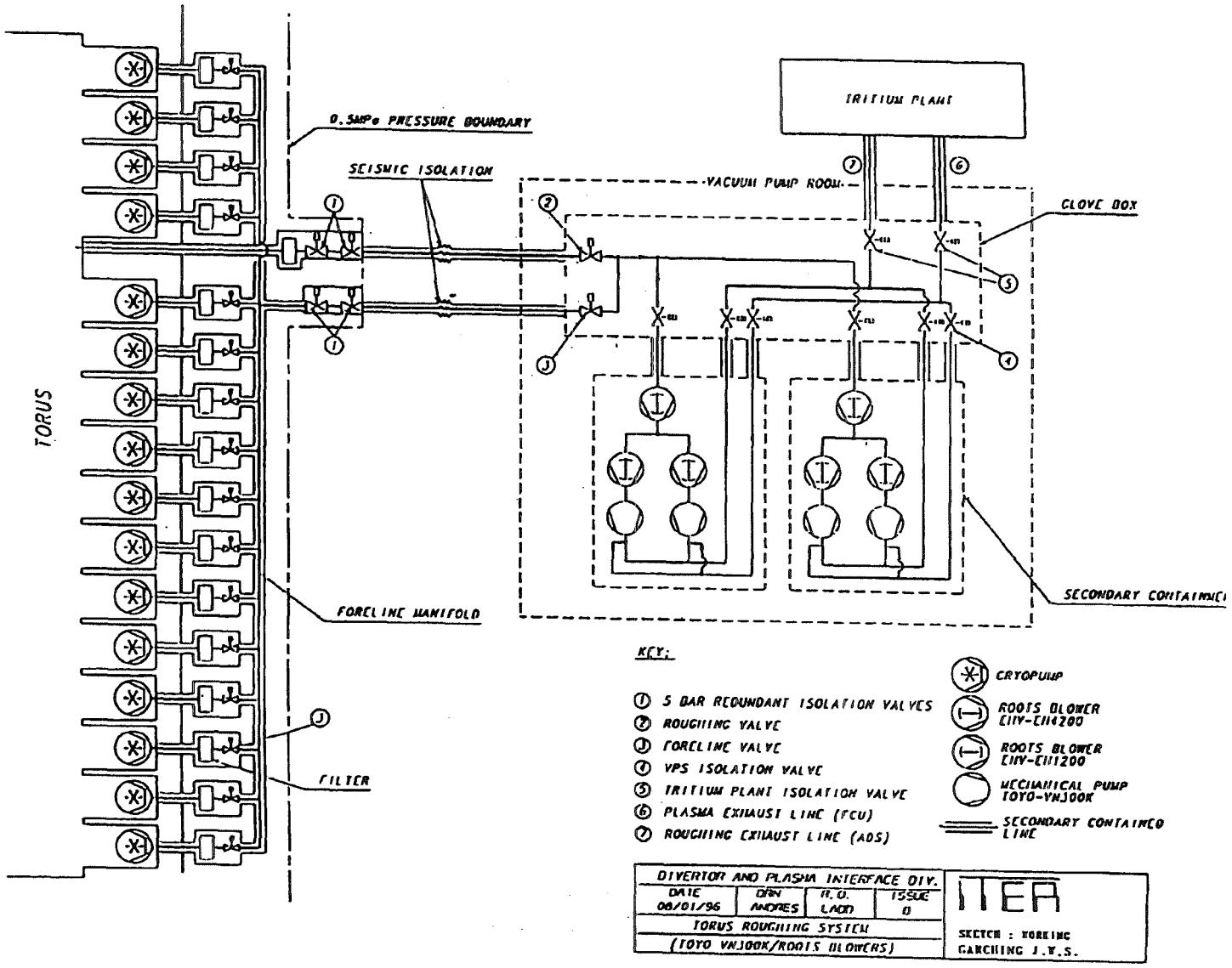

Figure 2: Schematic view of the torus and the cryopump location (taken from [1])

This limit gas load is determined by the maximum allowable tritium inventory (MALTI) in the whole cryopump system. MALTI is specified to be less than 140 g. The design point is 100 g.

Figure 3 illustrates that this limits the total cycle time of each pump and causes a large number of pumping cycles. According to the pumping strategy, which is currently in discussion [11], a maximum of P=12 pumps shall be available for pumping, the remaining (N-P)=4 being in regeneration or stand-by. Pumps will be taken off-line sequentially for regeneration. The staggering interval a between the intermittent use of the pumps is 62.5 s. Under these assumptions the resulting regeneration time t_R is 250 s, the pumping time t_P equals to 750 s. The pumps will be regenerated via the torus roughing pumps. A detailed discussion and the exact derivation of the numbers can be found in [12]. As shown in Figure 3, a quasi-continuous cryopumping mode is achieved within the operation concept outlined above.

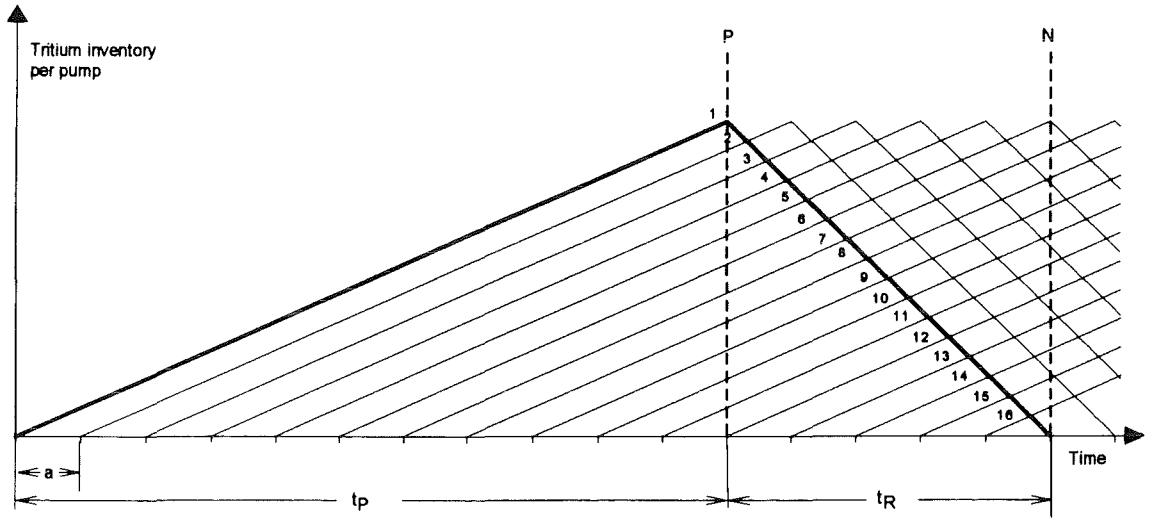

Figure 3: Staggered operation of cryopumps.

According to this strategy, the mechanical forepumps must perform the pump-down of just one cryopump every 62.5 s. In this time interval, they have to reduce the pressure to the cross-over pressure, which has been specified with 10^{-1} mbar. Starting from this point, the cryopumps have to be able to pump quantitatively and to reduce the pressure down to operation pressure of approximately 10^{-3} mbar.

The relevant operational steps, which have to be managed within the regeneration period, are summed up in Table 1.

Table 1: Operational steps in the cryopump regeneration phase.

Operation	**Time scale**
1) Closing of the valve to the divertor (to isolate the pump from torus)	10 s (full stroke) [4]
2) Heating up the panel (4.5 K --> 90 K)	?
3) Thermal gas release[1]	20 s
4) Pumping down the released gas	62.5
5) Cooling down the pumping panel [2]	90 s [14]
6) Opening of the valve to the divertor (to reconnect the pump with torus)	10 s (full stroke)
TOTAL	required: < 250 s

If every single step has to be done separately, there are only 57.5 s left for fast heating of the panels. Nevertheless, it may be promising to start the pump-down within the heating phase, thus, starting at lower pressures and resulting in a shorter pump-out time. On the other hand, the heating process is supported by higher pressures, which allow for the heat transfer from the 80 K shielding via molecular gas conduction. The detailed operation situation has to be evaluated in an optimisation calculation and verified by tests.

However, in the present report we want to focus on the heating methods that allow heating within 60 s. The choice of an optimum fast heating strategy is the subject of the present study.

[1] The time to remove the gases strongly depends on the amount of gas and on the procedure as to how it is removed. In our case, the time scale of 20 s is estimated using thermal desorption data from literature for protium, which is expected to desorb most slowly [13]. However, provided other (i.e. tritiated) species are not trapped or inhibited from desorption by protium, we may accept incomplete regeneration of protium.

[2] At the time, discussions are under way to reduce the time specified for cooling to 60 s [11].

4 Screening study: Decision for possible heating methods

In the open literature various heating methods for conventional cryopumps are described. They are used for cryopumps cooled with one- or two-stage Gifford McMahon refrigerators. An overview is given in [15].
The simplest one is the natural warm-up regeneration. The LHe supply is switched off and the warm-up of the panel occurs by thermal radiation from the surrounding which is usually driven at LN_2, i.e. at 77 K. After reaching the equilibrium temperature of phase transition or desorption, the gas is released and the pressure in the vacuum vessel starts to rise. Then, heat transfer via convection and gas conduction leads to a faster warm-up.
This principle can be supported by injection of purge gas. An inert gas is led into the pump to accelerate the natural heating process. The principal disadvantage of this concept is the time necessary for the roughing down after the regeneration process and the additional load on the following tritium-plant. Besides, the regeneration quality is poor, as desorbed gas species, which usually are prevented from hitting the charcoal by using a LN_2-cooled baffle, adsorb at the coal at relatively high partial pressures. However, it may be useful, because of the dilution effect of the pumped gas species, which might be toxic or explosive.
None of the conventional methods meet our requirements as far as heating time is concerned. They result in regeneration times in the magnitude of some hours. The shortest regeneration time for a commercially available cryopump was about some tens of minutes [16].
Operational experience from other fusion machines, e.g. the JET pumped divertor cryopump system [17] in Abingdon, UK or the DIII-D Divertor cryopump system [18] in San Diego, USA is not useful for fast regenerating cryopumps; there, the cryopumps could be operated for some days without regeneration. Just recently, Gouge et al. reported about a continuous regeneration technique of Ar frost cryopumps [19]; they also made some feasibility considerations concerning rapid regeneration techniques for conventional cryopumps, but could not present experimental data [20].

Therefore, as a first step, a concept study had to be made to investigate various techniques for fast heating of a cryopanel. The paramount criteria are:
- Low mass,
- high heat input,
- compatibility with magnetic fields, n- and γ-radiations and low-temperature operation,

- high efficiency (only surface heating of the charcoal, no bulk heating of the panel as a whole) and
- possibility of selective heating.

The results of this study were described in detail in [12]. Within the selection and optimisation process, various contactless techniques (bare wire heating at some distance close to the panel surface, glow discharge heating, microwave heating, inductive heating) had to be rejected, because they turned out not to be feasible. We decided to investigate in more detail the following three methods:

- Infrared heating,
- convective heating via forced warm He gas flow through the cooling channels of the panel and
- electric heating elements fastened on the panel surface.

Consequently we decided to carry out series of experiments to assess the practicability of these three different techniques. For this purpose we used the TITAN facility, which is described in the following section.

5 Description of the TITAN test facility

The experimental facility used and the procedures were described in detail in [12]; only an outline will be given here.

5.1 Recipient

The test panel with 80 K shielding is installed in a cylindrical vacuum vessel of 700 mm diameter and 2200 mm height; a view of the vertical cross-section is given in Figure 4. The free volume was experimentally determined to be 760 l. It can be baked up to 200 °C by trace heating.

The bottom part of the vessel is designed as a measuring dome in compliance with the PNEUROP guidelines [21]. They contain a standard procedure ('steady pressure method') to derive the pumping speed from defined measurements of throughput and pressure [3]. To fulfil these, the gases are metered into the lower part of the vacuum vessel via a tube with 70.3 mm inner diameter.

---

[3] In this report, the physical property throughput, which plays a key role in vacuum technology, is defined as pV product at standard temperature of T_0 = 273.15 K. The corresponding molar flow rate is $\dot{n} = (p \cdot \dot{V}) / (R \cdot T_0)$ with the universal gas constant R=8.3145 J/mol/K. The pumping speed of a vacuum pump is defined as a volume flow rate at T_0 and suction pressure p.

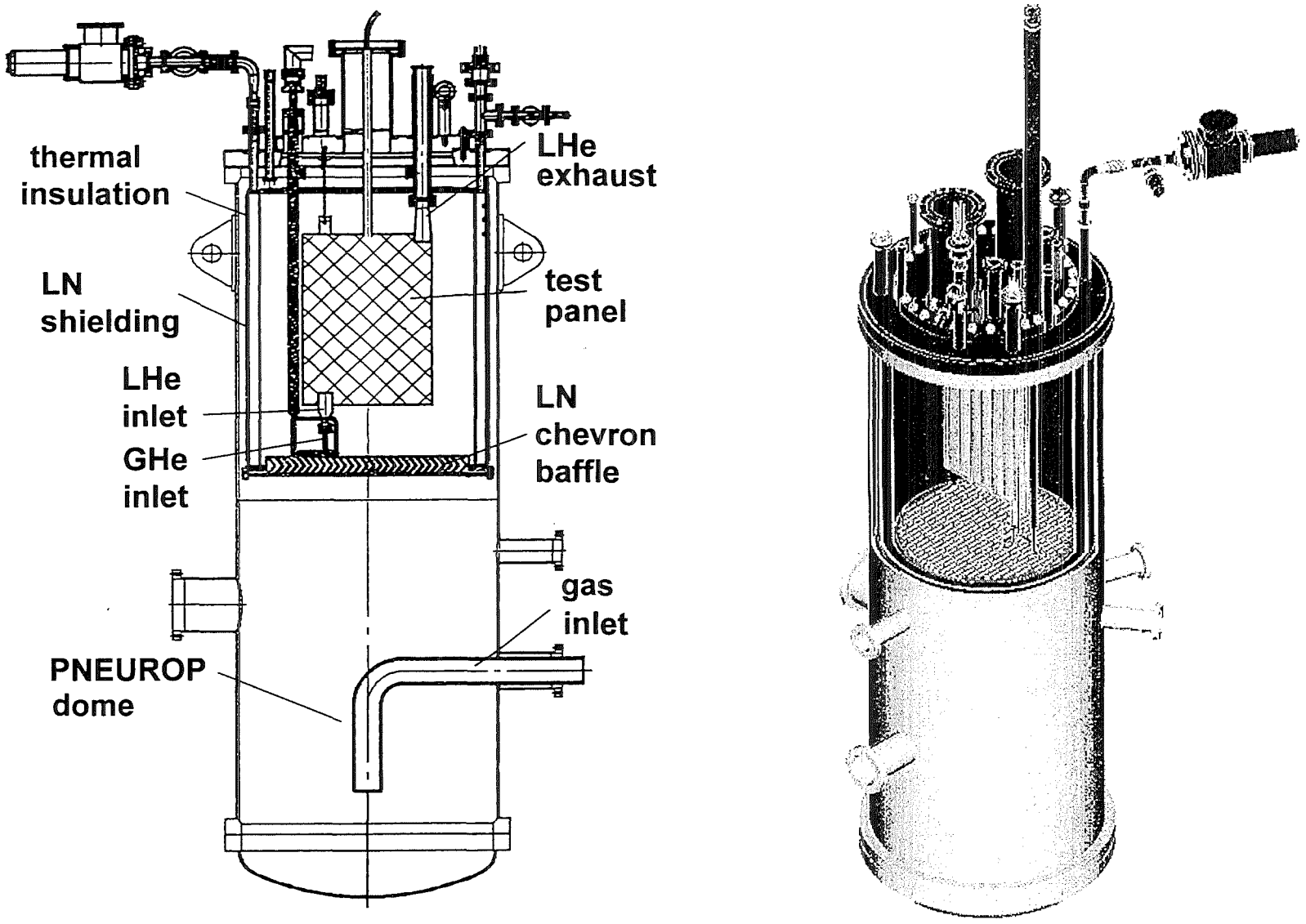

Figure 4: TITAN facility (cross-section and 3D drawing).

Dosage rates from $2.5 \cdot 10^{-2}$ mbar·l/s to 16.9 mbar·l/s (at 0°C) can be set up with three mass flowmeters connected in parallel (see chapter 5.6.3). Nozzles for cryogen supply and evacuation lines as well as measuring cables are provided on the vessel lid. Special flanges (CF160) are reserved for accommodation of the infrared heater elements. The flanges on the sheath surface serve for gas dosage, connection to the vacuum pump set, sampling for mass spectrometry and installation of pressure meters.

5.2 Vacuum pump set

The auxiliary mechanical pumping system used for the evacuation of the TITAN facility consists of a turbomolecular pump with a capacity of 500 l/s (BALZERS TPU 5105), backed by an oil-sealed rotary vane pump of 60 m^3/h capacity (BALZERS DUO 030A). Oil vapour is prevented from backflowing by means of a condensate separator (BALZERS KAS 040) and a catalyser trap (BALZERS URB 040).

5.3 Cryogen supplies

The TITAN facility is supplied with liquid nitrogen from a stationary LN_2 storage tank via a vacuum insulated transfer line. Liquid helium is supplied from a dewar transport vessel having a volume of 450 l.
It should be noticed that for ITER the use of supercritical He (critical pressure of 0.23 MPa) is planned. This mode cannot be simulated in the TITAN facility, as no stationary supply is possible. Nevertheless, the heating method finally applied for ITER will be tested in the model cryopump, which is currently being installed in the TIMO facility (Test facility for ITER model pumps) at FZK [22].

5.4 Test rig and panel

The cryopump consists of two pumping stages. The first one is a LN_2 pool-cooled 106° chevron baffle, made of copper and blackened (opening diameter 527 mm, baffle thickness 50 mm, wall thickness of the V-profiles 3 mm, pitch 19 mm). The baffle is screwed to the bottom of a cylindrical annular LN_2 recipient and kept at 80 K by heat conduction. Towards the top, the 80 K volume is covered by a copper plate.

The second stage is the LHe forced-flow cooled panel itself. It is installed in the centre of the 80 K volume. The panel is made in quilted design using SS plates (Comp. L'Air Liquide, Sassenage, France). The design of the panels used is illustrated in Figure 5. The panel comprises 7 flow channels[4] in quilted geometry. Prior to installation in TITAN, the panel is coated with a sorbent on both sides, thus, yielding a total pumping area of 0.35 m^2. As sorption material we used activated carbon (type SCII, mean particle diameter 1 mm mesh size (sieved), Comp. Chemviron, Brüssel), which is bonded to the panel surface using inorganic cement with high thermal conductivity (Thermoguß 2000, Comp. Klebchemie, Weingarten). About 300 g carbon is necessary to coat the panel on both sides (thickness about 1 mm). The choice of the optimum material combination and the development of an automatic coating device was one of the objectives of an earlier research project [23]. According to the currently discussed concept for the ITER prototype cryopump, panels following this quilted design shall be used as basic modules to achieve the necessary total pumping area of 8 m^2 [22, 24].

For the tests two similar panels were used, both following the same geometry, but equipped with different temperature sensors. The positioning of the sensors is illustrated in Figure 6.
The first one (denoted 'Panel I', blank panel weight 4.6 kg incl. flanges, additional charcoal mass 286 g) was used for the tests with IR radiation and forced warm He gas flow. To monitor the temperature distribution across the panel, various sensors were used. At the coated surface, seven Fe-Rh temperature sensors were bonded with special cement of high thermal expansion coefficient (type Polytec 906, comp. POLYTEC, Waldbronn) onto one side of the steel substrate panel. The panel is illustrated in Figure 7. Additionally, two further sensors were installed on the inlet and outlet tube, respectively. For comparison a fast responding thin-film resistance temperature sensor (CERNOX) (see chapter 5.6.2) was also fixed to the panel outlet flange, near to the position of the Fe-Rh sensor. In order to obtain some information about the LHe level inside the panel, one more Fe-Rh sensor was immersed into the LHe hold-up inside the outlet flange. To be able to evaluate quantitatively measurement errors caused by radiation from the 80 K environment, the temperature sensors T142, T145 and T147 were shielded with three layers of aluminium foil. The temperature sensors are placed in a way that both the panel edges, which are expected to have the greatest time lag, and the situation directly at the flow channels can be monitored.

[4] Within the detailed planning phase of the ITER vacuum system, it was meanwhile worked out, that panels with a smaller number of channels should be preferred. The results discussed in the present report are not significantly influenced from this geometry.

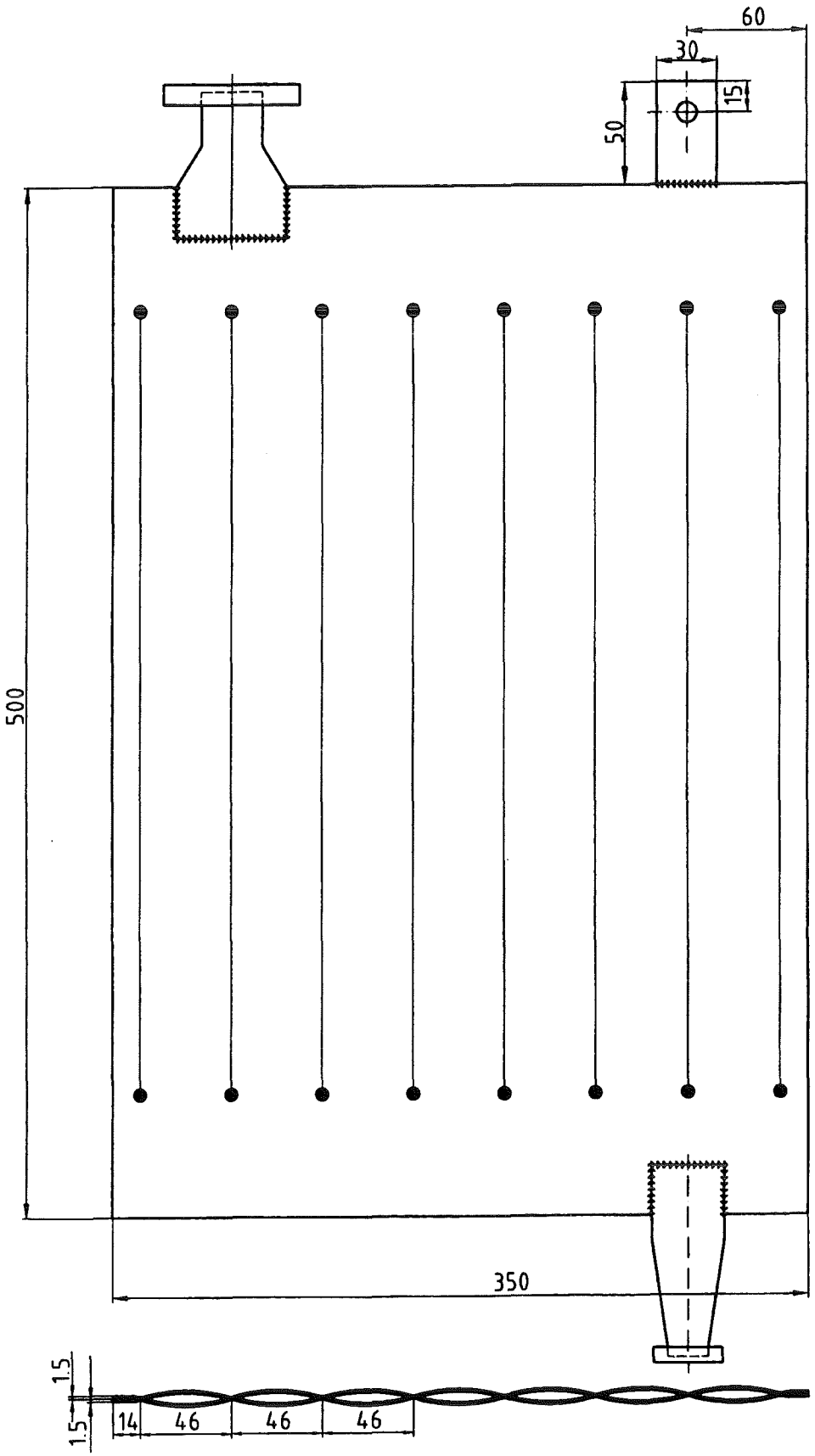

Figure 5: TITAN test panel in quilted design.

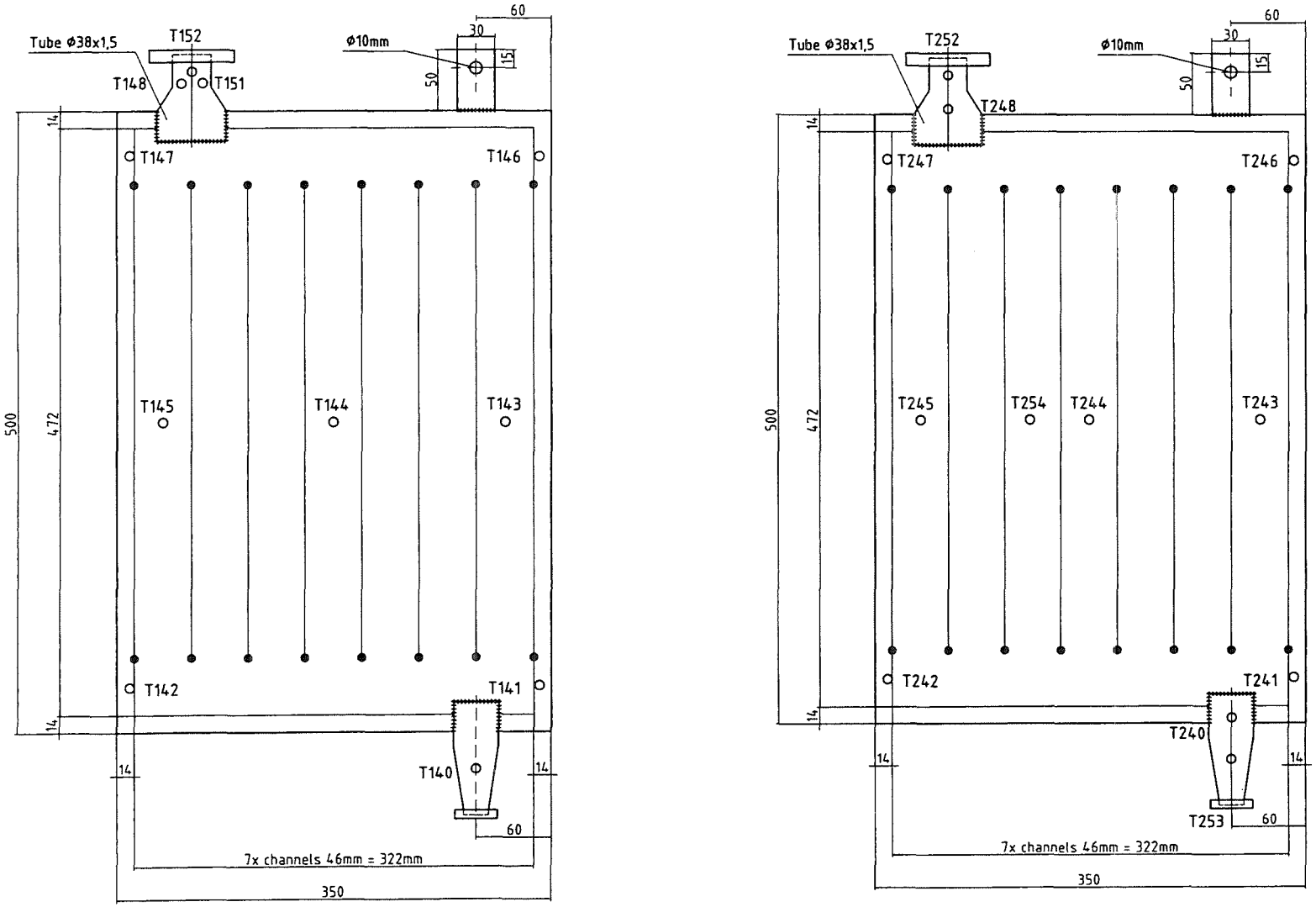

Figure 6: Location and nomenclature of the temperature sensors on the test cryopanel. On the left, the panel I used for investigations with infrared radiation and warm forced He gas flow is shown; on the right, the panel II used for investigations with warm forced He gas flow and electrical heating is illustrated.

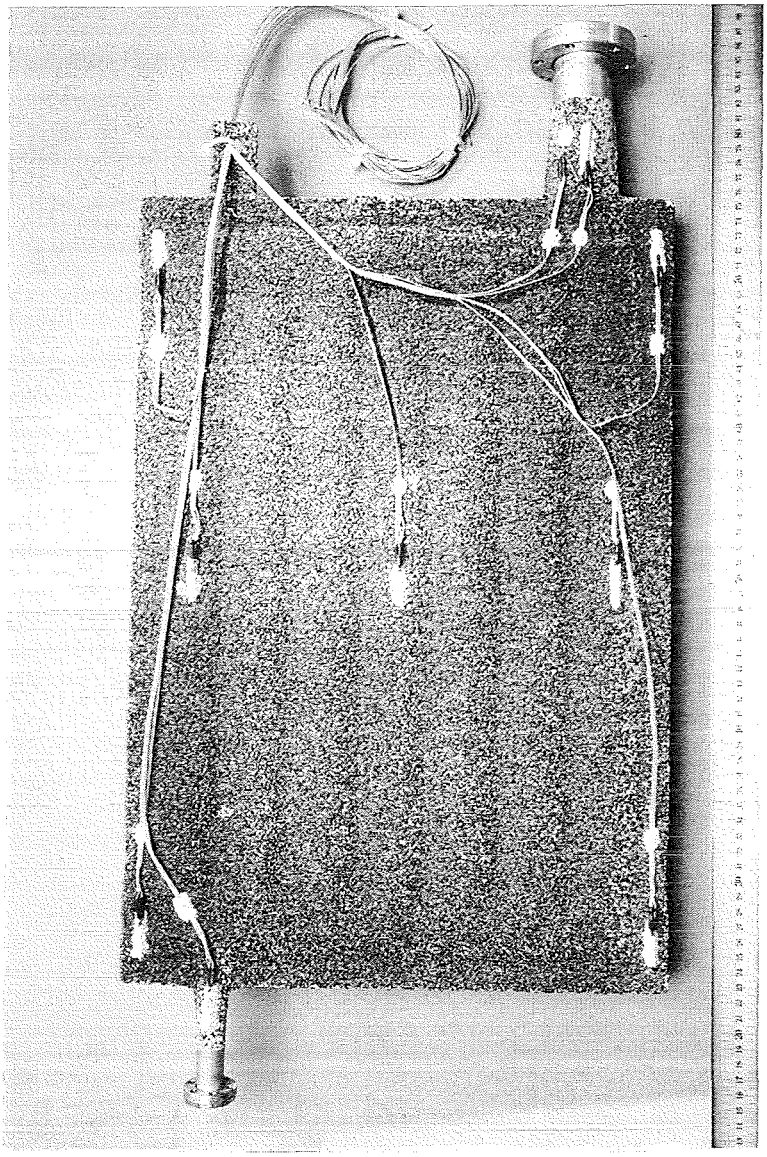

Figure 7: Test panel I.

The second panel (denoted panel II) was used for some tests with forced GHe flow and all the electrical heating tests. It was manufactured after the first test runs with panel I. Consequently, first performance results could be considered in order to work out a somewhat refined design. A few manufacturing steps had to be done in advance. At first, the electrical resistive heaters and the thermocouples for controlling were fixed onto the steel substrate using SS straps (see Figure 8). In a second step the whole panel was subjected to electrolytic copper coating (about 400 µm thickness) to ensure a homogeneous temperature profile. Due to this treatment, panel II is almost 2 kg heavier than panel I. A photography of the panel in this stage of manufacturing is shown in Figure 9.

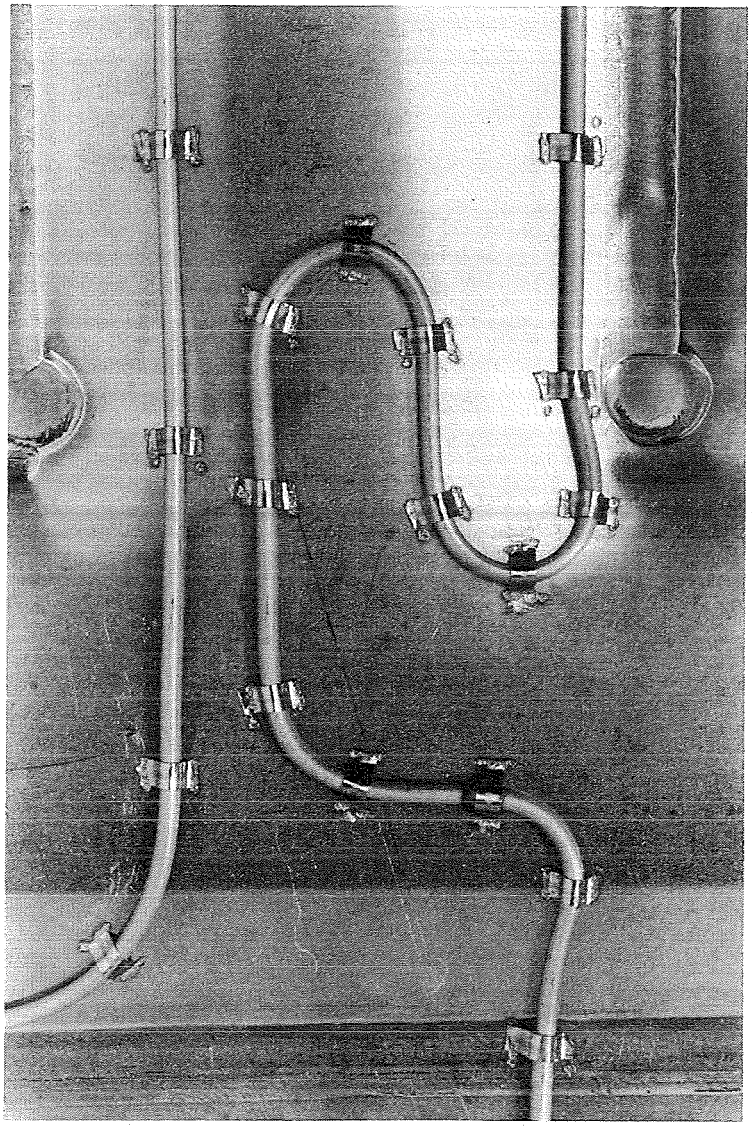

Figure 8: Illustration of the fastening technique used for the electric heaters.

The whole surface was then coated with activated charcoal (327 g carbon mass in total). The location of the measurement sensors is indicated in Figure 6b. The central measuring position at the panel surface was additionally equipped with a fast responding silicon diode (see chapter 5.6.2). All the sensors at the panel surface were shielded against thermal radiation (Figure 10), using three layers of aluminium foil. Finally, a Fe-Rh sensor was also placed inside the inlet tube.

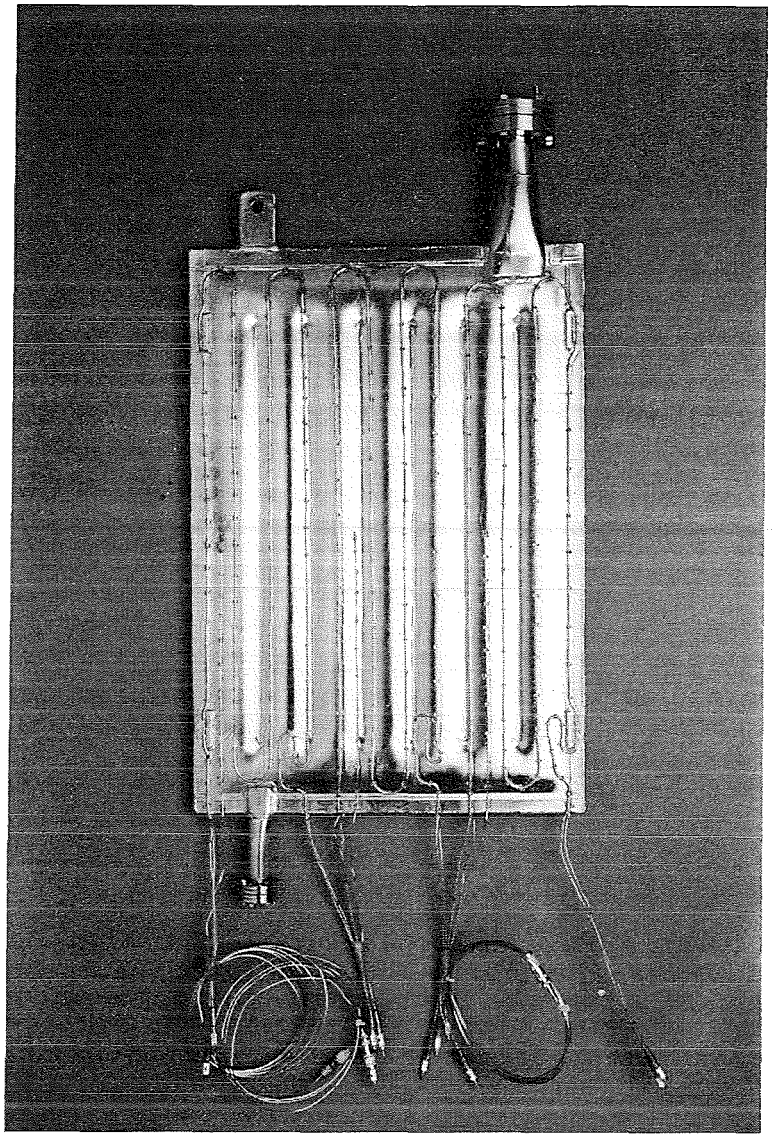

Figure 9: Test panel II (electrolytically coppered), before coating with activated charcoal.

To achieve a reliable and reproducible controlling procedure for active LHe cooling, ensuring very short response times, we used a manual actuation of the LHe transfer line valve at a fixed gas overpressure of about 300 mbar in the LHe dewar vessel. We also tried an indirect automatic control loop using the mass flow of evaporated He as leading property. In this case, the time lags were too long to attain a stable control loop.

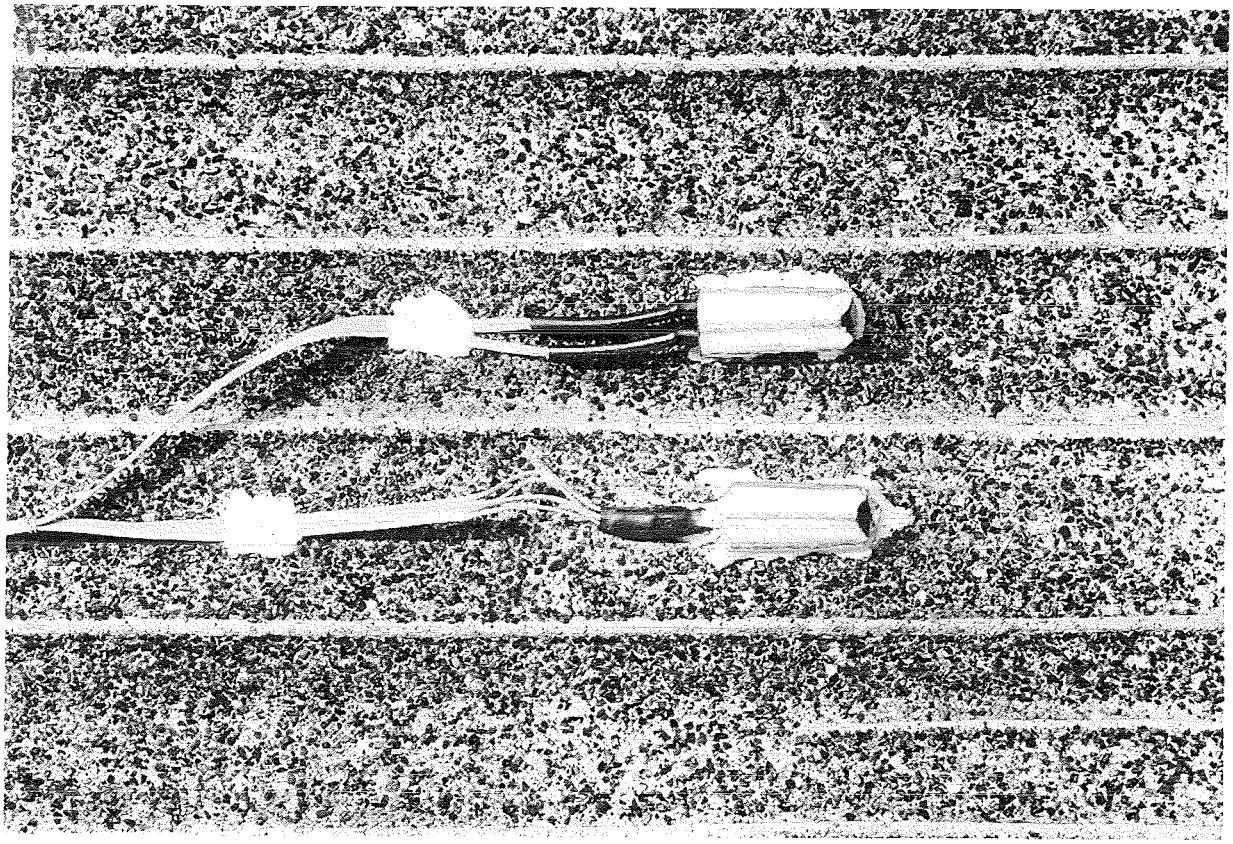

Figure 10: View of the thermal radiation shielding of the temperature sensors.

5.5 Panel heating

The necessary heat consumption can be estimated from the panel mass to be heated (ca. 5 kg), the necessary temperature range (5 to 90 K) and the time range (about 60 s). The mass theoretically also includes the amount of frozen gas. However, a scale-down of ITER conditions to TITAN yields a final gas load of approx. 6700 mbar·l (at 273.15 K), which equals (in the case of pure D_2 pumping) to only 1.8 g. This is of negligible magnitude as is the heat of desorption or desublimation and the enthalpy of evaporation and superheating of the LHe hold-up.
Thus, for heating from 5 to 90 K about 40500 J, corresponding to 670 W (relating to a heating time of 60 s) have at least to be generated within the heating process. Taking into account the heat losses and to consider a certain safety margin, approximately 1 kW has to be installed.

5.5.1 Infrared heating

On each side of the panel an IR heater rod (outer diameter 9.5 mm) was installed (Comp. Etirex Chromalox, Soissons, France). The geometric configuration is shown in Figure 11. The distance to the panel is 140 mm. The active heating length is 450 mm. On the side not facing the panel a reflector sheet is fixed by clamping which reflects onto the panel the radiation from the rear side of the heater. The temperature of the heater can be controlled by a NiCr-Ni thermocouple embedded in the insulating mass (magnesium oxide). Each heater has an installed electrical power of 500 W at a supply voltage of 230 V. The emission coefficient of the Incoloy 800 tube is 0.7 - 0.8. The view factor was calculated to be about 80%. More details are given in [12].

5.5.2 Warm gas heating

Warm gas heating is an available alternative to IR-heating. For this, a 6x1 mm pipe is welded onto the LHe inlet nozzle, through which helium gas from a compressed gas cylinder at ambient temperature can be supplied (via a pressure reducer) to the coolant channels (see Figure 4). The maximum He mass flow rate was 6 g/s at a pressure of 13 bar. The He used was of the purity 99.9999 %.

5.5.3 Electric heating

The design of the panel is illustrated in Figure 12. On each side of the panel we fastened 3 resistive heating elements (Comp. Philips-Thermocoax, Heilbronn), with two units each. One of each pair was placed at the front, the other at the back side of the panel. Each pair was controlled within one heating loop using a NiCr-Ni thermocouple as controlling sensor. The heaters were 240 cm long including 20 cm long cold ends on each side. The outer diameter of each heating cable was 1.5 mm, the ohmic resistance was about 11 Ω. Depending on the heat transfer situation at the place of installation, the electric power range between 100 and 1000 W (adjustment by variable voltages, corresponding to 33 V and 105 V potential difference, respectively) is achieved for each element.

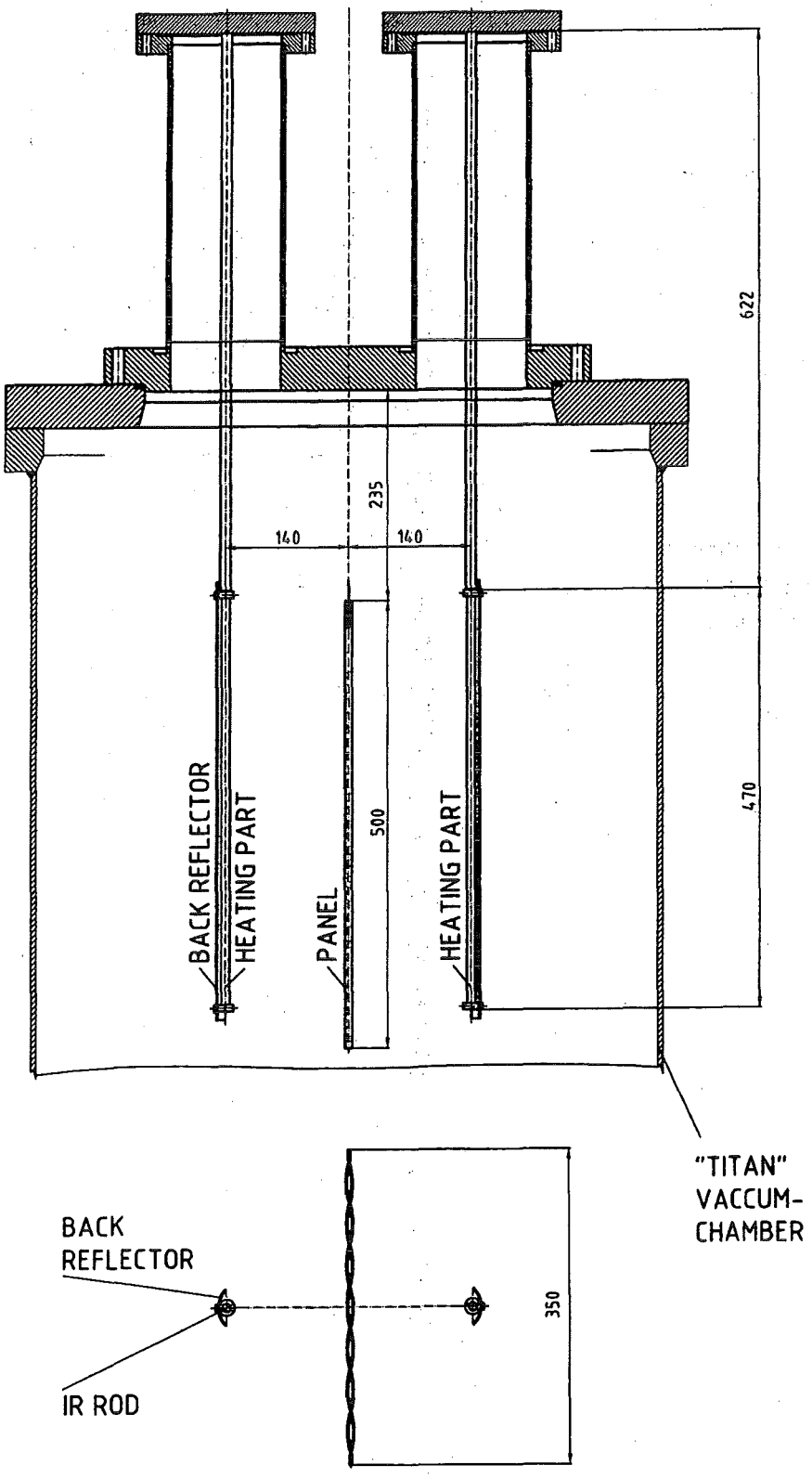

Figure 11: Infrared heater assembly.

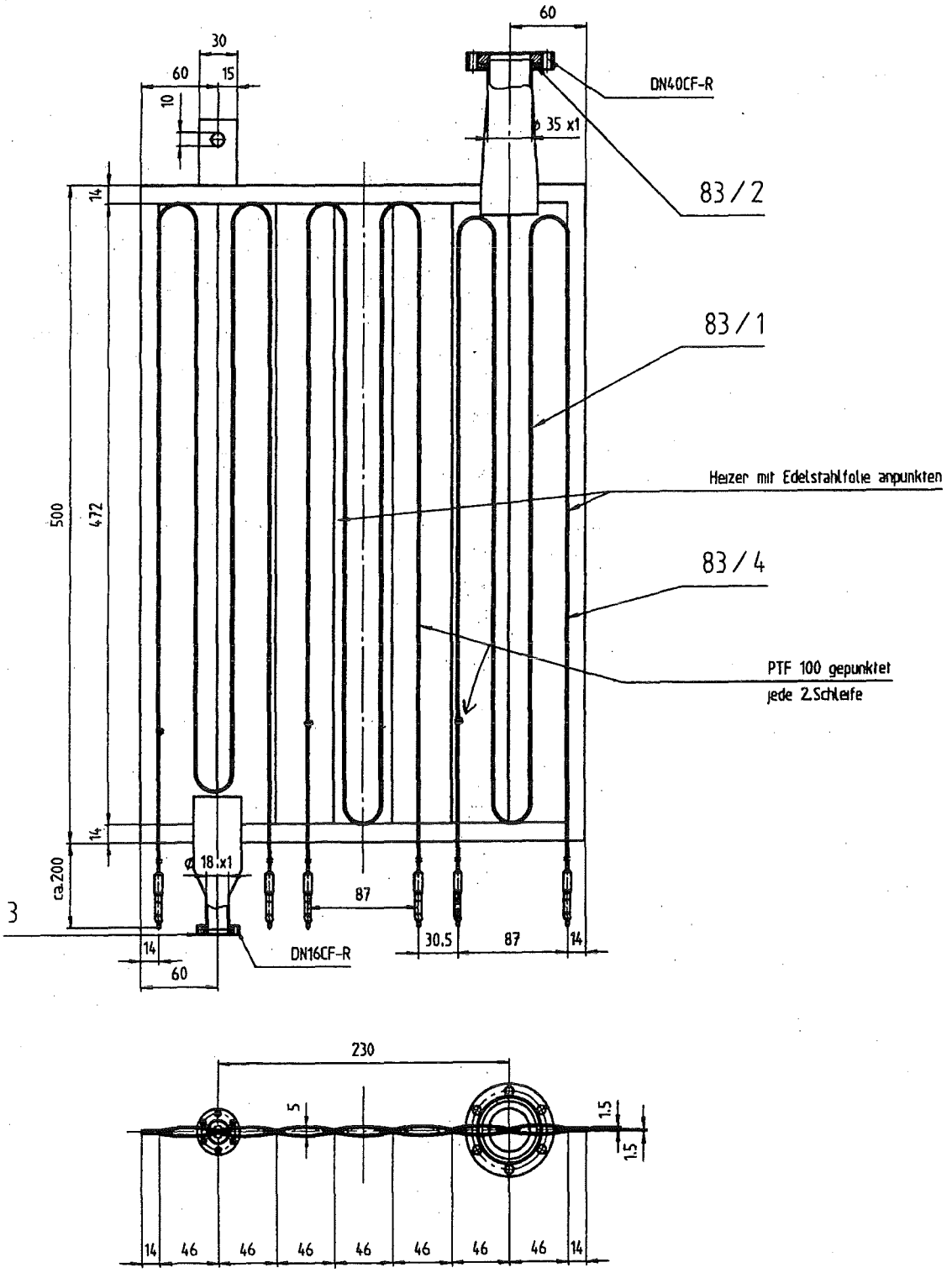

Figure 12: Manufacturing drawing of the resistive heating elements assembly at panel II.

5.6 Instrumentation

The instrumentation used is indicated in Figure 13. It shows a section of the P&I-diagram of TITAN. All the relevant in-vessel measurement sensors are presented in this chapter.
Details with respect to measurement uncertainties, error propagation and statistics can be found in [25].

5.6.1 Pressure measurements (inside the PNEUROP dome)

The range of pressures to be measured extends over 12 decades, i.e. from 10^{-9} to 10^{3} mbar; it can be covered only by use of several measuring instruments of different types. The output signals of all instruments used are dependent on the gas species, except for the capacitive manometer. For this reason, the manufacturers provided standard calibration files for all pure gases of interest. For comparison we checked these at our own calibration lab for N_2 and He. The agreement was good.

1 Hot-cathode ionisation-type pressure gauge (P225)

Manufacturer: Varian; type 890 AR, equipped with Bayard-Alpert measuring tube UHV-24, measuring range 10^{-3} to 10^{-10} mbar.

2 Gas-friction type pressure gauge (P206)

Manufacturer: Leybold, type Viscovac VM 210, with a heatable measuring head VK 200, measuring range 10^{-6} to 10^{-2} mbar.

3 Cold-cathode ionisation-type pressure gauge (P227)

Manufacturer: Edwards, type Penning 505, with measuring tube CP 25 K; measuring range 10^{-6} to 10^{2} mbar.

4 Thermal conductivity pressure gauge (P226)

Manufacturer: Edwards, type Pirani 16/501, with measuring tube PRH 10 K, measuring range 10^{-3} to 10^{3} mbar.

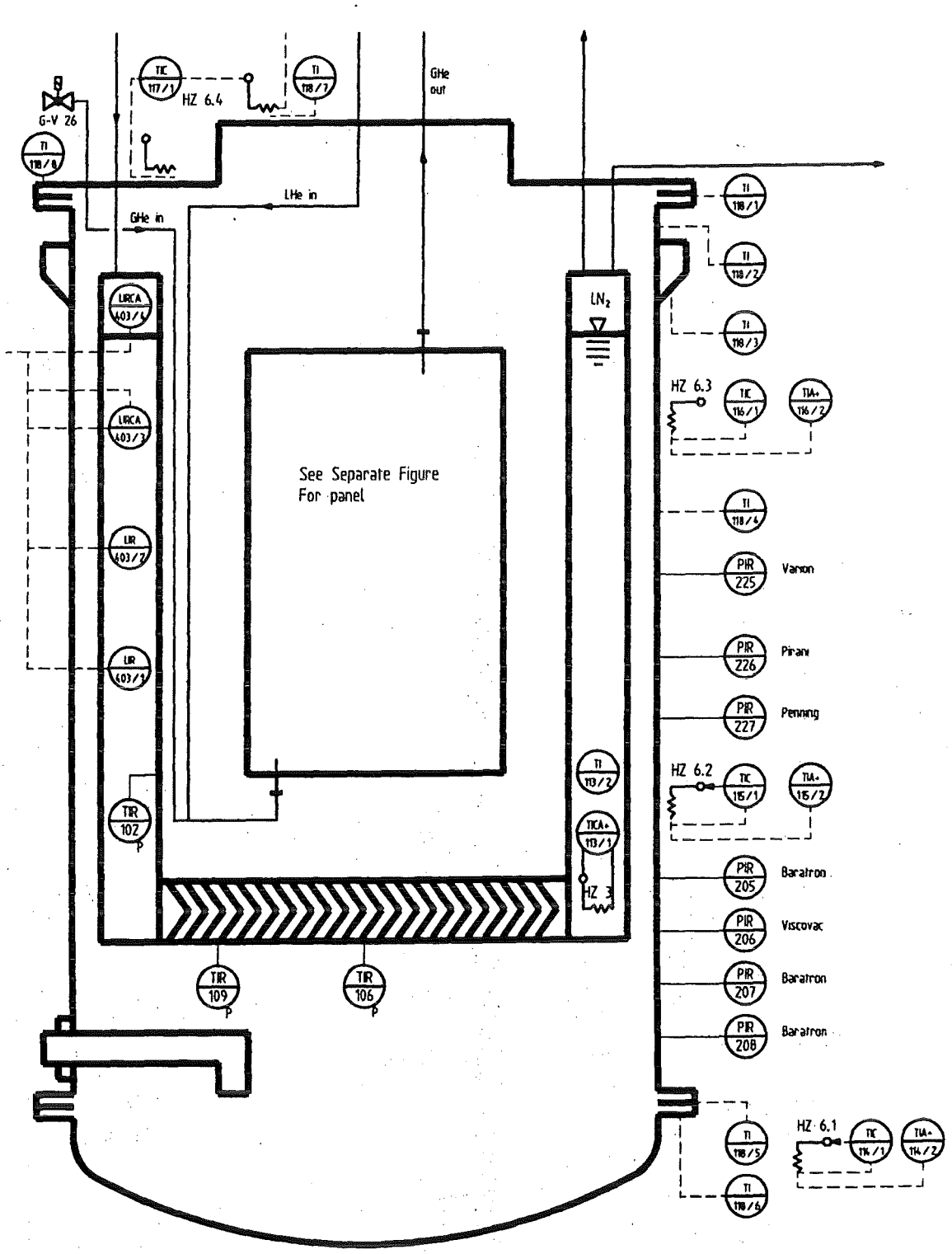

Figure 13: P&I-diagram of the TITAN vacuum recipient.

5 Capacitive manometer

Manufacturer: MKS; type Baratron 390 HA (thermostatised measuring chamber):
a) measuring range $1.3 \cdot 10^{-1}$ to $1.3 \cdot 10^{3}$ mbar (P205)
b) measuring range $1.3 \cdot 10^{-3}$ to $1.3 \cdot 10^{1}$ mbar (P208)
a) measuring range $1.3 \cdot 10^{-5}$ to $1.3 \cdot 10^{-1}$ mbar (P207)

5.6.2 Temperature measurement

The cryogenic sensors (thin-film (T151), diode (T254), Fe-Rh (all others at the panel)) are procured including calibration curves. All resistance sensors are designed in 4-lead technology. The temperatures correspond to the ITS-90 temperature scale. In the following, the relevant instrument characteristics are listed.

1 Fe-Rh resistance temperature sensor

Manufacturer: Oxford Instruments Ltd., Oxford, England via J.A.&M.M. Deegan, Heidelberg, type RhK, 27 Ω (at 0°C), cylindric geometry (3.2x20 mm), heatable to 800 K, up to 400 K without impact on calibration characteristics[5], for highest resolution operated at two different current values (2.8 mA up to T=30 K and 0.15 mA up to T=600 K), reproducibility better than 1.5 mK (short-term) or 10 mK (long-term), respectively; accuracy 10 mK (at T<27 K), thermal response time 10 s (at ambient temperature), not recommended for use in magnetic fields below LN_2 temperature, high resistance to ionizing radiation.

2 Platinum resistance sensor

Type Pt 100, 1/3 DIN tolerance A.

3 Thin-film resistance temperature sensor

Manufacturer: Lake Shore Cryotronics Inc., Westerville, USA via. Cryophysics GmbH, Darmstadt, type: CERNOX CX 1070 SD, flat rectangular disk geometry (3.2x1.9x1 mm), heatable to 325 K; stability 3 mK (short-term) and 25 mK (long-term), accuracy 5 mK (at T<10 K), 20 mK (at 20 K), 35 mK (at 50 K), 140 mK (at 300 K); thermal response time 15 ms (at LHe), 200 ms (at LN_2), 800 ms (at room

temperature), recommended for use in magnetic fields at low temperatures, excellent resistance to ionizing radiation. A comparison with other sensor types is given in [26].

4 Silicon diode

Manufacturer: Lake Shore Cryotronics Inc., type DT-470-SD, flat rectangular disk geometry (3x1.9x2.7 mm), heatable to 475 K, stability short-term 10 mK (at LHe) , 20 mK (over the whole temperature range), stability long-term 10 mK (at LHe), 40 mK (at LN_2), 25 mK (at ambient temperature), accuracy 20 mK (at T<10 K), 50 mK (at 10 to 330 K), thermal response time 10 ms (at LHe), 100 ms (at LN_2), 200 ms (at ambient temperature), not recommended for use in magnetic field applications below 60 K or in radiation environments.

5 Thermocouple

Type NiCr-Ni (K), DIN Class 3.

5.6.3 Flow rate measurement

1 Flow rate of GHe (evaporated LHe coolant)

The thermal mass flow sensing technique is especially suitable for the measurement of small and medium gas flow rates. The theory of operation is based on heat transfer. For the measurement of the flow rate of the evaporated LHe, we used instruments manufactured by the BROOKS company (via Westphal GmbH, Ottobrunn); here, a precision power supply provides a constant heat input at the heater of the sensor bypass capillary tube, which is operated in the laminar flow regime. Upstream and downstream, a temperature sensor is located. At zero flow conditions, the temperatures measured there are equal. When gas flows through the tube, the upstream sensor is cooled and the downstream sensor is heated. This temperature difference is used to measure the gas flow quantitatively. Calibration was carried out with He directly. The instrument data are as follows:
Manufacturer Brooks, type 5850; measuring range 0 to 50 and 83.3 l/min, respectively (at standard conditions T=273.15 K and p=1 atm). The measurement error is specified to be 1% (of F.S.) for directly calibrated mass flowmeter as we used it; repeatability 0.25% (of F.S.).

[5] Obert et al. [17] reported about drifts during operation of Fe-Rh sensors.

2 Dosage of mixtures (PNEUROP-Dome)

For gases and gas mixtures which the instrument is not calibrated for, conversion factors for linear flowmeters are specified by the manufacturers. However, the measurement error is distinctively greater (up to 5%), as the conversion factors are derived theoretically. It is general knowledge that these factors are not well understood and are of questionable reliability [27]. A detailed calibration study is right under way at FZK.
The dosage is realized by means of a mass flow programmer (type 147B, MKS Instruments, München) using three different scaled mass flow controllers (type 1259B, MKS) with the measuring ranges 0 to 10, 0 to 100 and 0 to 1000 SCCM, respectively. The MKS sensors are based on the same physical operation principle, but use another signal than the BROOKS instruments. They establish the temperature difference and measure the required power consumption. The achievable accuracy is specified to be 0.8% (of F.S.), the repeatability 0.2%. The sensors are mounted in a thermostated chamber, to minimize drift effects caused by changing ambient temperatures.

3 Metering of warm GHe flow for panel heating

As thermal settling time until nominal measurement accuracy takes some tens of seconds, the thermal mass flowmeters are not feasible for unstationary mass flows. Nor are they suited for large mass flows (6 g/s corresponding to $2 \cdot 10^6$ SCCM). Therefore, an indirect method has been used. For that purpose, the pressure decrease in the high pressure supply cylinder (known volume) during the GHe flow has been registered as a function of time. By use of an appropriate equation of state for He [28], the mass flow can easily be calculated. The evaluation procedure is described in annex A.

5.7 Data acquisition and processing

Measurement data of all relevant quantities are continuously registered and stored by an automatic device. It takes place three times per second for 64 analog differential inputs. The voltage values are digitised subsequently. Then, the average for 5 s is taken for each measured quantity. The rough data obtained in this way are stored together with 33 digital input signals. They are converted into physical data referring to the calibration tables available. The resulting physical data are also

stored. In addition, they are displayed online on a colour monitor of the system and, at the same time, 25 m away in the control station. Depending on the type of gas used, the calibration tables for gas dosage can be selected directly at the computer of the control station.

6 Experimental results

In this section, the experimental results for the different heating methods are presented and discussed. The general objective was to study panel heating curves at a parametric variation of the power of the heat source. To investigate the influence of pressure (i.e. the impact coming from an additional heat transfer mechanism, the molecular gas conduction) as well, we performed tests both with bare panels (no frozen gas at the panel surface, at $p=10^{-8}$ mbar) and with loaded panels (panel surface covered with a full-cycle gas load[6], corresponding to ITER conditions achieving a final specific gas load of 1.9 (mbar·l)/cm^2, start pressure $p=10^{-3}$ mbar and very rapid increase during heating up to about 5 mbar). For experimental reasons, the effective gas load during the ITER operation can very much differ from the nominal value.

6.1 Concept of temperature measurement

To draw correct conclusions from the experiments, the temperature measurement must be studied in some detail.

As described above, we used two different panels, both equipped with a matrix of Fe-Rh sensors and one additional sensor each (thin-film sensor with panel I, Si diode with panel II). We decided to base our prime measurement strategy on the Fe-Rh sensor, as it is the only commercially available sensor, which is both usable above room temperature (for bake-out at 120 °C) and within ionizing radiation. The greatest drawback is the cylindric shape, which may cause contact problems with plane surfaces, and the long thermal response time. Both effects may cause erroneous temperature measurement results.

Contact problems for steady-state operation are not considered to be very important; as long as we can demonstrate that the panel is filled with LHe, the surface

[6] We used a gas mixture representative for ITER burn and dwell operation mode (tritium has been replaced by deuterium), consisting of: 3 mole% He, 1.12 mole% CH_4, 1 mole% H_2, 0.16 mole% O_2, 0.16 mole% CO, 0.16 mole% N_2, 0.08 mole% CO_2, 0.08 mole% Ar, Rest D_2.

temperature results only from the heat transfer resistance through the steel, the charcoal, the bonding cement and the frozen gas. In this case, the real surface temperature can be estimated to be about 5 to 5.5 K [24]. The contact situation could be very much improved if a flat disk sensor would be used. From Comp. LakeShore, a Fe-Rh bare chip version is available. We tested this sensor type, but it was very much affected by the cement material, such that it could not be used as a reliable instrument.

To investigate the influence of thermal contacting for our own measurements, typical results (mean temperature and corresponding scatter) at low temperature steady-state operation are listed in Table 2 (see Figure 6 for nomenclature). It is shown that the temperature averages differ remarkably, but the random errors of the various sensors are comparable.

Table 2: Statistical data (mean temperatures T and standard deviation σ) at low temperature steady-state operation. Sensors with radiative shielding are marked with (S). All sensors are Fe-Rh type, except for T151 (thin-film resistive sensor) and T254 (Si diode). The measurement sample comprised about 180 values, corresponding to 15 min steady-state operation.

Panel I:

Sensor	T140	T141	T142 (S)	T143	T144	T145 (S)
T [K]	8.01	7.90	6.51	7.80	7.20	6.04
σ [mK]	39	33	35	71	37	69

Sensor	T146	T147 (S)	T148	T151 (TF)	T152	
T [K]	8.50	7.16	9.73	5.64	4.48	
σ [mK]	50	37	57	41	41	

Panel II:

Sensor	T240 (S)	T241 (S)	T242 (S)	T243 (S)	T244 (S)	T245 (S)
T [K]	10.75	10.04		9.75	7.66	11.72
σ [mK]	23	17		51	10	25

Sensor	T246 (S)	T247 (S)	T248 (S)	T252	T253	T254 (D)
T [K]	7.88	10.87	12.77	4.22	4.28	6.24
σ [mK]	8	11	85	14	33	32

The values for the sensors directly immersed in LHe (T152, T252, T253) demonstrate that they work well. All surface sensors are subjected to the same radiative heat input from the 80 K environment. The Fe-Rh-measured temperature for panel I varies between 6 and 8.5 K, for panel II between 7.7 and 11.8 K. The indicated temperature variation is first of all due to the sensors itself, caused by the disadvantageous contact situation between the convex sensor geometry and the concave quilted panel channel geometry. As secondary influence, a conductive heat flux through the outlet tube has to be considered (T148 gives the highest temperature at panel I, T 248 at panel II, respectively). The impact of the contact situation in our case can be worked out, if the measurements of two different sensor types (one with good contact situation, one with bad contacting) at almost the same location are compared: T148 with T151 (ΔT=4 K) and T244 with T254 (ΔT=1.2 K).
The thermal conductance between sensor and panel surface (which should be infinite for an ideal measurement situation) depends on the individual fastening situation and may vary from sensor to sensor. In current heat transfer literature [22, 30], several empirically-based theories exist for calculation of heat flux through single contact spots. Incorporating these ideas in the evaluation process of the temperature measurement may enable us to derive the real temperature from the measured value. However, they are very difficult to apply to our geometry, especially when the influence of the contact cement (unknown material properties) also must be considered. Calculations are right under way though.

Another conclusion to be drawn from Table 2 concerns the influence of radiative shielding, as the shielded sensors at panel I give the lowest temperatures of all Fe-Rh surface sensors. This was the reason why we equipped all sensors at panel II with radiation shields. Nevertheless, the measured temperatures at panel II were distinctively higher. This may be partly attributed to the electrical heaters, which are connected with ambient temperature via the electrical feedthroughs. Although the wires were thermally anchored, they work as an additional conductive heat source. However, this influence cannot be separated properly from the contact problem as discussed above.

At this level of interpretation, it must be decided which sensor is the one that should be referred to in a quantitative manner. In this respect, we have to consider that we are not interested in the sensor itself, but only using the sensor as a tool to obtain information about the charcoal; the charcoal temperature is the thermodynamically interesting temperature for adhesion of the molecules hitting the surface. As the sensor is not small enough to be fully embedded in the charcoal layer of about 1 mm

thickness, it is contacted with the panel wall material and thus also affected by the substrate temperature. In this regard, the measured temperatures are only an indication of charcoal temperature, not an exact determination. This is one more reason for accepting the drawbacks described above. In annex B it is demonstrated that the sensors with three layers of radiation shielding can be compared satisfactorily with the situation at the charcoal.

The question of thermal response behaviour of the sensors is discussed in section 6.5 as part of the comparison between the diode and the Fe-Rh sensors in the dynamic heating performance.

6.2 Efficiency of thermal insulation

In Figure 14 the temperature curves are given as they result from natural warm-up. In the time range illustrated in this Figure the steady-state base temperature is also considered.

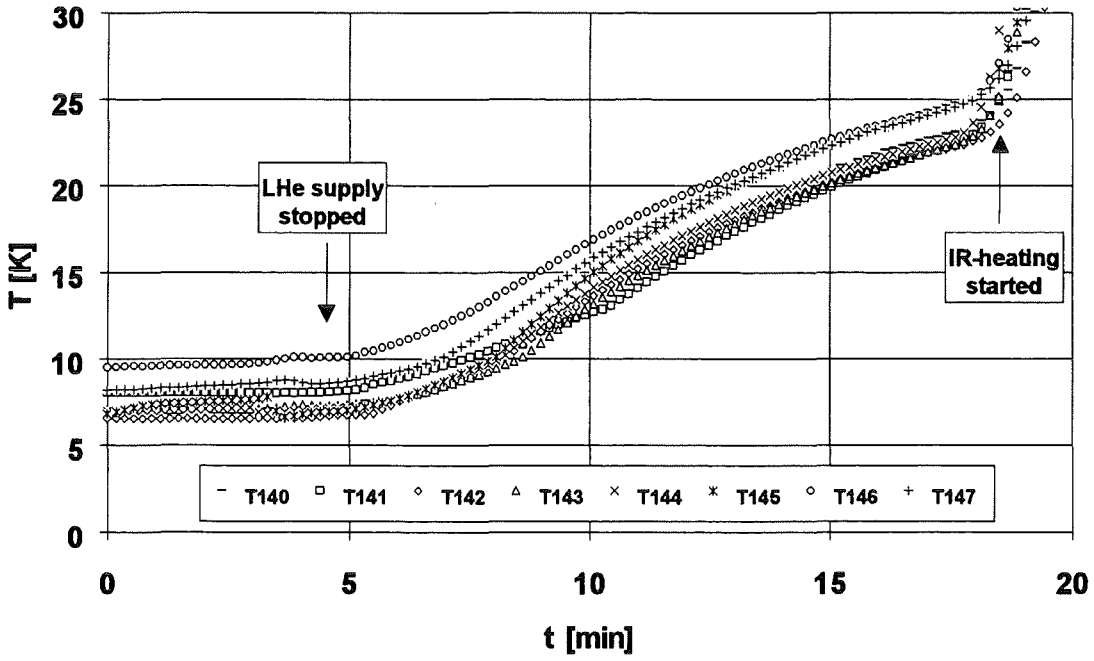

Figure 14: Natural warm-up of the cryopanel.

The time needed for heating from 10 K to 20 K is, quite uniformly, about 7 min. Considering the panel weight of about 5 kg, this results in a heat flux of approx. 1.0 W. This value is comparable with the results derived from a theoretical study [31]. The heating curves show a directed order: The panel is systematically warmed up starting from the top of the panel (T146, T147), the bottom of the panel is heated the slowest (T141, 142). This can be explained by the mechanism underlying heating. At the operation pressure of about 10^{-8} mbar during this natural heating experiment, heat transfer by convection or molecular gas conduction can be neglected. Radiative heat transfer from the LN_2 surrounding would cause symmetrical heating, whereas heat conduction through the cross-section of the outlet tube (38x1.5 mm) is the only mechanism to cause a directed heating. Even the steady-state performance is partly influenced by this heat input.

Anyway, the impact of unwanted heat transfer can be neglected (1.2 W compared to 1 kW and more).

6.3 Infrared (IR) heating

In Table 3 an overview of the experiments made is given. The impact of IR radiation was investigated at two different temperatures.

Table 3: Test matrix for the heating tests using IR radiation.

Test run #	Topic to be investigated
1	Taking into operation of the heaters: heating at ambient temperature
2A, 2B, 2E	Heating of the cold panel after switching off the LHe supply; heating via radiation and conduction from 80 K surrounding (see Figure 14)
2C	Heating of the cold panel with IR heater at 200 °C
2D	Heating of the cold panel with IR heater at 400 °C

Heating performance

The heating curves measured for two different IR heater temperatures are shown in Figures 15 and 16; the first one corresponds to a heater temperature of about 200 C, the second to 400 °C. The temperature increase measured by the themocouples inside the IR heaters was determined to be very fast (about 130 K/min).
It becomes obvious that the temperature distribution across the panel surface is very inhomogeneous. The steepest temperature increase is being measured at the panel centre with T144. With all other sensors, remarkably longer heating times were obtained. Here, the influence of the thermal radiation shielding becomes very important. An intercomparison of shielded sensors (right panel side T142, 145, 147) and the group of unshielded ones (T141, 143, 146) reveals that in both cases the upper half of the panel is being heated a little bit faster than the lower half. The inhomogeneity increases with rising heater temperature. For 400 °C heater temperature, a time lag of about 40 s is measured by the shielded sensor, the value recorded by the unshielded sensors is about 10 s. The differences between position 144 and 143 resp. 145 indicate a strong angle dependency of the thermal IR radiation.
The impact of thermal radiation is illustrated in Figure 17. Here, the temperature difference between the unshielded and the shielded sensors for each symmetric combination (see Figure 6) is plotted for the two heating experiments (ΔT_1 =T147-T146, ΔT_2 =T145-T143, ΔT_3 =T142-T141). Consequently, the difference ΔT_1 at the upper side of the panel is smaller than at the other panel parts and the magnitude of the ΔT itself is remarkably greater than in the unheated state (see Table 2).

To ensure a reliable pumping operation without charcoal poisoning the whole panel must be heated to the upper regeneration temperature desired. Thus, the longest time measured should be considered the relevant heating time. Table 4 indicates the relevant time range. Obviously, the necessary times of less than 60 s are not achieved at all. This is possibly due to the fact that the absorption behaviour of solid DT is very bad at the wavelength of the IR transmitter. For a detailed evaluation, more information about the absorption properties of frozen gas is needed; literature data are very scarce [5, 19, 32].

Another disadvantage of the IR heater technology, i.e. high thermal inertia, shall be discussed in the next section.

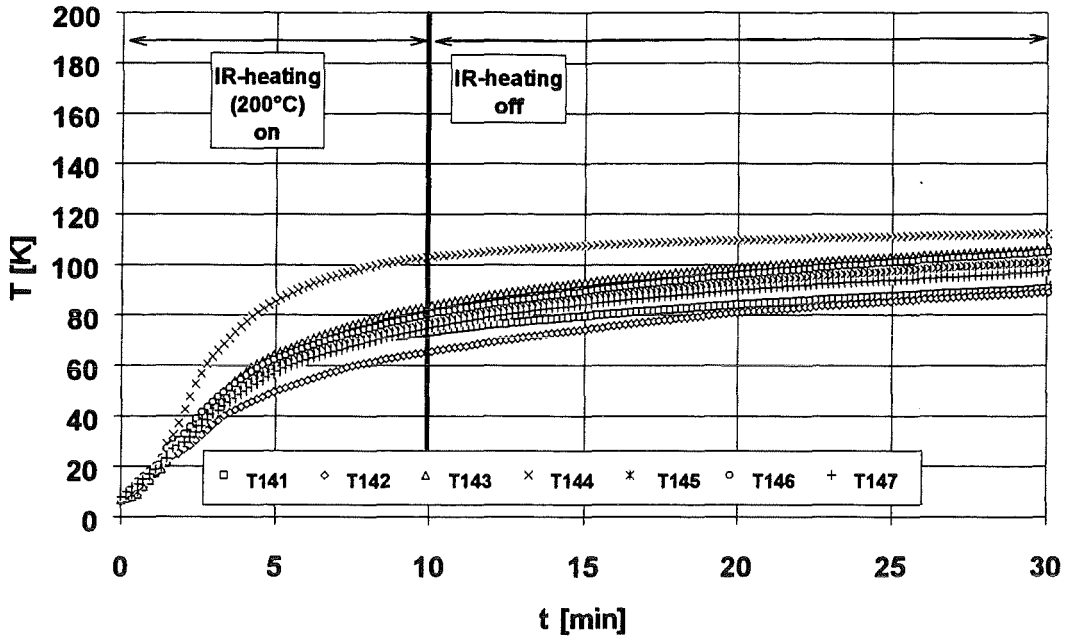

Figure 15: Heating curves at IR radiation at 200 °C.

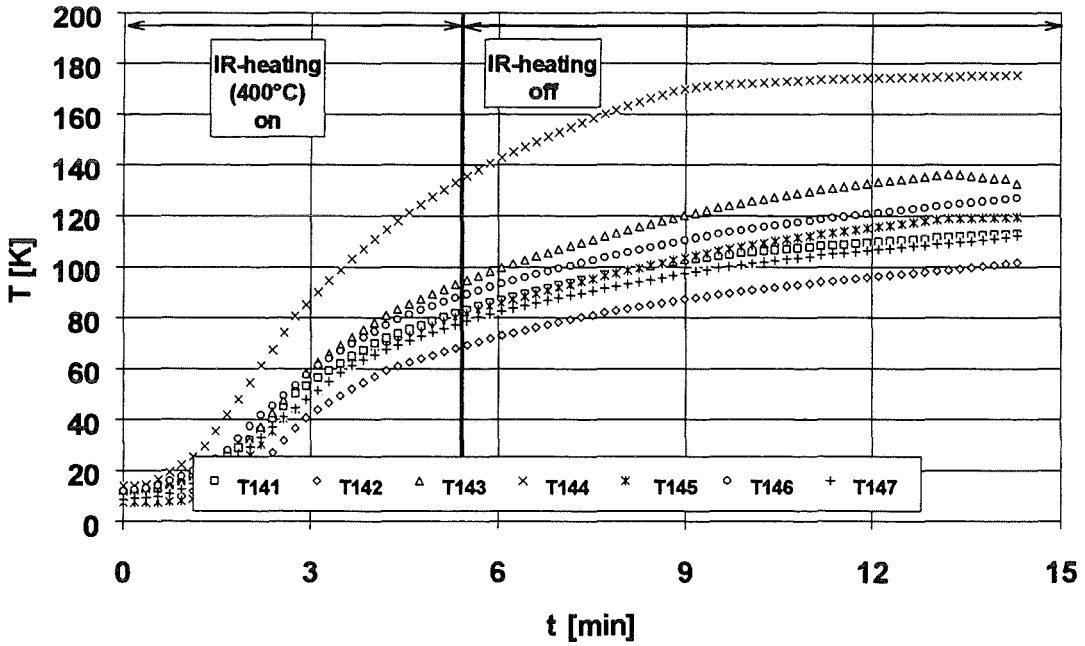

Figure 16: Heating curves at IR radiation at 400 °C.

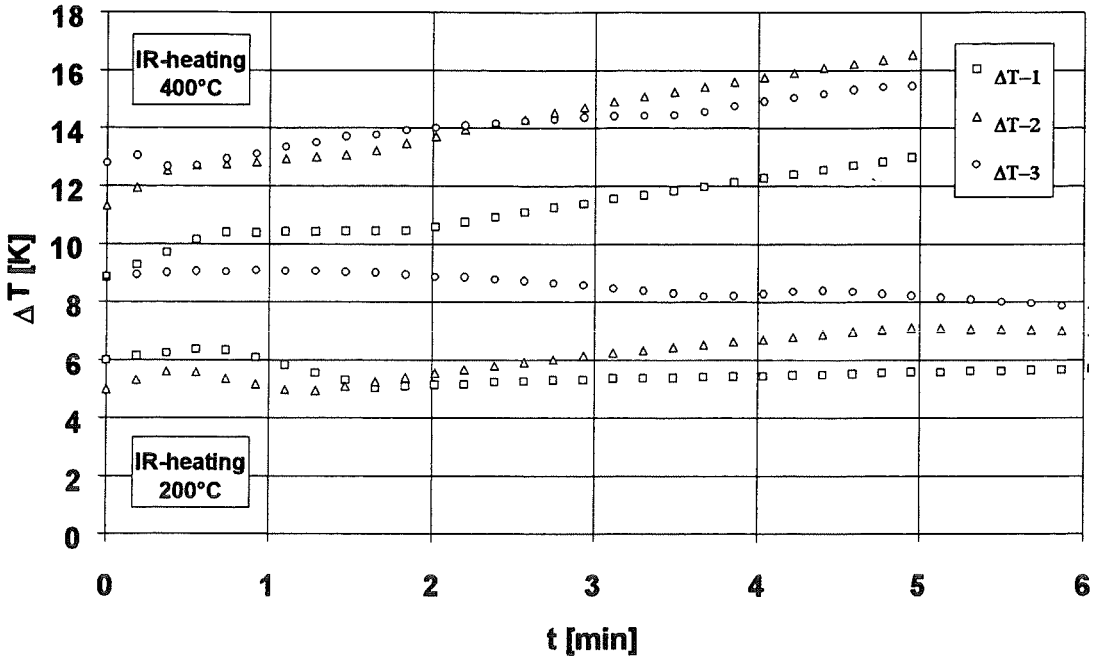

Figure 17: Comparison of the temperature difference between bare and shielded sensors at three defined position levels (ΔT_1 =T147-T146), ΔT_2 =T145-T143, ΔT_3 =T142-T141) and at two radiative expositions.

Table 4: Heating times up to 80 K in min. The heater was active during 10 min (at 200 °C) and 5.5 min (at 400 °C), respectively.

IR operation	T144 (fastest)	T147/T145 (middle)	T142 (slowest)
IR radiation at 200 °C	4.3	12 (extrapolated)	very long
IR radiation at 400 °C	2.7	5.7 (extrapolated)	very long

Cool-down behaviour

If the heater has once been warmed up, i.e. if it has been used once, the time required for cooling down is very large. But low-temperature steady state can only be achieved at the panel if the energy impact coming from the heater almost vanishes. This situation is examplified in Figure 18. There, the cool-down performance of the panel, characterised by the central panel position (T144) and the edge position (T147), is compared for three different IR heater conditions: Cold heater, heater cooling down from 200 °C (rod temperature between 130 °C at t=0 and 90 °C at t=25 min) and heater cooling down from 400 °C (rod temperature between 300 °C at t=0 and 130 °C at t=25 min). The experimental result is due to the active radiation arising from the IR heaters, as they do not cool down fast enough. They cannot transport their energy through the vacuum.

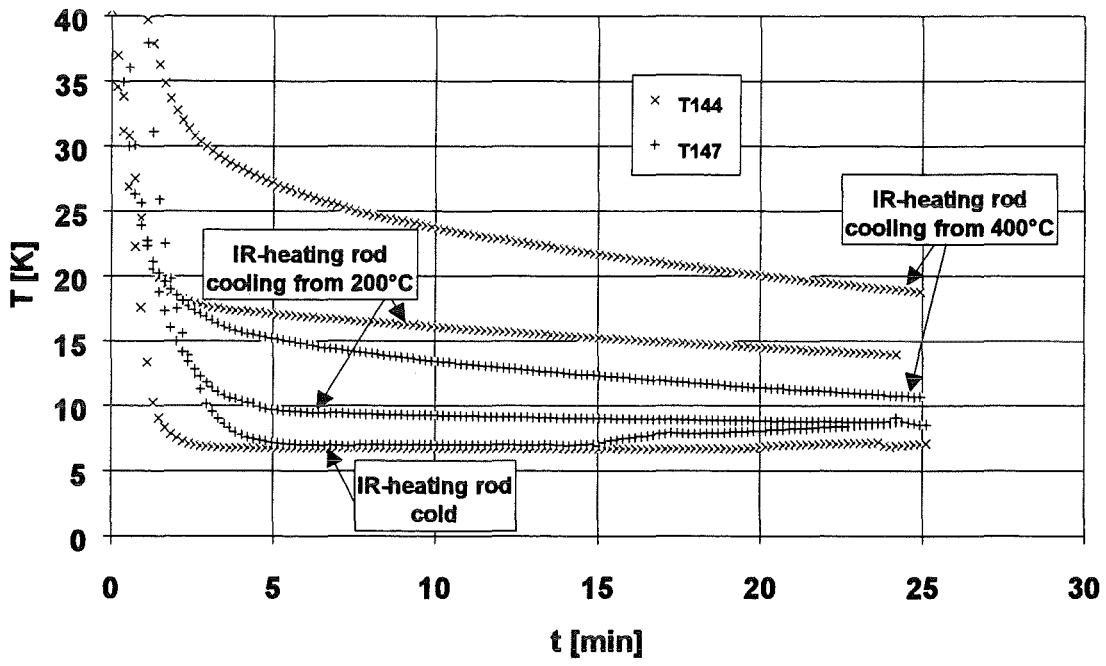

Figure 18: Cool-down behaviour of the panel.

To achieve a better performance, the heating rod should be cooled actively. From the energetic point of view, this cannot be accepted. It is a typical drawback of contactless heating methods. Also, controlling of such techniques is very unsatisfactory, because of the great time lag of the heating section. Therefore, the other two heating techniques investigated are direct-contact, bulk heating methods.

6.4 Warm gas (GHe) heating

In Table 5 the corresponding matrix for tests with forced flow of warm He gas (GHe) is given. The heating tests were performed at a parametric variation of the GHe flow rate. The momentary flow rate was determined indirectly by monitoring the pressure decrease in the He supply high-pressure bottle (c.f. annex A). The flow rate was realized at different pressure situations, characterised by the total pressure at no flow p_{tot} and the pressure measured during flow p_{stat}.

Table 5: Test matrix for GHe flow method.

Test run #	Panel, situation	p_{tot} [bar]	p_{stat} [bar]	Averaged mass flow rate [g/s]
A1HEa	P I , unloaded	5.1	1.4	1.1
A1HEb	P I , unloaded	9.9	3.6	1.9
A2HE	P I , unloaded	19.5	8.0	4.0
A3HEa	P I , unloaded	25.0	13.3	5.1
A3HEb	P I , loaded	25.0	12.7	5.0
A4HEa	P I , unloaded	0.90	0.36	0.27
A4HEb	P I , unloaded	14.7	7.6	2.9
A5HEa	P II , unloaded	19.8	9.7	3.8 [7]
A5HEb	P II , loaded	20.8	10.0	3.8 [7]

In Figure 19 a typical result is shown. Obviously different types of heating curves are obtained; two temperature sensors (T145 and T142) show a change in curvature during the heating process. This is due to great fluctuations in the channel-related throughput. The maldistribution is explained by different pressure losses for the individual channels: The unification of partial streams produces other pressure losses than the corresponding division of a total stream into partial streams [33, 34].

[7] For the GHe flow measurements with panel II, a drift in mass flow during the experiment was observed (see annex A). These two tests should therefore only be used for intercomparison,

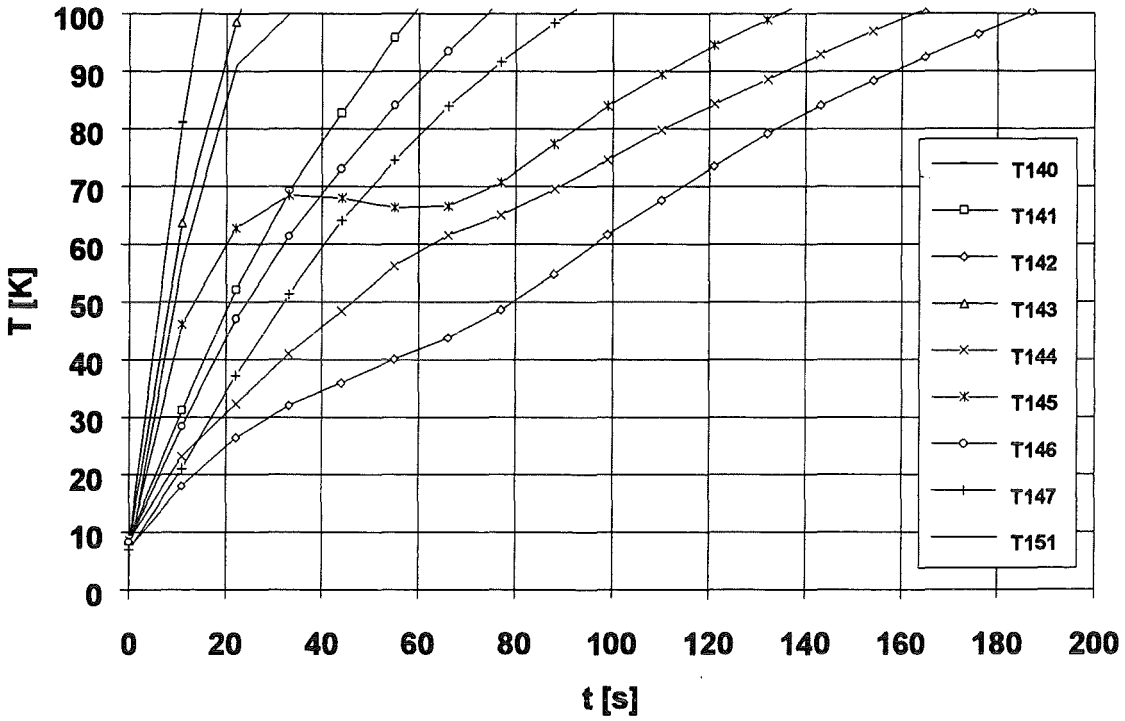

Figure 19: Typical heating curves at 4 g/s GHe flow rate (test run A2HE).

The influence of the pressure drop on the flow rate is very much emphasized by the increase in volume caused by the evaporation of the LHe inventory. As this is not representative for the ITER operation, the results can only be used for intercomparison. Furthermore, the panels discussed for ITER will consist of less than 7 channels. Thus, the influence of the unsymmetrically positioned feeder is much weakened. For this reason and to diminish the maldistribution influence to the largest possible extent, we base our comparison on the situation of that channel, which is directly above the inlet section of the panel. The heating curve of this channel is characterised by the positions 140 (panel inlet) and 143. The sensors 141 and 146 are mounted at a certain distance from the channel and, therefore, show greater heating times. In annex C the heating curves of these 4 representative positions are given both graphically and in tabular form for all tests done.

The accelerating influence of pressure on the heating process is illustrated in Figures 20 and 21.

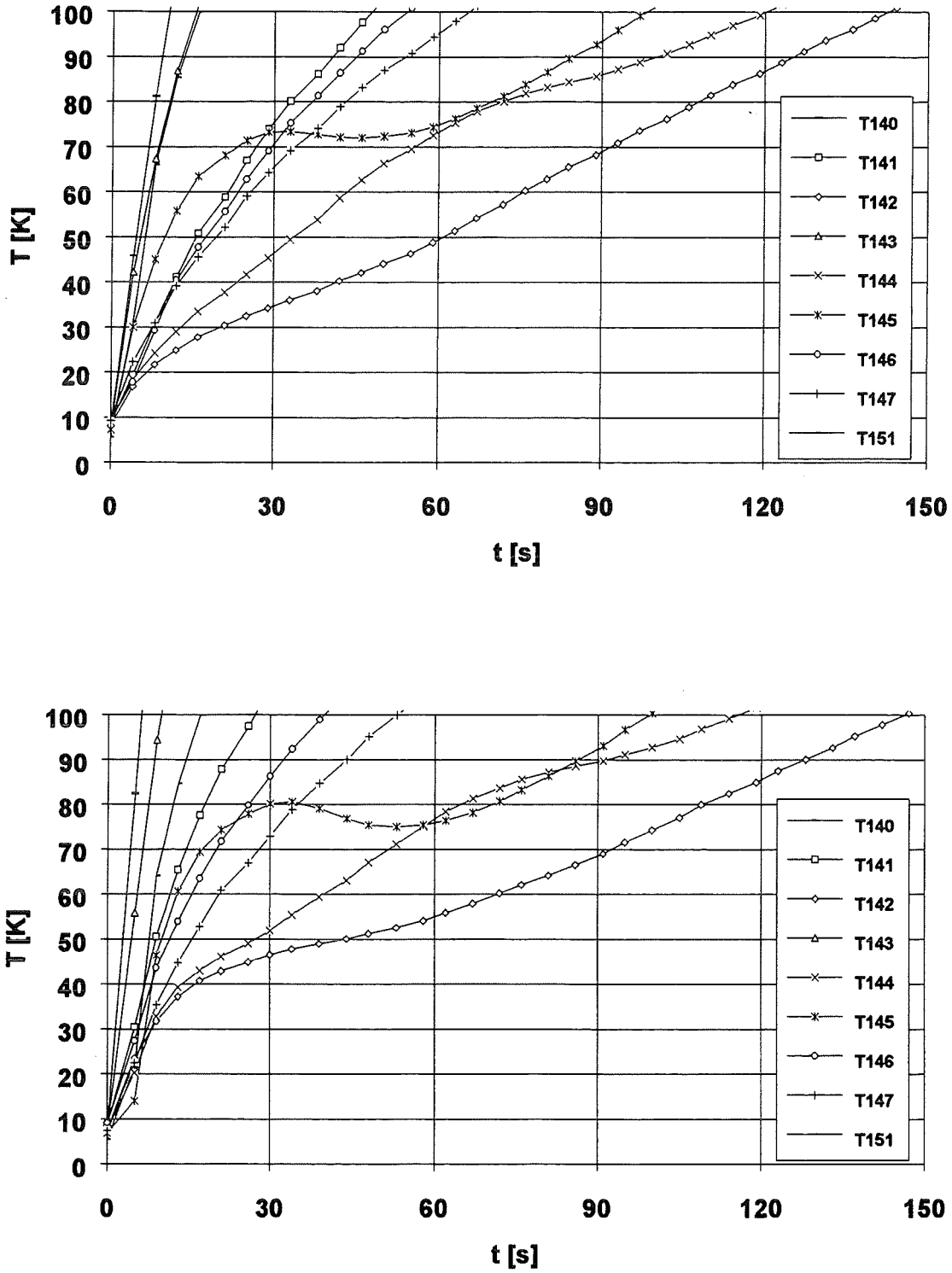

Figure 20: Heating curves for 5.1 g/s GHe flow rate (above, test run A3Hea) and 5.0 g/s (below, test run A3HEb), respectively. Comparison between heating performance of an unloaded (above) and a loaded panel (below). Experiments done with Panel I.

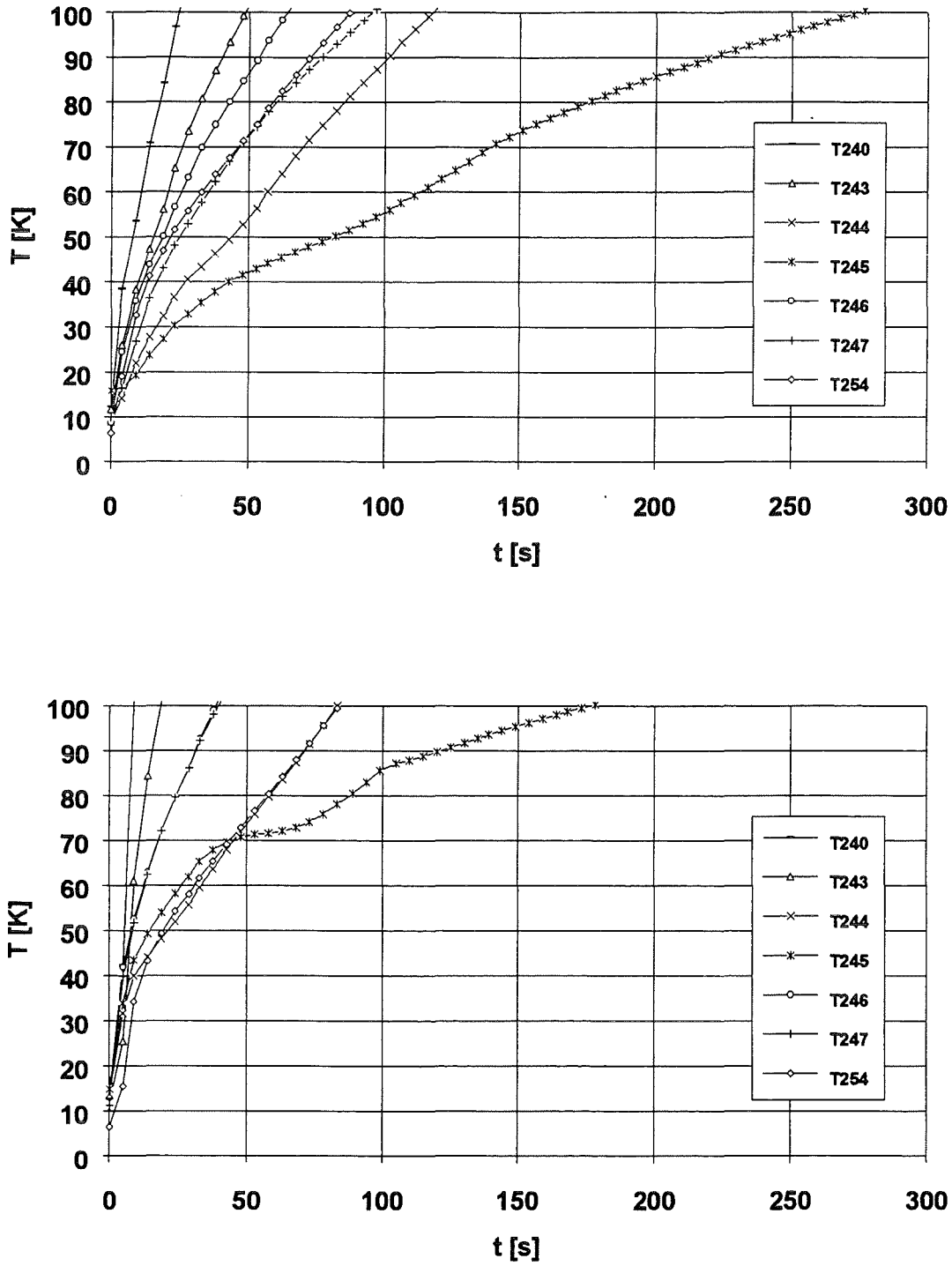

Figure 21: Heating curves for approx. 3.8 g/s GHe flow rate (above, test run A5HEa; below, test run A5HEb). Comparison between heating performance of an unloaded (above) and a loaded panel (below). Experiments done with Panel II.

These two Figures give the heating curves at comparable mass flow for experiments with a loaded and an unloaded panel [8,9]. For the experiments using the loaded panels we measured an instantaneous pressure rise from 10^{-3} mbar to 2 mbar in less than 3 s from the start of the heating process. The heating is supported by the pressure increase, due to an additional heat flux arising from gas molecular conduction. The additional heat of desublimation resp. desorption which has to be supplied when heating up a loaded panel does not play an important role.

All results for the GHe forced flow method are summed up in Figure 22, which gives the heating times to achieve the temperature of 90 K at various mass flows.

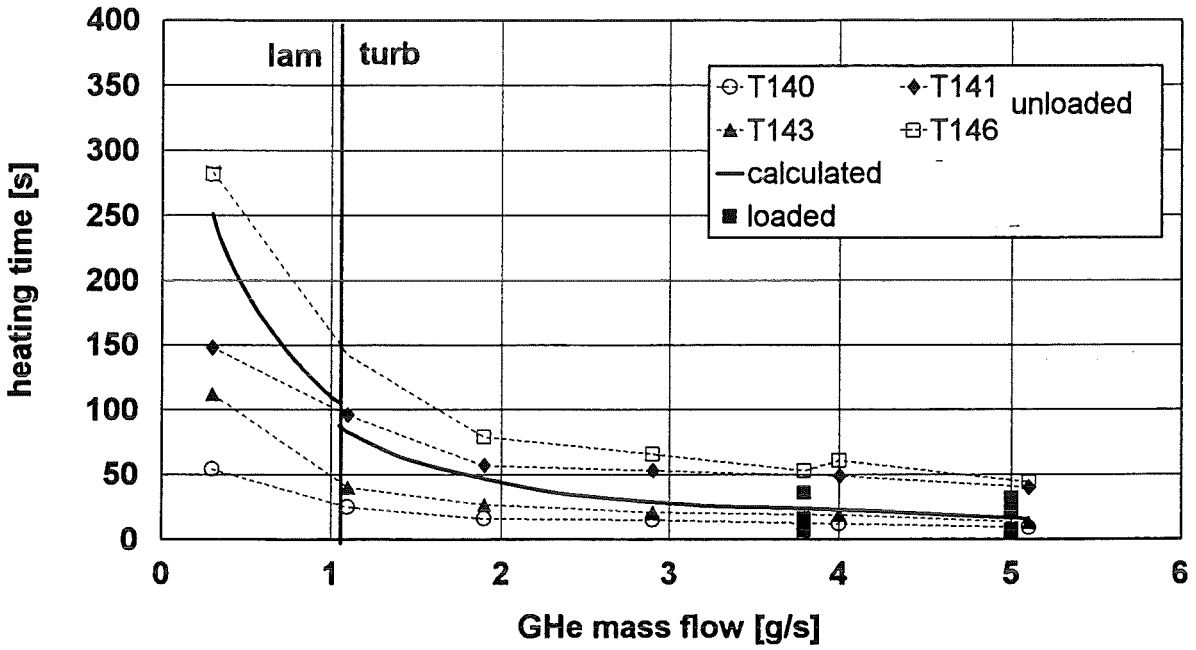

Figure 22: Summary of the results for fast heating up to 90 K using the warm helium forced-flow method.

The experiments peformed covered laminar and turbulent flow including the thermodynamically controlled regime for high gas throughput. It was found out that

[8] Sensors T241 and T242 were defective.

[9] The panel was loaded according to ITER-relevant conditions using a typical ITER exhaust gas composition, see footnote 6 [4]. The test illustrated in Figure 20 b was performed with a final gas load of 8741 mbar l/s (according to a pumping time of 20 min, related to 180 g MALTI), the test illustrated in Figure 21 b was performed with a final gas load 6698 mbar l/s (according to a pumping time of 750 s, related to 100 g MALTI).

for turbulent flow conditions inside the flow channels, heating times of less than 60 s do not pose any problem. From the economic point of view, it is not justified to operate with more than about 4 g/s, as the heating times are not reduced essentially in this thermodynamically controlled region. The measured times are compared with calculated data based on a simple model for the average caloric temperature. The model and the assumptions it is based upon are discussed in detail in annex D.

The GHe forced flow is a possible method for achieving fast heating of cryopanels. One drawback of the heating technique was the maldistribution of the gas feed between the various channels. To minimise this unwanted effect, it is recommended to use panels with less flow channels. Because of the maldistribution, no controlling strategies could be developed. However, as the heating process is primarily not controlled, difficulties are to be expected, if defined temperatures shall be reached and no overshooting can be tolerated.

6.5 Electric (COAX) heating

At last, we performed heating tests using a cryopanel with resistive heating elements of COAX type, attached on its surface. As for the GHe forced flow method, tests were carried out using both bare and loaded panels.
On each side of the panel we fastened three elements, two of which were controlled by one heating loop using a thermocouple as controlling sensor. First tests at ambient temperature proved that the heat conduction within the copper layer is that fast that fine controlling would be feasible even in the case of a very rapid heating process. A further decrease in heating time is expected, as this heating method directly affects the charcoal without the additional heat transfer resistance through the steel wall. Furthermore, the heating performance is expected to be much more homogeneous, because of the uniform coverage of the whole surface with heating elements and because of the additional temperature equalising copper coverage.

At first, we had to adapt the parameters of the PID controllers. The best temperature profile would be a rapid increase until the upper regeneration temperature would have been reached and instantaneous constancy at this temperature level (no overshooting, if ever possible). Typical results are given in Figure 23.

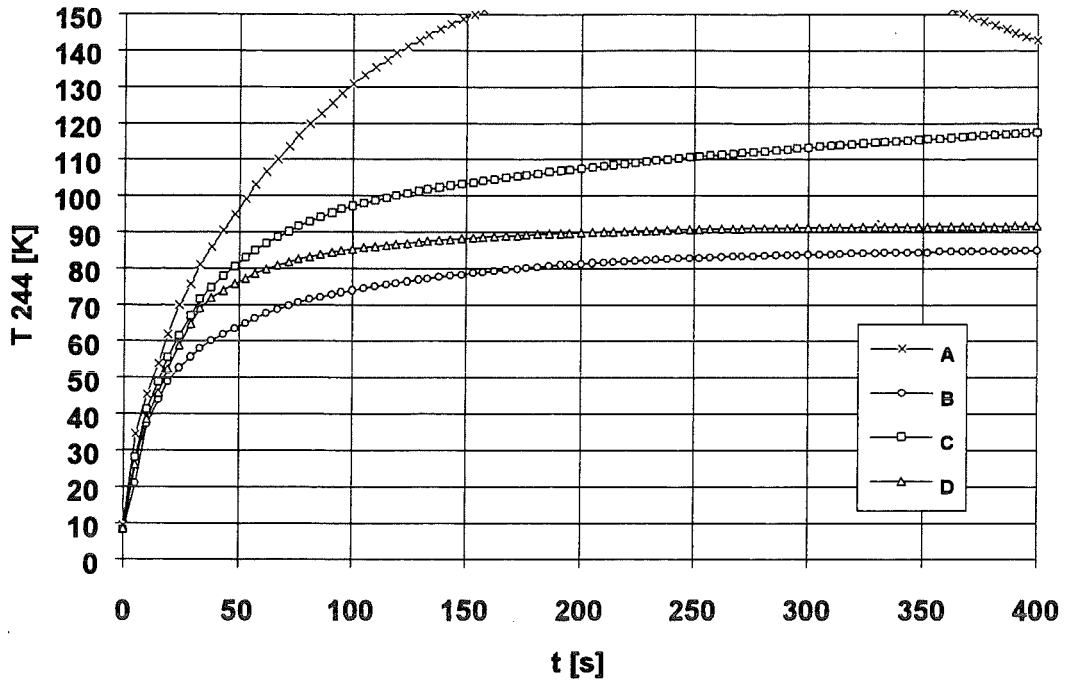

Figure 23: Comparison of different operation modes of the PID controller (set value 90K) for COAX heating. (A) PID, large D; (B) PID, small D; (C) large P; (D) small P.

In various tests we found that a simple two-point-control operation mode (i.e. the I and D part of the controller is set to zero) yields temperature profiles, which are most similar to this optimum shape. All tests discussed in this chapter were performed with this controlling mode.

Once having found the optimum controlling parameters, we performed a series of heating tests at variable electric power input. In Table 6 the corresponding matrix for the tests is given. To be able to separate the influence of the controller and the heating result, we performed two different kinds of experiments: One with the use of the controller set to 90 K as the upper temperature range desired (named 'controlled heating') and one with the use of the controller set to 150 K to simulate uncontrolled heating, i.e. full electric power heating at least until 120 K (named 'full heating') in the whole regeneration temperature range.

A typical result for panel heating is given in Figure 24 for 2390 W heating power input. All other heating curves are given in annex E. In Figure 24 a, the measured heating curves for unlimited heating operation are illustrated, in Figure 24 b for controlled operation (setpoint temperature 90 K) and in Figure 24 c for controlled heating of the loaded panel. In the dynamic heating process, the great influence of different thermal response times is examplified by comparison of the Fe-Rh sensor and the Si diode.

Table 6: Test matrix for electric method.

Test run #	Panel situation	controlling situation	electric power input [W]
H4E1	unloaded	controlled	2390
H4E2	unloaded	full	2390
H4E3	unloaded	full	1250
H4E4	unloaded	controlled	1250
H4E5	unloaded	controlled	3070
H4E6	loaded	controlled	2390
H4E7	unloaded	full	3070
H4E8	loaded	controlled	3070

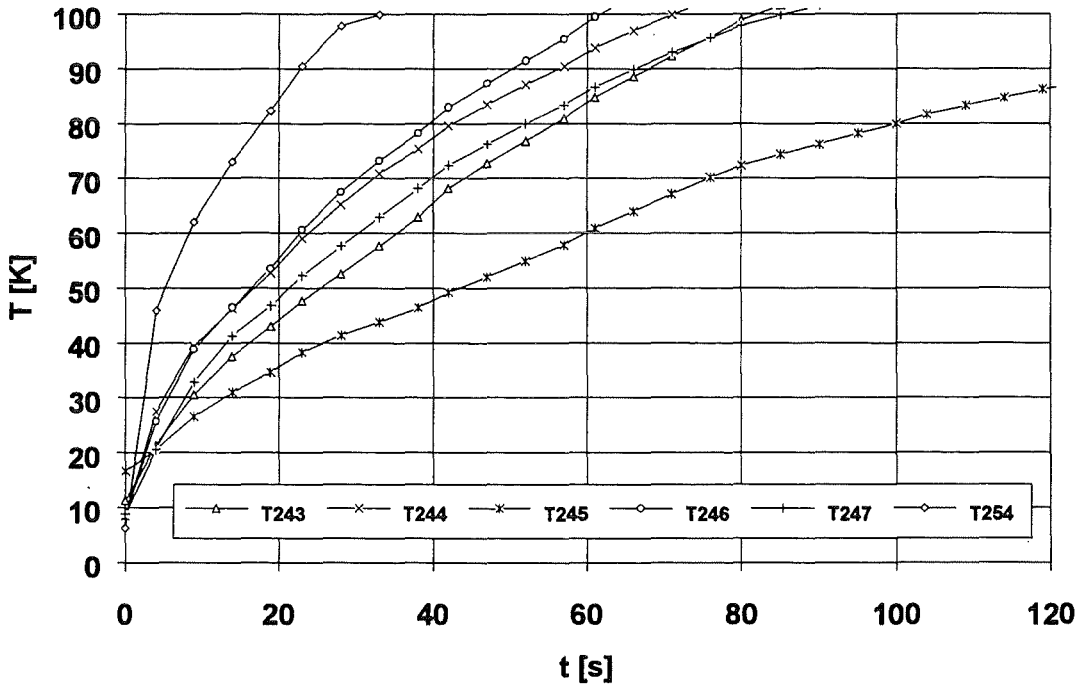

Figure 24a: Full heating of unloaded panel (test run H4E2).

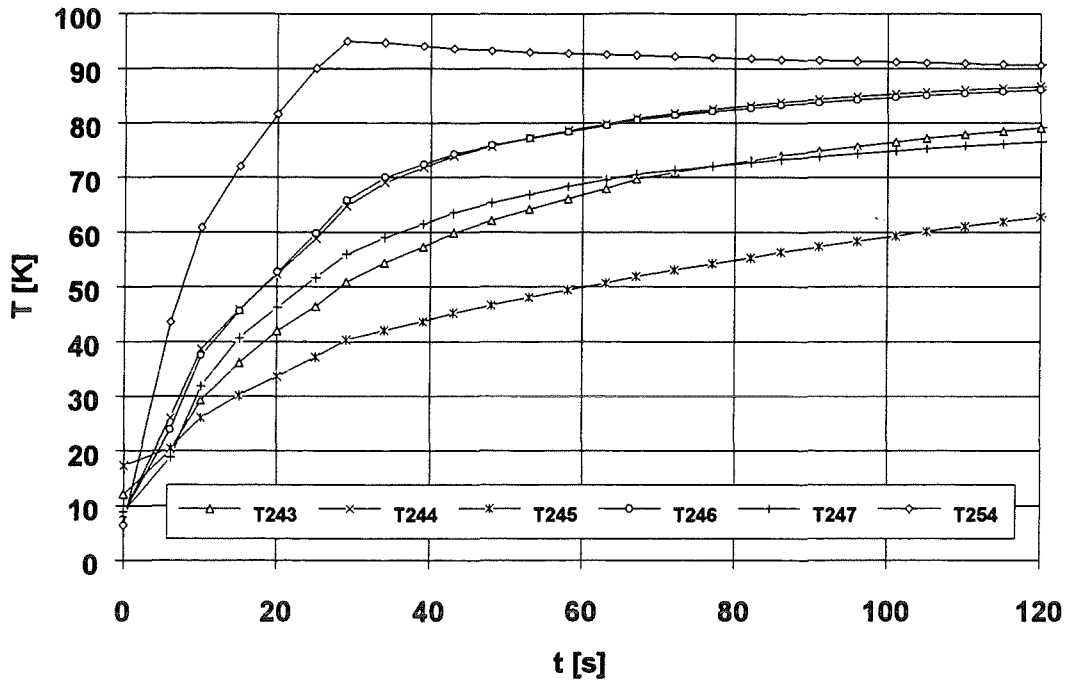

Figure 24b: Controlled heating of unloaded panel (test run H4E1).

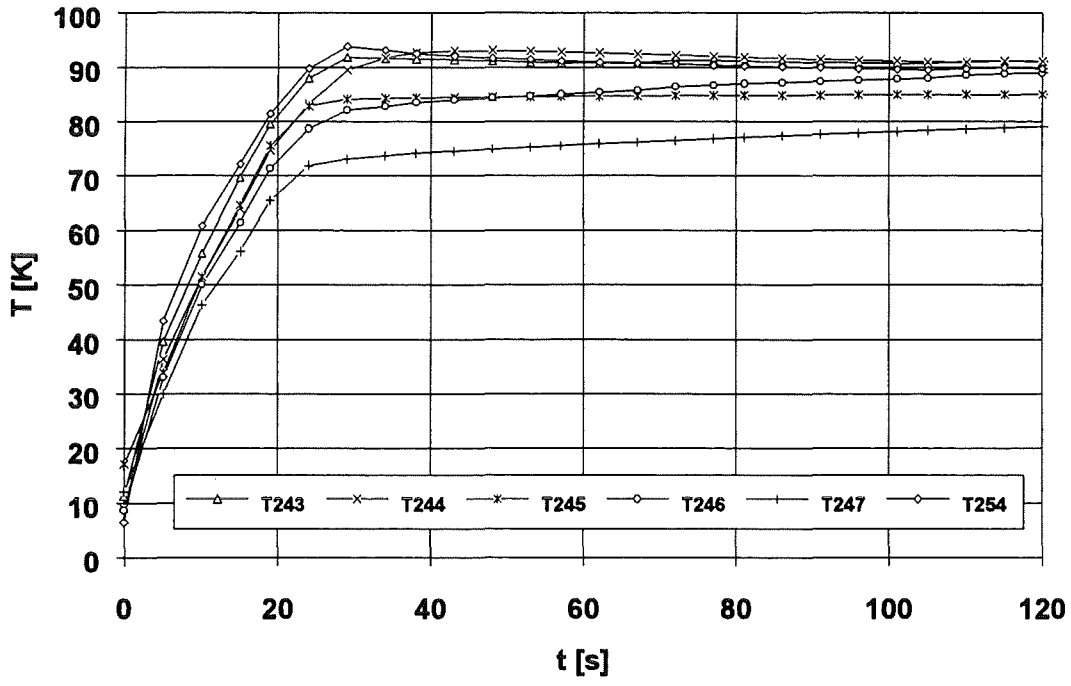

Figure 24c: Controlled heating of loaded panel (test run H4E6).

Figure 24: Heating curves for COAX heating at 2390 W and three different modes: a) full heating of unloaded panel (above), b) controlled heating of unloaded panel (middle), c) controlled heating of loaded panel (below).

On a whole, it can be seen that the sensors showing the lowest temperatures in steady-state cooling give the shortest heating times. Both features can be explained with a good contact situation. The worse the contact conductance is (large thermal inertia), the higher is the resistance for heat flux.

The heating behaviour of the loaded panels reveals the characteristics of the controller influence. As temperature sensor within the control loop we used a thermocouple, which is comparable to the Si diode as far as thermal response times are concerned. Consequently, the Si diode (T254) curves represent the decisive temperature for the control loop: As soon as the set value of 90 K has been reached, the active heating phase was over. This has been after about 25 s. Until then, the panel heating behaviour is very comparable (compare Figures 24a and 24b). After this time, all further temperature rises in the case of controlled operation are due to temperature equalisation processes, whereas for full heating operation there is still an active heat input coming from the heating elements. That is the reason why the heating times necessary to reach 90 K in controlled operation as measured by Fe-Rh sensors are distinctively greater than for uncontrolled operation. This situation is illustrated in Figure 25 for the two central sensors: the diode T254, which comes very near to the 'real' dynamic behaviour of the charcoal and the corresponding Fe-Rh sensor (T244). In Figure 25 a, the heating times to reach 80 K for the unloaded panel in both operation modes are compared for variable electric power; in Figure 25 b the corresponding heating times are given for the temperature setpoint value 90 K. The influence of the different temperature sensors can be seen. As discussed above, the fast responding diode (circular symbols) gives the same behaviour in both operation modes; this represents the most the physically 'true' behaviour. The slow responding Fe-Rh sensor shows higher heating times. The difference in heating time between the two sensors in full heating mode (approx. 30 s) is only caused by the sensor type itself (thermal response behaviour and contact situation). Consequently, this time lag is comparable in figs 25 a and b. Whereas the difference in controlled heating mode is additionally influenced by the thermocouple-based controlling strategy. For that reason, it is significantly greater in Figure 25b where controlled heating up to the setpoint temperature is concerned. In this case, the maximum delaying impact of the controlling on fast heating when being measured by Fe-Rh sensors is illustrated. The impact of controlling vanishes for diode measurements. Both parts of Figure 25 reveal that an increase of electric heating power from 2.4 to 3.1 kW does not improve the heating performance essentially, whereas the smaller heating power of 1250 W leads to remarkably longer heating times.

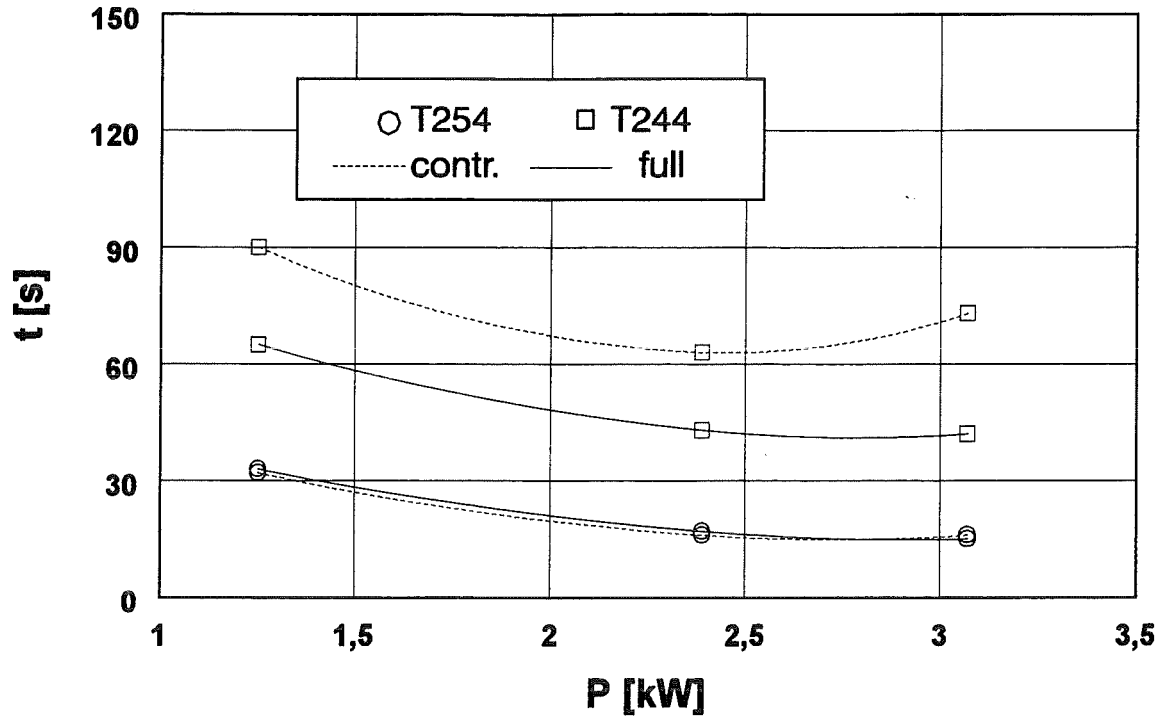

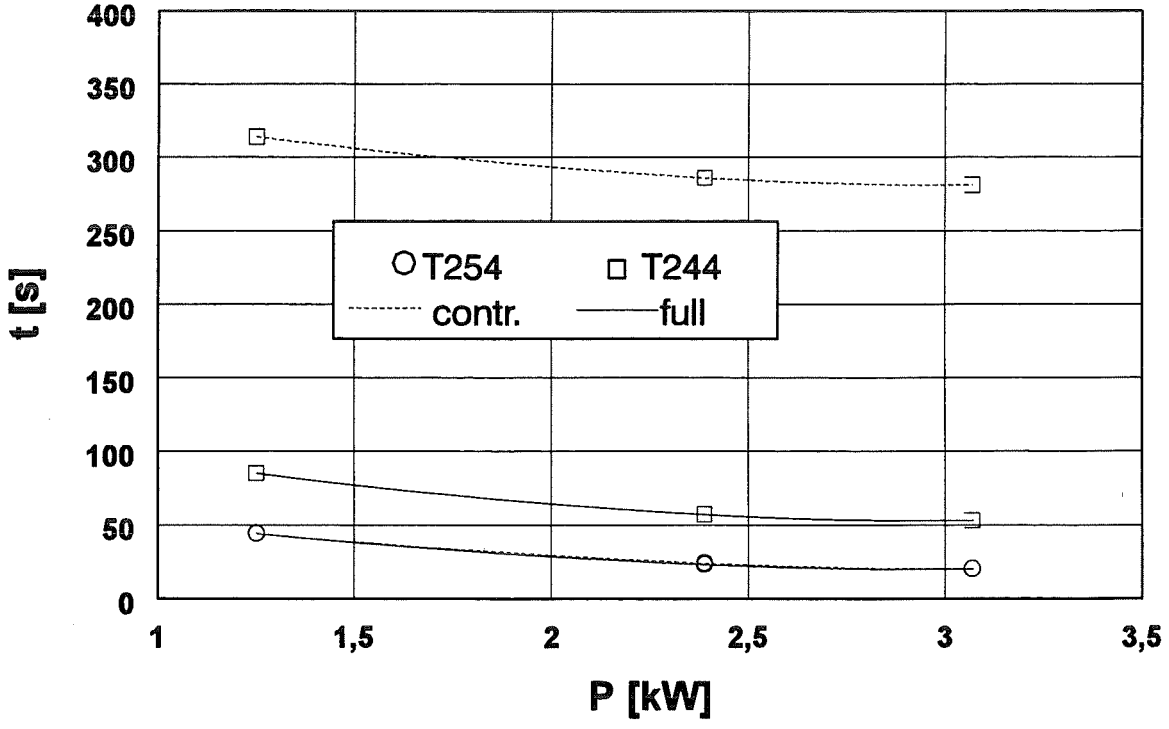

Figure 25: Comparison of heating times for COAX heating at different electric power and both operation modes for the unloaded panel. The heating times correspond to 80 K (above) and 90 K (the setpoint of the controller) (below), respectively.

In Figure 26, the situation at a fixed heating power of 2390 W for controlled heating is illustrated in the whole temperature range between 80 and 90 K. The heating times measured by the Fe-Rh sensor T244 are too large due to the influence of the sensor type (almost constant over the whole temperature range) and they are additionally influenced by the controlling strategy, because the active heating phase is only 25 s. After this time there is only 60 K measured at T244. The further heating process is caused by temperature equalisation; therefore, the measured time is increasing with decreasing temperature difference to 90 K.

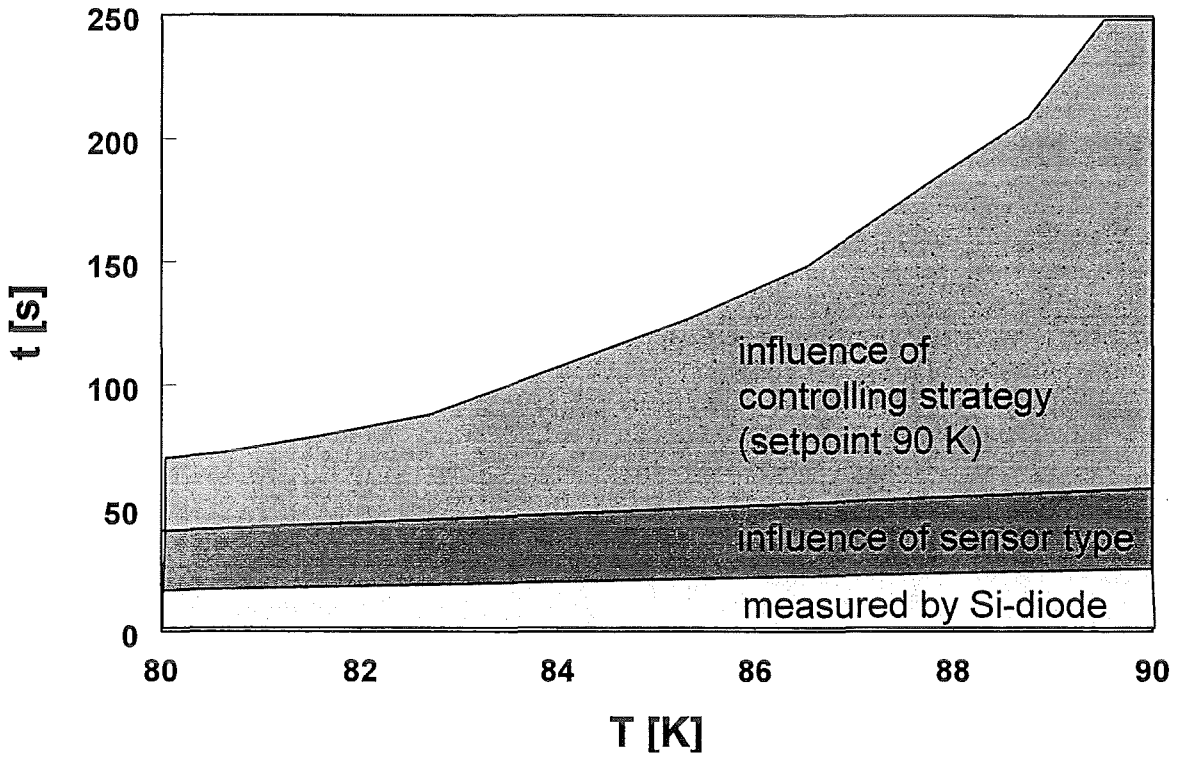

Figure 26: Illustration of the individual influences on the heating times measured by the Fe-Rh sensor (T244, P=2390 W).

To work out the characteristics in more detail, the performance under the same controlling, but different heat transfer conditions must be compared. This is illustrated in Figures 24b and 24c, both for controlled operation mode. It becomes obvious that for loaded panels, a significantly faster heating can be achieved (this has also been shown for the GHe heating method). The panel temperature is much more homogeneous than for unloaded panels. This is due to the rapid pressure rise and the increased heat transfer as a result to degassing of the frozen gas. The heating curves, together with the pressure behaviour are plotted in Figure 27 for a controlled heating experiment with 3070 W.

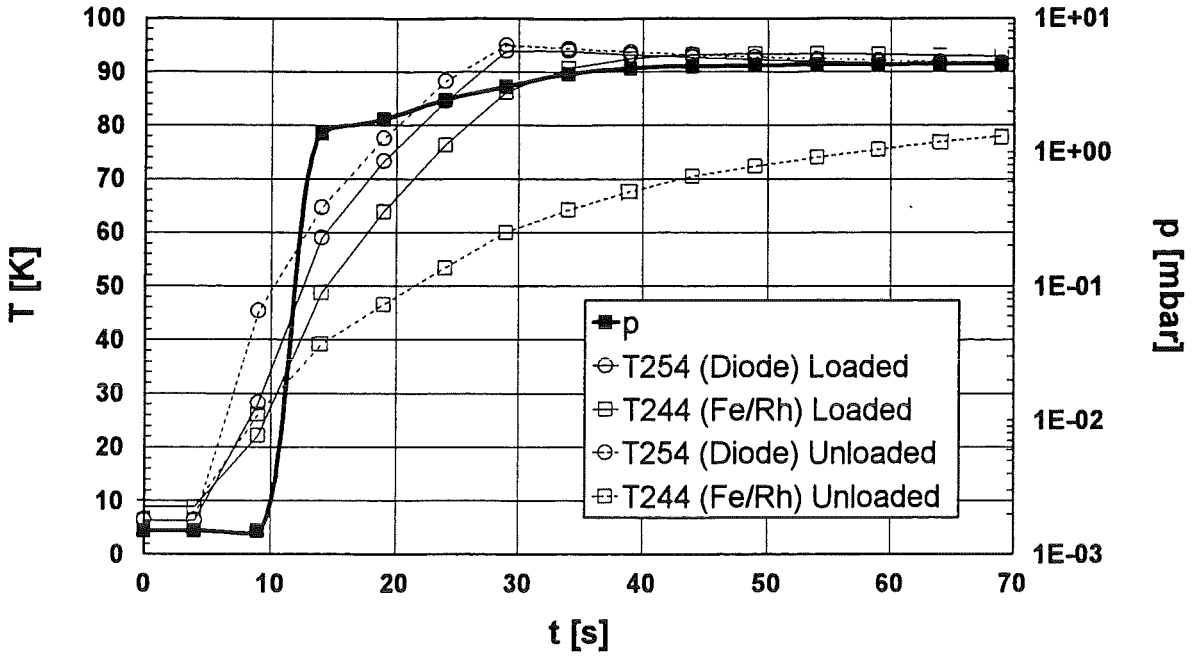

Figure 27: Comparison of heating behaviour for loaded and unloaded panels (Experiment at 3070 W in controlled operation mode).

The pressure rises as soon as the equilibrium desublimation/desorption temperature has been reached (approx. 10 K for the investigated mixture). We measured typical pressure increases from 10^{-3} mbar to 1 mbar in 4.5 s. As a consequence to the high pressure, an additional positive heat flux results from molecular heat conduction coming from the 80 K surroundings. This effect enhances the heating especially in the higher temperature range, in which the greatest percentage of total heating time is caused.

It is once more shown, that the diode heating curve does only very little depend on the operation mode. The results for the unloaded panel illustrate again that the heating curves determined by the Fe-Rh sensors are much closer to the ones of the diode as in the case of unloaded panels. There is no delay anymore, because they are heated not only through the contact spots with the panel but also by the molecular heat conduction, which affects the whole sensor surface and the charcoal also of course. During our tests with forced GHe we also measured that steep pressure increase but we did not notice such a strong impact on heating times (see Figures 19 and 20), because the local neighbourhood of the sensor worked as a heat sink. Whereas for the experiments with the COAX heaters, the local sensor area is in much better contact with the resistance heaters due to the electrolytic covering with copper. Keeping that in mind, the measured results for loaded panels are very

representative for the charcoal, which also is in close contact with the electric heaters.
Taking the diode measurements as physically true values and representative for the whole panel (as discussed above), the heating can take place in the magnitude of less than half a minute. Fast heating is also feasible in the controlled mode.

The results for heating up to 80 K and 90 K, respectively are summarized in Figures 28 and 29. The experimental results refer to the Si diode and therefore are very much the same for loaded and unloaded panels (c.f. Figure 27) and for uncontrolled and controlled heating (c.f. Figure 25). They agree very well with calculated heating times using a mean temperature for the whole panel and under the assumption of zero heat losses to the environment.

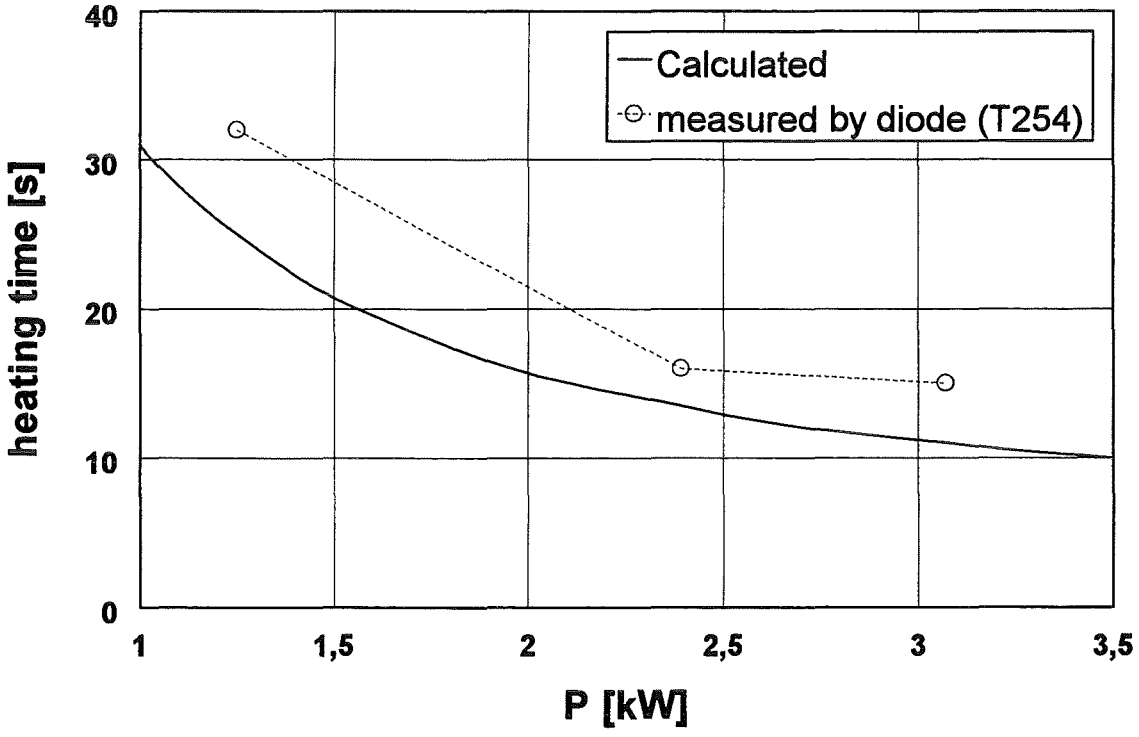

Figure 28: Summary of the results for electric fast heating up to 80 K.

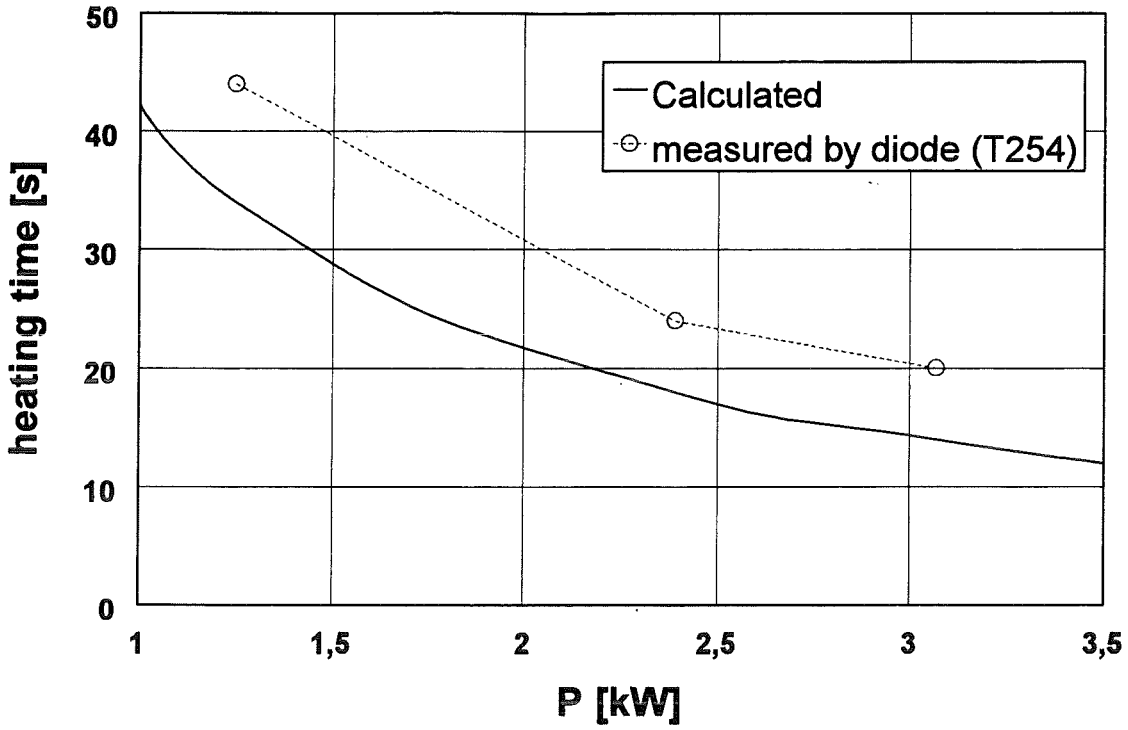

Figure 29: Summary of the results for electric fast heating up to 90 K.

7 Conclusion

The individual pump cycles of ITER cryopumps are kept very short short to minimize the localised tritium inventory. To also keep the numbers of installed cryopumps as small as possible, the regeneration period comprises only 250 s. Approximately 60 s are left for fast heating of the cryopanels from LHe temperature to about 90 K.

Three heating methods for use in the fast regeneration process of cryopumps were tested within a parametric variation of energy input.
As representative for contactless techniques, infrared radiation heating was investigated. In the tests the required short heating times could not be achieved. Furthermore, the experiments revealed, that thermal inertia of the heating rods is too high to attain a feasible operability. This is a generic drawback of methods where the heating source is not in contact with the panel; these methods cannot be recommended for fast heating processes in cryopumps.
As the second method, we generated a forced flow of warm helium gas in the flow channels of the cryopanel. The heating times at different mass flows were recorded.

We measured a remarkable temperature inhomogeneity across the panel surface, mainly due to flow maldistribution as result to the evaporation process of the LHe hold-up in the panel. However, as it is planned to cool the ITER cryopumps with supercritical He, the maldistribution problem of our tests is not crucial when this heating method is used for ITER. Depending on the position at the panel, the heating times measured were less than 60 s.
The third heating method investigated was surface bulk heating with electrical resistance heating elements. Using this technique, it was no problem to achieve heating times of less than 30 s. It could be shown that the pressure increase resulting from the thermal release of frozen gas supports the heating pretty much. Incorporating a refined control strategy, the electric heating process is highly recommended for use in ITER cryopumps.

For fast heating as part of the regeneration process of ITER cryopumps both warm gas heating and electric heating are recommended technologies. The required expenditure of energy for one full scale ITER cryopump (8 m^2 pumping surface) can be estimated to be the enthalpy difference related with 70 g/s GHe flow or about 50 kW electric heating power. This is only a rough estimation; the accurate number depends on the detailed design of the pumping area (number of channels per panel, number of panels per pump), which has not yet been fixed. In Table 7 the advantages and drawbacks of these two methods are compared.

The table reveals that the COAX heating method is characterized by a very high versatility in use. The possibility to distribute the total heating power among several heating elements enables the operator to limit the heating to a certain area of the whole panel. Thus, it may be feasible to install panels with a heated side (the condensation side of the panel including tritium) and an almost unheated side (the sorption side of the panel, which does not need to be heated in each regeneration step). The GHe method is also more difficult to control than the electric heating. On the other hand, the maintenance and (explosion) safety of electric heater installation has to be investigated in more detail. At last, an economic estimation has to be made, to judge the financial needs for GHe flow rates and electric current, respectively.
Experimental tests on fast cooling of cryopanels [35] showed that the energetic needs are higher than for fast heating. Therefore, it could be feasible, to save part of the specified 60 s for fast heating in order to be able to admit more time for cooling.

Table 7: Comparison of the recommended heating methods.

Feature	GHe heating	COAX heating
Heating times	< 60 s	<30 s
Energy consumption for 0.35 m^2 panel area (both sides) (Partial regeneration)	GHe enthalpy difference related with 3 g/s flow rate	electric current 2 kW
Energy efficiency	low (heating through the steel wall)	high (direct heating of the charcoal)
Possibility of total regeneration	$T_{max}=T_{He}$ at the panel inlet	unrestricted[10]
Possibility of limitation of the heating on individual heating zones	no	yes
Controllability	poor	very good
Maintenance	good	poor
Manufacturing	standard	more manufacturing steps necessary
Temperature homogeneity	poor	well

8 Acknowledgments

The authors wish to thank A. Edinger, H. Reinhard, R. Töpfer and D. Zimmerlin for their help in many aspects of this work.
This work has been performed within the framework of the Nuclear Fusion Project of FZK and is supported by the European Communities under the European Fusion Technology Programme.

[10] For ITER conditions (assumed panel mass to be heated 120 kg [22, 24]) we calculated 222 s for the electric heating from 5 to 300 K.

9 References

[1] ITER Team, ITER Design Description Document DDD, San Diego 1995

[2] Haefer, R.A. : Cryopumping. Clarendon Press, Oxford 1989

[3] Baechler, W.G. : Cryopumps for research and industry. Vacuum 37 (1987) 1-2, 21 - 29

[4] Ladd, P. : ITER Vacuum equipment specification - primary cryopump, ITER Doc.no. G131SP001W1.1, Garching Joint Work Site, April 1996

[5] Souers, P.C. : Hydrogen properties for fusion energy. University of California Press, Berkeley 1986

[6] Roth, A. : Vacuum technology. 3rd ed., North-Holland/Elsevier, Amsterdam 1990

[7] Hablanian, M.H. : High-vacuum technology. Marcel-Dekker, New York 1990

[8] Perinic, D.; A. Mack; H. Illbruck; G. Class; D. Röhrig; D. Murdoch : Experiments on co-pumping of simulated plasma exhaust gases in a two-stage cryopump. Proceedings 17th SOFT, Roma, Italy, September 1992

[9] Özdemir, I.; D. Perinic : A comparison of thick and thin sorbent layers for plasma exhaust cryopumping. Proceedings 18th SOFT, Karlsruhe, August 1994, 1123 - 1126

[10] Mack, A.; D. Perinic; J.-C. Boissin; D. Murdoch : Experimental investigations of helium cryotrapping by argon frost. Fusion technology 21 (1992) 2, pt.2, 902-908.

[11] Mack, A.; J.-C. Boissin; D.K. Murdoch; D. Röhrig; G. Saksagansky : Primary vacuum pump concept, component testing and model pump development for ITER. Proceedings 19th SOFT; Lisboa, Portugal, September 1996

[12] Mack, A., Forschungszentrum Karlsruhe, Interner Bericht HIT 1995

[13] Jaeckel, M; F. Fietzke : Investigation into sorption kinetics of porous solids at low temperatures and under vacuum conditions. Vacuum 44 (1993) 5-7, 421 - 424

[14] Kast, G. (ed.) : Nuclear Fusion Project Annual Report of the Association FZK/EURATOM. Forschungszentrum Karlsruhe Report FZKA 5688, 1996, 21-24

[15] Mundinger, H.-J.; H.U. Häfner; M. Mattern-Klosson; H.H. Klein; U. Timm : A new cryopump with a very fast regeneration system. Vacuum 43 (1992) 5-7, 545 - 549

[16] Häfner, H.U.; H.H. Klein; U. Timm : New methods and investigation for regenerating refrigerator cryopumps. Vacuum 41 (1990) 7-9, 1840 - 1842

[17] Obert, W.; K. Barth; L. Herblin; C. Mayaux, G. Saibene; E. Thompson : Performance of the JET pumped divertor cryopumpsystem. Proceedings 16th SOFE, Urbana-Champaign, USA, Sept./Oct. 1995, 742 - 745

[18] Schaubel, K.M.; J.P. Smith; Laughon, G.J.; C.B. Baxi; G.L. Campbell; M.A. Mahdavi; R. Maingi; M.M. Menon; M.J. Schaffer; R.D. Stambaugh : The DIII-D Divertor cryopump system: Design and operational experience. Proceedings 18th SOFT, Karlsruhe, August 1994, 347 - 350

[19] Gouge, M.J.; C. Foster . Argon frost continuous cryopump for fusion applications. DOE Final report no. DOE/ER/81236-6, 1995

[20] Gouge, M.J.; L. Pittenger : Fast regeneration of ITER cryopumps. Proceedings of Combined technical meeting tritium plant and fuelling & pumping systems. ITER Naka JWS, Dec. 1995

[21] PNEUROP Document PN5ASRCC/5 : Vacuum Pumps - Acceptance Specifications refrigerator cooled cryopumps. Maschinenbau-Verlag GmbH, Frankfurt, 1989

[22] Murdoch, D.; A. Mack; H.D. Röhrig; E. Karb; C. Day; N. Petersohn : Technical specification for the ITER model pump, The NET Team/Forschungszentrum Karlsruhe, 1996

[23] Perinic, D.; H. Haas; A. Mack : Development of cryosorption panels for cryopumps. Adv. Cryogenic Engng. 39 (1994) 1553 - 1559

[24] Boissin, J.C., unpublished report, Comp. Air Liquide/FZK-HIT 1995

[25] Hanauer, J.; T. Höhn; H. Lukitsch; A. Mack; D. Perinic, Forschungszentrum Karlsruhe, Interner Bericht HIT 1991

[26] Spiegel, H.J.; M. Süßer, Forschungszentrum Karlsruhe, Interner Bericht ITP 1995

[27] Tison, S.A. : A critical evaluation of thermal mass flow meters. J. Vac. Sci. Technol. A 14 (1996) 4, 2582-2591

[28] McCarty, R.D. : Thermodynamic properties of He^4 from 2 to 1500 K at pressures to 108 MPa. J. Phys. Chem. Ref. Data 2 (1973) 4, 923-1042

[29] Madhusudana, C.V. : Thermal contact conductance. Springer, New York 1996

[30] Schlünder, E.U; E. Tsotsas : Wärmeübertragung in Festbetten, durchmischten Schüttgütern und Wirbelschichten. Georg Thieme, Stuttgart 1988

[31] Riedel, C. : Unveröffentlichter Bericht, GSI Darmstadt.

[32] Tokaryk, D.W.; G.R. Wagner; R.L. Brooks; J.L. Hunt : Infrared emission spectra from cryogenic proton-irradiated helium gas. J. Chem. Phys. 103 (1995) 24, 10439-10444

[33] Kast, W. : Druckverlust. in VDI-Wärmeatlas, 6. Auflage, Abschnitt Lc, VDI-Verlag, Düsseldorf 1991

[34] Wagner, W. : Strömungstechnik und Druckverlustberechnung. 2. Auflage, Vogel-Verlag, Würzburg 1990

[35] Day, Chr.; H. Haas; A. Mack : Development of cryopanel fast regeneration methods for use in the ITER primary vacuum system. Proceedings 19th SOFT; Lisboa, Portugal, September 1996

[36] Reiss, H. : Superisolationen. in VDI-Wärmeatlas, 6. Auflage, Abschnitt Kf, VDI-Verlag, Düsseldorf 1991

[37] Eder, F.X. : Arbeitsmethoden der Thermodynamik. Bd.2: Thermische und kalorische Stoffeigenschaften, Springer, 1983

[38] CRYOCOMP v.2.0 . Eckels Engineering/Cryodata Inc. , Colorado, USA , 1994

10 Annex

A Determination of the He flow rate for the warm gas heating tests

The warm gas heating tests were performed at a parametric variation of the GHe flow rate. The momentary flow rate was determined indirectly by monitoring the pressure decrease in the He supply high-pressure cylinder during the GHe flow as a function of time. The evaluation procedure how to calculate the mass flow from these experimental data is described in this section.

Incorporating the compressibility factor Z,

$$Z \equiv \frac{p \cdot V}{m \cdot \frac{R_0}{M} \cdot T} \quad , \qquad \text{(gas constant } R_0\text{=8.3145 J/(mol·K))} \qquad \text{(A1)}$$

with the Volume V, which contains the mass m of a gas with molar mass M (helium: M= 4.0026 g/mol) at the temperature T and pressure p, the mass flow can be derived as follows:

$$\dot{m} = -\frac{dm}{dt} = -\frac{d}{dt} \cdot \left(\frac{p \cdot V}{\frac{R_0}{M} \cdot T \cdot Z} \right) \quad . \qquad \text{(A2)}$$

From the experiment, the dependency of the pressure with respect to time p⟨t⟩ was measured. The gas cylinder volume V is known, as well as the room temperature T. The compressibility factor Z for a pure fluid is in principle a function of pressure and temperature. By separation of constant and time-dependent variables and conclusive differentiation we get:

$$\dot{m} = -\frac{V}{\frac{R_0}{M} \cdot T} \cdot \left(\frac{\frac{dp}{dt} \cdot Z - \frac{\partial Z}{dt} \cdot p}{Z^2} \right) \quad . \qquad \text{(A3)}$$

For helium, which is very close to the ideal gas state, Z can be approximated as one linear curve versus pressure for the whole temperature range of interest. Figure A1

illustrates the real gas data calculated with an accurate equation of state [28]. From these numbers we derived the simple expression

$$Z = A + B \cdot p / bar \quad , \tag{A4}$$

with A=1.00107 and B= $0.48616 \cdot 10^{-3}$, averaged between 275 and 300 K.

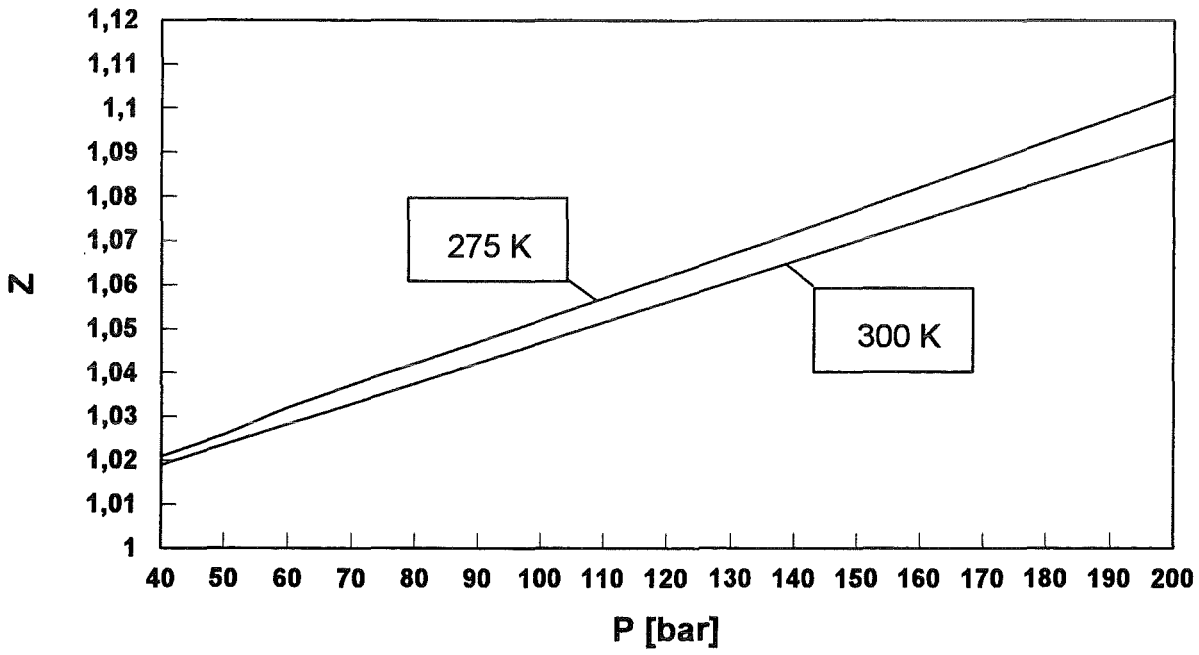

Figure A1: Compressibility factor of helium.

Applying this expression and considering the identity

$$\frac{dZ}{dt} = \frac{dZ}{dp} \cdot \frac{dp}{dt} \qquad \text{with } \frac{dZ}{dp} = \text{B=const.} \quad , \tag{A5}$$

the final equation can be written as follows:

$$\dot{m}\langle t\rangle = -\frac{V}{\frac{R_0}{M} \cdot T} \cdot \frac{dp\langle t\rangle}{dt} \cdot \left(\frac{Z\langle p\langle t\rangle\rangle - \frac{dZ}{dp} \cdot p\langle t\rangle}{Z\langle p\langle t\rangle\rangle^2} \right) = -\frac{V}{\frac{R_0}{M} \cdot T} \cdot \frac{dp\langle t\rangle}{dt} \cdot \left(\frac{A}{\left[A + B \cdot \frac{p\langle t\rangle}{bar} \right]^2} \right) \tag{A6}$$

In order to examplify how to continue the evaluation, we use the data of test run A3HEa. The registered data for the pressure curve are presented in Table A1.

Table A1: Measured pressure decrease in GHe supply cylinder during the experiment A3HEa.

pressure [bar]	time [s]
200	0
190	9
180	21
170	35
160	49
150	63
140	80
130	95
120	110
110	126
100	144
90	160
80	175
70	192
60	208

In the evaluation of the tests we found out that for all tests performed, it is feasible to fit the curve pressure vs. time as a second order polynomial

$$\frac{p\langle t\rangle}{bar} = a \cdot \left(\frac{t}{s}\right)^2 + b \cdot \left(\frac{t}{s}\right) + c \quad . \tag{A7}$$

For the data listed in Table A1, the fit yielded the following parameter values achieving a mean relative error in p of 0.7 % :

a= $0.499672 \cdot 10^{-3}$, b=-0.7563517, c=197.0222 .

Table A2 gives the final result for the calculated mass flow based on the above mentioned parameters. The high-pressure cylinder volume was V=49.7 l.

Table A2: Calculated GHe mass flow for the experiment A3HEa.

time [s]	mass flow [g/s]
0	5.2
10	5.2
20	5.1
30	5.1
40	5.1
50	5.0
60	5.0
80	4.9
100	4.8
120	4.7
140	4.6
160	4.5
180	4.4
200	4.3
220	4.2

The data in Table A2 are illustrated in Figure A2. The mass flows for all other tests are also given; they were determined analogously. The nominal mass flow values given in Table 5 are averages of an appropriate time range.
It becomes obvious that the mass flow was not constant, but showed a certain decreasing tendency with increasing time. This effect is the strongest for the experiments using panel II (A5HEa, A5HEb), which is surprising as the two panels are totally identical as far as the channel geometry is concerned. Both panels were manufactured by the same company according to identical construction drawings.

The achievable accuracy of the procedure outlined above is mainly determined by the error contributions connected with temperature measurement and measurement and fitting of the pressure. The measurement error of time, the error of the given cylinder volume as well as the inaccuracy of the compressibility factor, which has been temperature averaged is negligible. Thus, the maximum error can be estimated to be about 2 % .

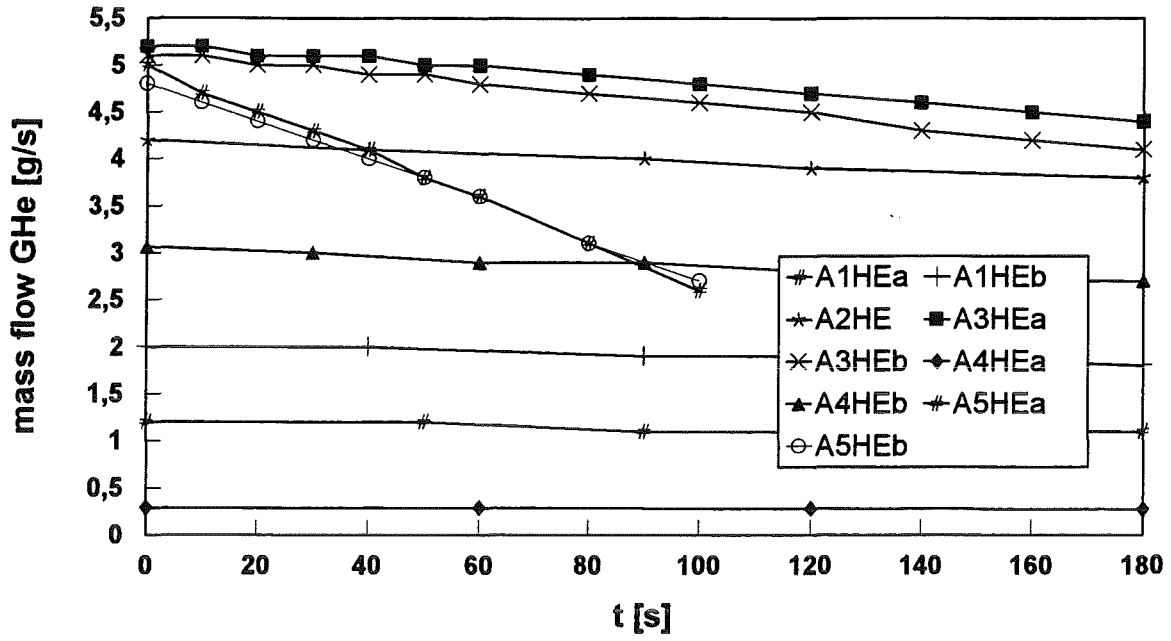

Figure A2: Dependence of the mass flow on time for the GHe experiments.

B Evaluation of the radiative shielding used for the temperature sensors

The efficiency of the cryosorption process is, above other things, mainly influenced by the charcoal temperature. To get a quantitative impression of this property, the panels were equipped with various temperature sensors. As the sensors are not small enough to be fully embedded in the charcoal layer of about 1 mm thickness, they were contacted with the panel wall material and thus also affected by the substrate temperature. In this regard, the measured temperatures are only an indication of charcoal temperature, not an exact determination. However, it should be tried to operate the sensors in such a way that they can be compared satisfactorily with the charcoal situation. The strategy how to achieve this goal is outlined in the following section, using the Fe-Rh sensors as a typical example. The number of aluminium foil layers, which we use in order to minimize the impact of thermal radiation coming from the LN_2-annular tank onto the temperature sensors, is used as a parameter to influence the heat transfer situation at the sensor.

The thermal situation ruling at the charcoal and the sensor is considered similar, if the temperature effect due to the surface related heat flux $\dot{q}$, which is predominantly caused by thermal radiation coming from the LN_2-cooled annular rig, is comparable. Introducing a surface related heat flux function $\dot{\Phi}$ to describe the losses into the substrate, the energy balances for the sensor S and the charcoal layer C, respectively are as follows:

$$\dot{Q}_c \equiv \dot{q}_c \cdot A_c = \frac{\Delta H_c}{\Delta t} + \dot{\Phi}_c \cdot A_c \quad , \tag{B1}$$

$$\dot{Q}_S \equiv \dot{q}_S \cdot A_S = f \cdot \left(\frac{\Delta H_S}{\Delta t} + \dot{\Phi}_S \cdot A_S \right) \quad , \tag{B2}$$

whereby A denotes the surface areas for heat transfer, and ΔH the enthalpy change in the time Δt; the factor f describes the efficiency of the thermal radiation shielding, which is, approximately, directly related to the number N of superinsulation layers, which are used as thermal radiation shielding for the sensors [36] :

$$f \approx \frac{1}{N+1} \quad . \tag{B3}$$

Incorporating the requirement of

$$\dot{q}_c = \dot{q}_S \tag{B4}$$

and coupling the two balance equations gives the following equation for the determination of the appropriate number of superinsulation layers N :

$$N = \left(\frac{\Delta H_S}{\Delta t \cdot A_S} + \dot{\Phi}_S \right) \cdot \left(\frac{1}{\frac{\Delta H_c}{\Delta t \cdot A_c} + \dot{\Phi}_c} \right) - 1 = \frac{\left(\Delta H_S + \dot{\Phi}_S \cdot \Delta t_S \cdot A_S \right) \cdot A_c}{A_S \cdot \left(\Delta H_c + \dot{\Phi}_c \cdot \Delta t_c \cdot A_c \right)} - 1 \quad . \tag{B5}$$

For evaluation of the worst case influence, we set the heat loss to zero, i.e. the whole thermal radiation energy input is used for the generation of measurement error. If we express the enthalpy change by means of the specific heat capacity and the masses m, which have to be heated, we finally arrive at

$$N = \frac{m_S \cdot \int_S c_S \cdot dT}{m_c \cdot \int_c c_c \cdot dT} \cdot \frac{A_c}{A_S} - 1 \qquad \text{(B6)}$$

With the estimated values:

mass of charcoal on one panel side	m_c = 150 g,
mass of one Fe-Rh sensor	m_S = 0.5 mg,
one panel side area	A_c = 0.175 m^2,
mean surface area of Fe-Rh sensor cylinder, incl. the foils	$A_S = 3 \cdot 10^{-7}$ m^2,
mean specific heat between 5 and 10 K (carbon) [37]	c_c = 0.2 J/kg/K,
mean specific heat between 5 and 10 K (glass) [38]	c_S = 0.6 J/kg/K,

we finally get an estimated theoretical value for the necessary number of superinsulation layers

N in the worst case of operation: N=5.

In the practical completion of the radiative shielding, we found it very difficult and clumsy to fix 5 layers of aluminium foil for each sensor in such a way that they do not contact each other. For this reason, we used only three layers as a compromise.

C Additional data for warm gas heating

As discussed in chapter 6.4, the heating behaviour of the cryopanel when heated by forced GHe flow is characterised best by the channel which is directly above the inlet section of the panel. This channel is described by the temperature measurement positions T 140, T141, T143, T146 (panel I) and T240, T243, T246 (panel II) respectively (see Figure 6). In the following, the relevant heating curves are given for all tests done. At the end of this section, the heating times up to 80, 90 or 100 K are listed in tabular form.

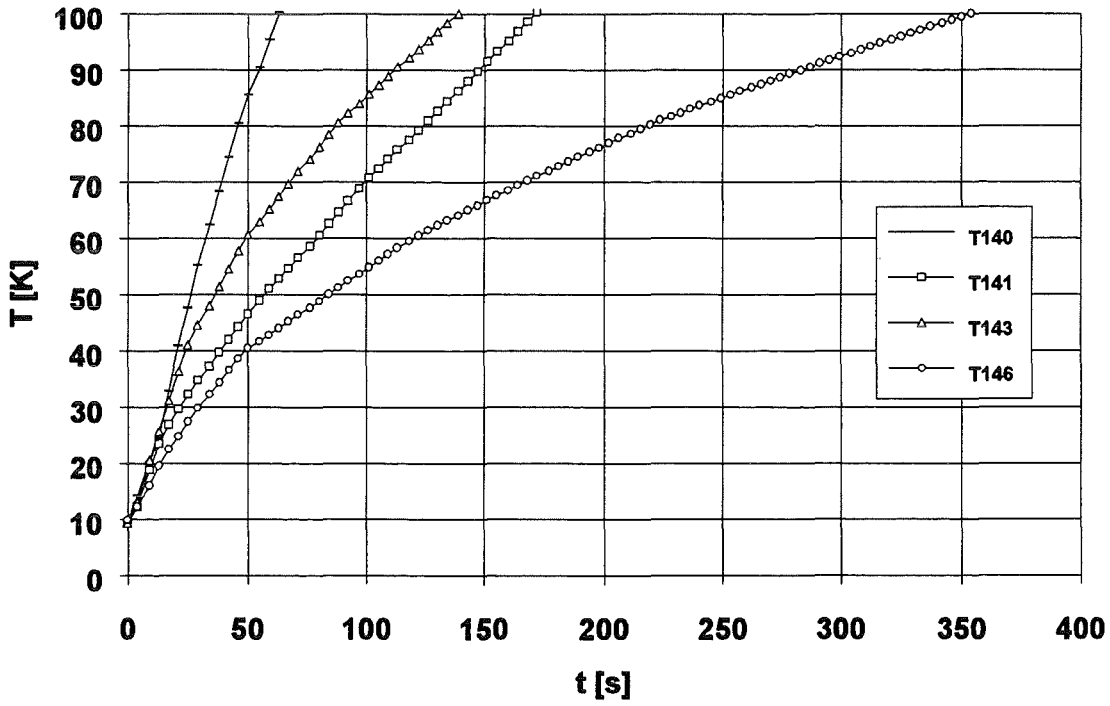

Figure C1: Heating curves for 0.27 g/s GHe flow rate (unloaded panel):

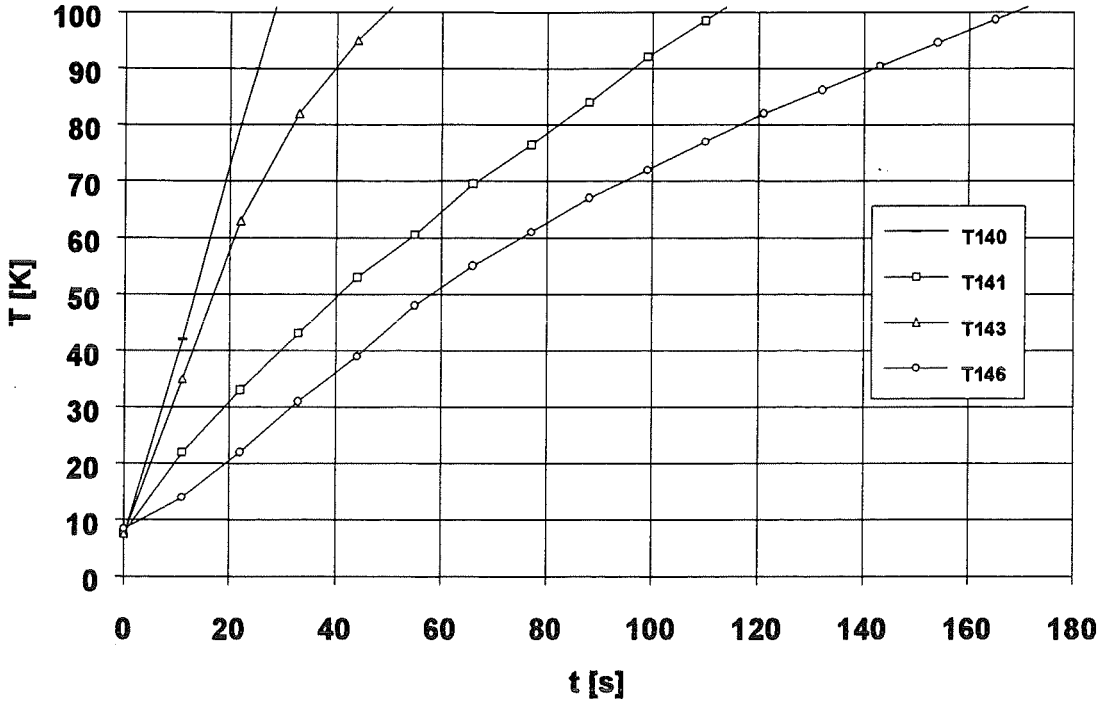

Figure C2: Heating curves for 1.1 g/s GHe flow rate (unloaded panel).

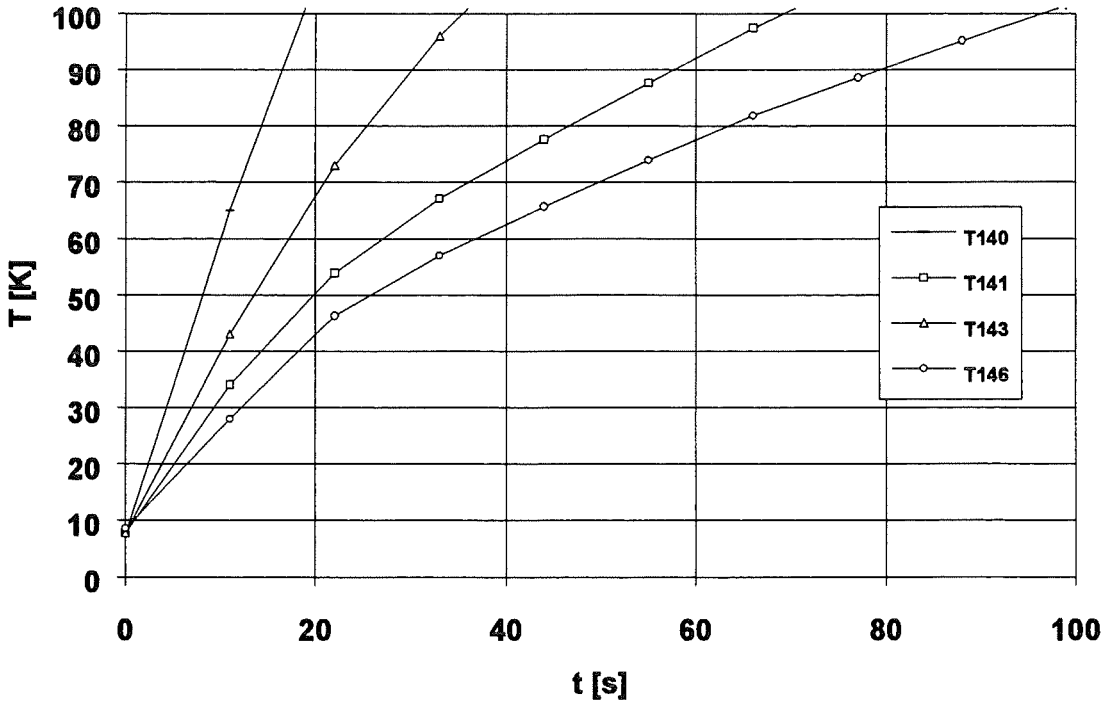

Figure C3: Heating curves for 1.9 g/s GHe flow rate (unloaded panel).

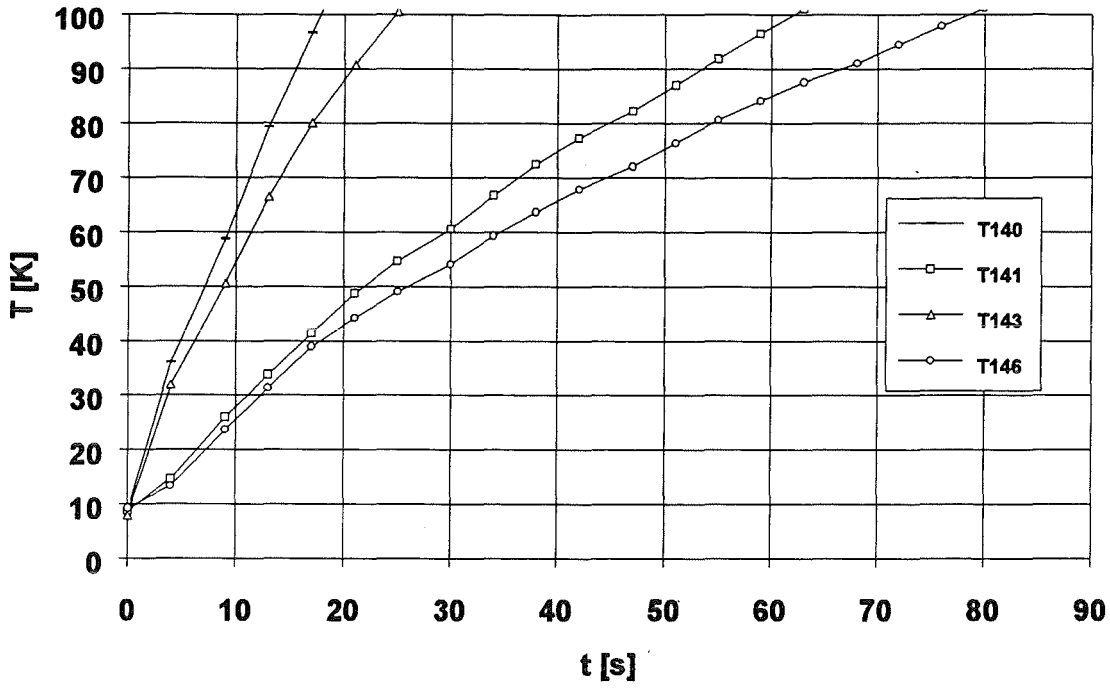

Figure C4: Heating curves for 2.9 g/s GHe flow rate (unloaded panel).

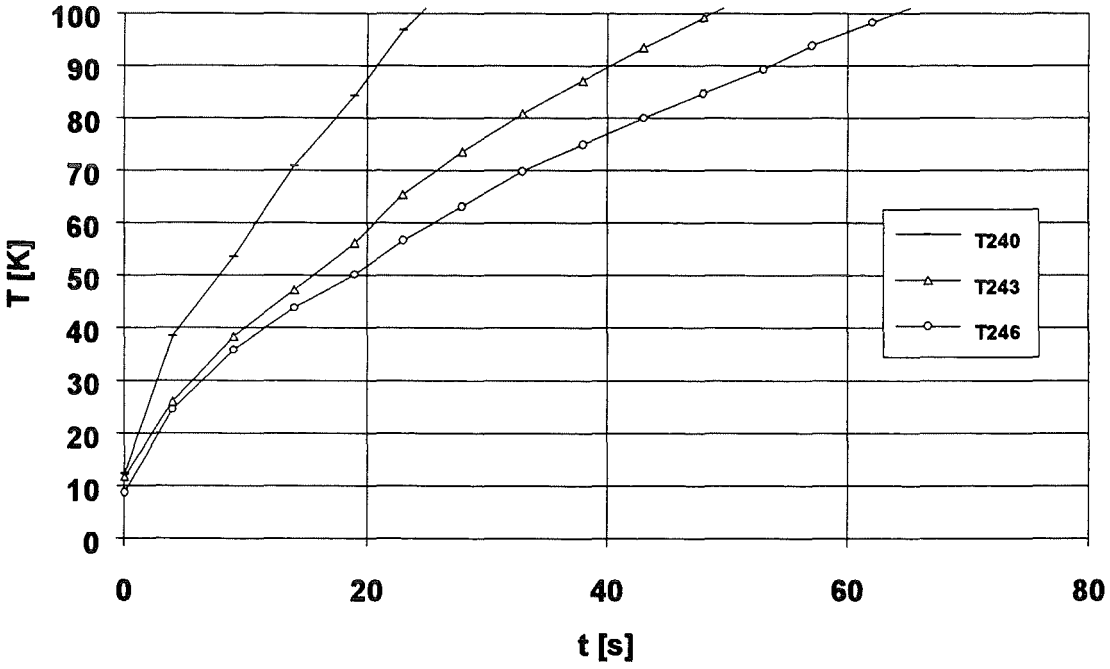

Figure C5: Heating curves for 3.8 g/s GHe flow rate (unloaded panel).

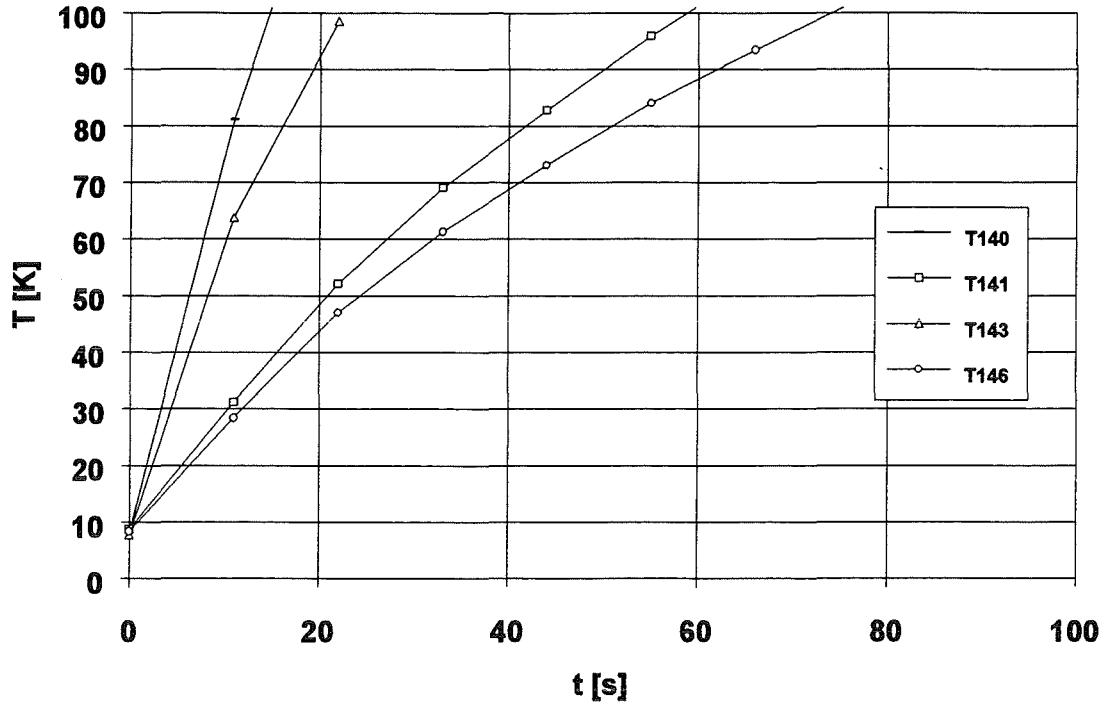

Figure C6: Heating curves for 4.0 g/s GHe flow rate (unloaded panel).

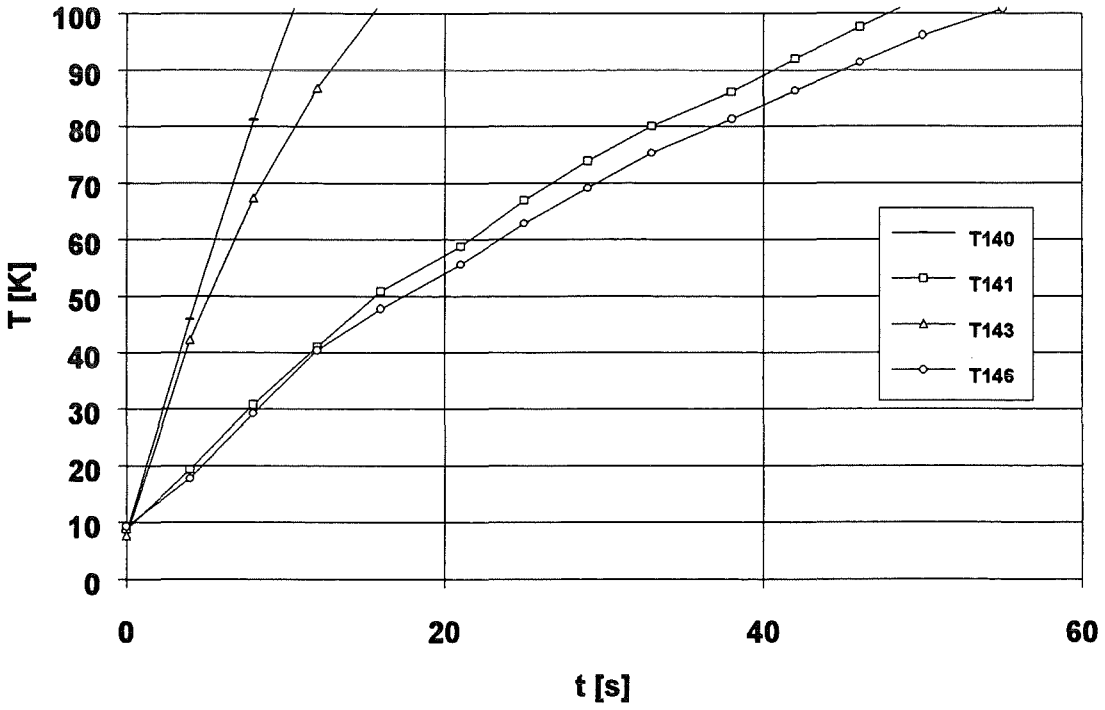

Figure C7: Heating curves for 5.1 g/s GHe flow rate (unloaded panel).

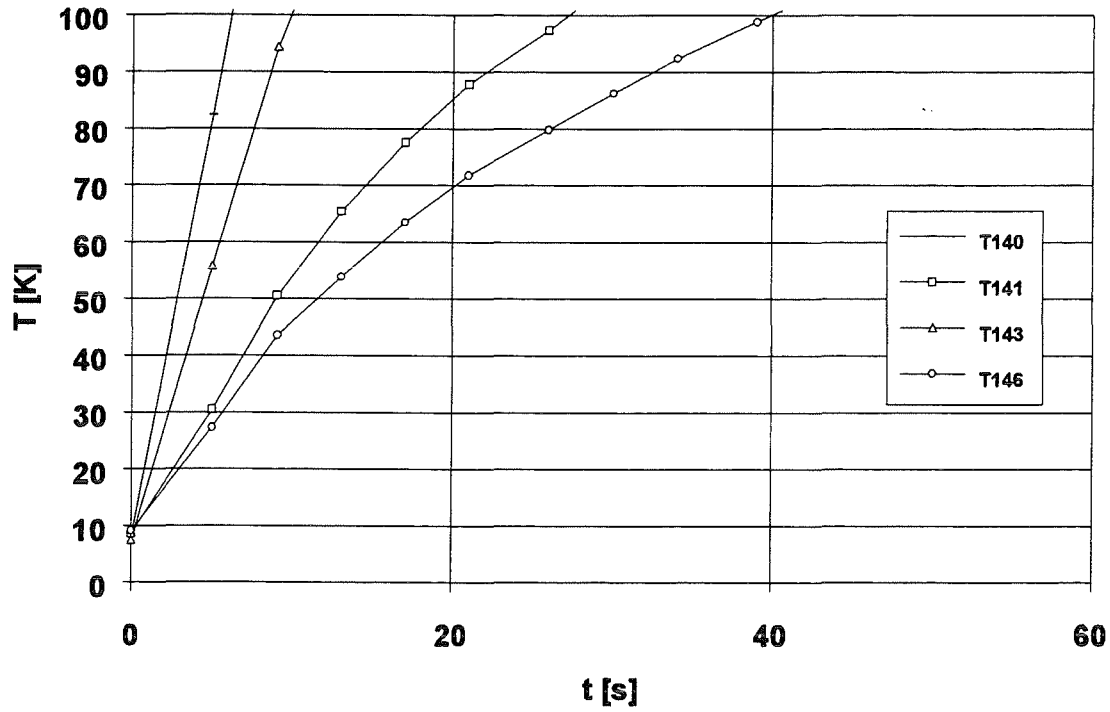

Figure C8: Heating curves for 5.0 g/s GHe flow rate (loaded panel).

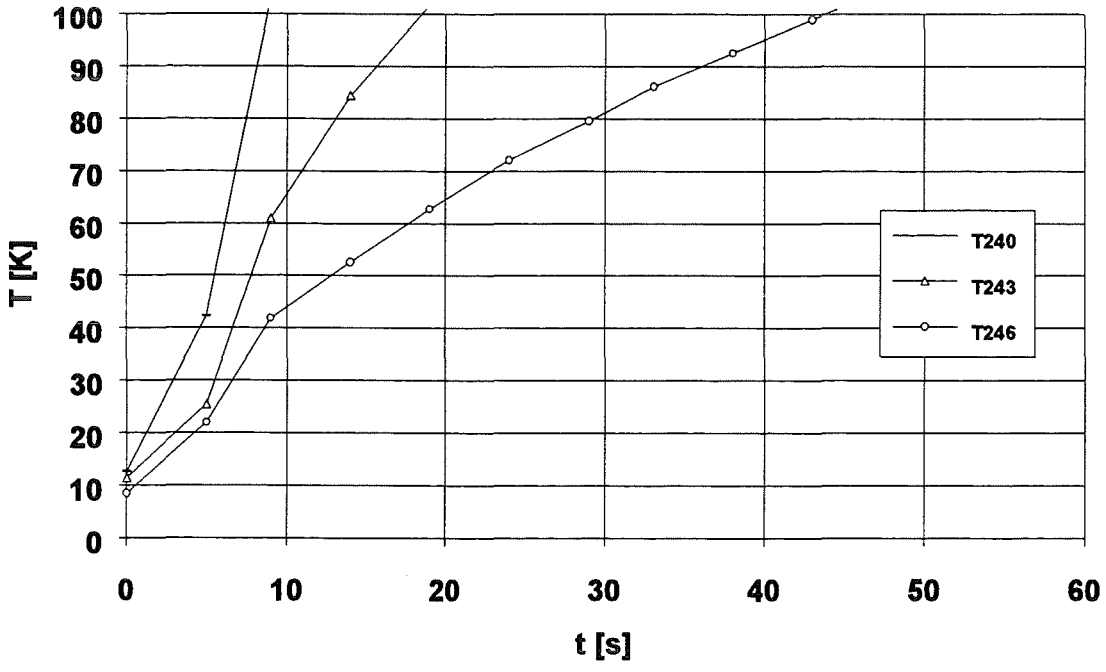

Figure C9: Heating curves for 3.8 g/s GHe flow rate (loaded panel).

Table C1: Summarized heating times for GHe method related to representative positions at the panel for heating up to 80, 90 and 100 K, respectively.

mass flow [g/s]	end temperature [K]	heating time [s] T140/240	T141/241	T143/243	T146/246
LOADED					
0.27	80	46	123	88	215
	90	54	148	112	283
	100	63	171	139	354
1.1	80	22	82	32	116
	90	25	96	40	142
	100	28	113	49	168
1.9	80	14	46	25	63
	90	16	57	27	79
	100	18	69	35	96
2.9	80	13	44	17	54
	90	15	53	21	66
	100	17	62	25	78
3.8	80	17	-	33	43
	90	21	-	40	53
	100	24	-	48	64
4.0	80	11	42	16	51
	90	12	49	19	61
	100	14	58	22	74
5.1	80	8	33	10	36
	90	9	40	13	44
	100	10	47	15	54
UNLOADED					
5.0	80	5	18	7	26
	90	5	22	7	32
	100	6	27	10	40
3.8	80	7	-	13	27
	90	7	-	16	36
	100	9	-	18	43

D An easy-to-use model for the estimation of heating curves

In this section, a simple model shall be derived, which can be used to predict heating and cooling curves of a solid by forced convection. For this reason the temperature, which is in general a complex function of position coordinate and time, is considered to vary only with time, i.e. the temperature distribution within the solid at any instant is uniform: the whole solid is described with an average caloric temperature. The application of such a lumped system analysis is limited to heat transfer problems characterised by small Biot numbers, i.e. to cases with a short heat transfer path.
The analysis of unsteady heat flow under such an assumption greatly simplifies the problem of determining the solid temperature curve.

Consider a solid, whose temperature at the beginning of the experiment is known. At this very beginning (time t=0) a forced convection heat transfer is established. The start temperature (at t=0) at the entrance of the convection fluid and of the solid is known. Wanted are the temperature curves of the convection fluid and the solid during the experiment. An additional heat source in the solid is also to consider.
The following derivation is referring to the fast heating of one typical quilted panel channel P (mass m_P, specific heat capacity c_P, length L) , which is heated (typically from 5 K to 90 K) by a forced flow of GHe (mass flow $\dot{m}_{He}$, specific heat capacity $c_{p,He}$). The heat source expression $\dot{\Psi}$ may, for example, be used for the consideration of additional electric heating or a (constant) thermal radiation contribution from the LN_2-cooled panel environment. Wanted is the time behaviour of the average temperature of the panel chanel $T_P\langle t\rangle$ and the helium temperature $T_{He}\langle z,t\rangle$ as a function of position z and time t.

A thermal energy balance (non steady-state)

$$\dot{E}_{in} = \dot{E}_{out} + \frac{dE}{dt} \qquad \text{(D1)}$$

for the helium stream on a differential segment dz of the channel with cross section area A_{ch} and circumference U_{ch}, considering an ammount of thermal power exchange $d\dot{Q}$ between helium and the channel mass gives:

$$\dot{H}_{He}\langle z,t\rangle = \dot{H}_{He}\langle z+dz,t\rangle + d\dot{Q} + \frac{\partial}{\partial t} dH_{He}\langle z,t\rangle \quad . \qquad \text{(D2)}$$

The use of a Taylor series for the enthalpy flow

$$\dot{H}_{He}\langle z+dz,t\rangle = \dot{H}_{He}\langle z,t\rangle + \frac{\partial \dot{H}_{He}\langle z,t\rangle}{\partial z} dz \qquad \text{(D3)}$$

yields

$$d\dot{Q} = -\frac{\partial \dot{H}_{He}\langle z,t\rangle}{\partial z} dz - \frac{\partial}{\partial t} dH_{He}\langle z,t\rangle \quad . \qquad \text{(D4)}$$

Inserting the enthalpy expressions

$$\dot{H}_{He} = \dot{m}_{He} \cdot c_{p,He} \cdot T_{He} \quad , \qquad \text{(D5)}$$

$$H_{He} = m_{He} \cdot c_{p,He} \cdot T_{He} \quad , \qquad \text{(D6)}$$

$$dH_{He} = dm_{He} \cdot c_{p,He} \cdot T_{He} = \rho_{He} \cdot A_{ch} \cdot dz \cdot c_{p,He} \cdot T_{He} \qquad \text{(D7)}$$

and the kinetic equation (heat transfer coefficient h) for the transferred heat between helium gas and the panel channel P

$$d\dot{Q} = h \cdot dA_W \cdot \left(T_{He}\langle z,t\rangle - T_P\langle t\rangle\right) \quad , \qquad \text{(D8)}$$

with the differential channel wall area

$$dA_W = U_{ch} \cdot dz \qquad \text{(D9)}$$

along the segment dz yields the differential equation

$$h \cdot dz \cdot U_{ch} \cdot \left(T_P\langle t\rangle - T_{He}\langle z,t\rangle\right) = \dot{m}_{He} \cdot c_{p,He} \cdot \frac{\partial T_{He}}{\partial z} \cdot dz + c_{p,He} \cdot \rho_{He} \cdot A_{Ch} \cdot \frac{\partial T_{He}}{\partial t} \cdot dz \,. \qquad \text{(D10)}$$

For high mass flows, we can neglect the derivative of the helium temperature with respect to time along the segment dz. Thus, by integration between inlet and variable position z we arrive at the final equation to calculate the helium temperature as a function of position for a fixed time t:

$$\frac{h \cdot U_{ch}}{\dot{m}_{He} \cdot c_{p,He}} \cdot \int_0^z dz = \int_{T_{He}\langle z=0,t\rangle}^{T_{He}\langle z,t\rangle} \frac{dT_{He}}{T_p - T_{He}} \quad ; \tag{D11}$$

the lower integration boundary of T_{He} can be given as a function of time. In the case of our experiments it is kept constant for all times t:

$$T_{He}\langle z=0,t\rangle = T_{He,in} = const. \quad . \tag{D12}$$

Evaluation of the integrals yields:

$$T_{He}\langle z,t\rangle = T_P\langle t\rangle + \left(T_{He,in} - T_P\langle t\rangle\right) \cdot \exp\left\{-\frac{h \cdot U_{ch}}{\dot{m}_{He} \cdot c_{p,He}} \cdot z\right\} \quad . \tag{D13}$$

To derive the temperature curve for the panel channel, we start with the macroscopic energy balance for panel channel plus helium:

$$\dot{H}_{He,in} + \dot{\Psi} = \dot{H}_{He,out} + \frac{dH_P}{dt} \quad . \tag{D14}$$

Inserting the enthalpy expressions analogously to (D5) to (D7) we get

$$\dot{m}_{He} c_{p,He} \cdot \left(T_{He}\langle z=L,t\rangle - T_{He,in}\right) = \dot{\Psi} - m_P \cdot c_P \cdot \frac{dT_P}{dt} \quad . \tag{D15}$$

If we now couple this equation with equation (D13) for T_{He}, we obtain a first order linear differential equation for the determination of $T_P\langle t\rangle$:

$$\begin{aligned} &m_P \cdot c_P \cdot \frac{dT_P}{dt} + \dot{m}_{He} \cdot c_{p,He} \cdot \left(1 - \exp\left\{-\frac{h \cdot U_{ch}}{\dot{m}_{He} \cdot c_{p,He}} \cdot L\right\}\right) \cdot T_P = \\ &= \dot{\Psi} + \dot{m}_{He} \cdot c_{p,He} \cdot \left(1 - \exp\left\{-\frac{h \cdot U_{ch}}{\dot{m}_{He} \cdot c_{p,He}} \cdot L\right\}\right) \cdot T_{He,in} \end{aligned} \quad . \tag{D16}$$

Incorporating the initial condition

$$T_P\langle t=0\rangle = T_{P,0} = given \quad , \tag{D17}$$

the final solution can be formulated as follows:

$$T_P\langle t\rangle = \left(T_{P,0} - C\right)\cdot \exp\{\omega t\} + C \qquad \text{with}$$

$$C = \frac{\dfrac{\dot{\Psi}}{\dot{m}_{He}\cdot c_{p,He}} + T_{He,in}\cdot\left(1-\exp\left\{-\dfrac{h\cdot U_{ch}}{\dot{m}_{He}\cdot c_{p,He}}\cdot L\right\}\right)}{1-\exp\left\{-\dfrac{h\cdot U_{ch}}{\dot{m}_{He}\cdot c_{p,He}}\cdot L\right\}} \qquad \text{and} \qquad \text{(D18)}$$

$$\omega = -\frac{\dot{m}_{He}\cdot c_{p,He}}{m_P\cdot c_P}\cdot\left(1-\exp\left\{-\frac{h\cdot U_{ch}}{\dot{m}_{He}\cdot c_{p,He}}\cdot L\right\}\right) .$$

If the thermal radiation term $\dot{\Psi}$ can be neglected, as it is the case for the GHe tests, the expression C is identical with $T_{He,in}$.

The heat transfer coefficient h can be calculated using the standard formulae for laminar and turbulent heat transfer, respectively, necessitating the calculation of the dimensionless Reynolds, Nusselt and Prandtl numbers. The evaluation of these formulae has to be done iteratively, as, for their calculation the helium properties have to be used at the mean temperature between inlet and outlet, but the outlet temperature is one of the wanted results. The dimensionless numbers for non circular cross sections are defined with the hydraulic diameter d_h (c.f. Figure 5):

$$d_h = \frac{4\cdot A_{ch}}{U_{ch}} \qquad \text{(D19)}$$

The cross section area of the quilted panel channel is approximately 62 mm^2, the circumference is about 75 mm, thus yielding a hydraulic diameter of d_h=6.6 mm.

These formulae show how the GHe fast heating of cryopanels with fixed geometry is influenced by the helium mass flow and the inlet temperature. The influence of helium pressure is only very weak, because in the interesting temperature range, very much away from the critical state, helium behaves almost like an ideal gas.

An impression of the calculated panel heating performance is given in Figure D1. It shows the calculated times for heating the TITAN cryopanel, consisting of seven quilted flow channels, from 5 to 90 K as a function of total mass flow and with the helium inlet temperature as parameter.

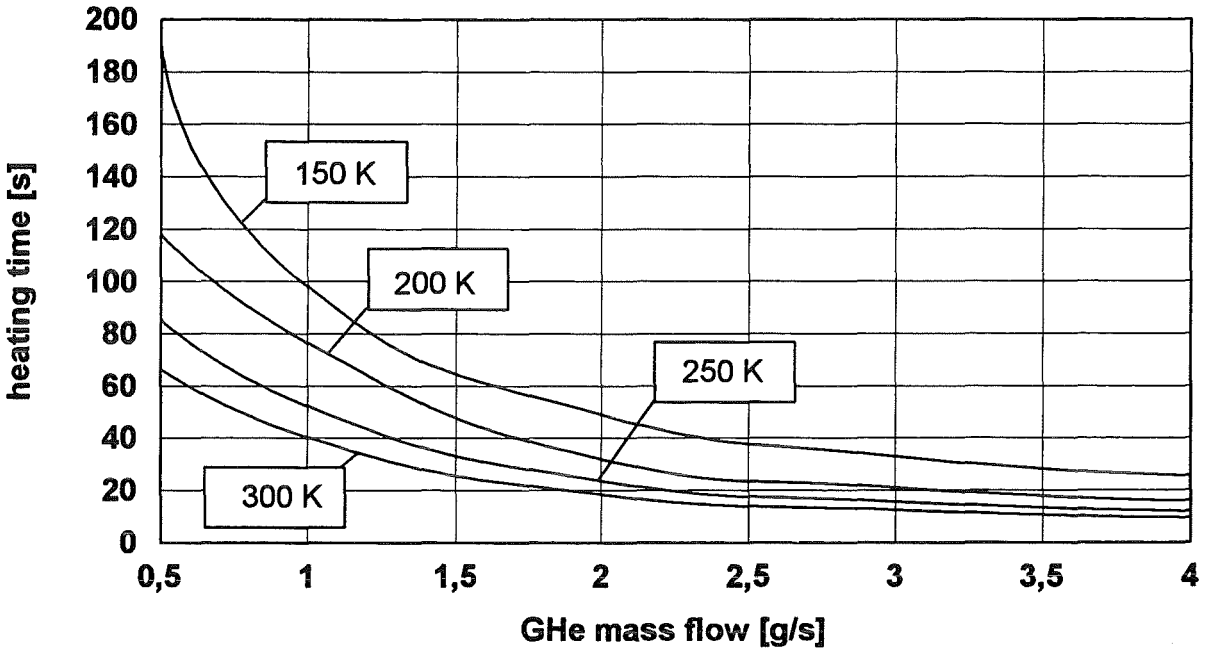

Figure D1: Calculated heating times of the TITAN cryopanel as a function of the GHe mass flow and the helium inlet temperature.

E Additional data for electric heating

In Figure 24, paragraph 6.5 the heating curves for 2390 W electric power input are presented for the three different modes investigated (unloaded, full; unloaded controlled; loaded, controlled). In the present annex, the results for the experiments at 1250 and 3070 W are also given.

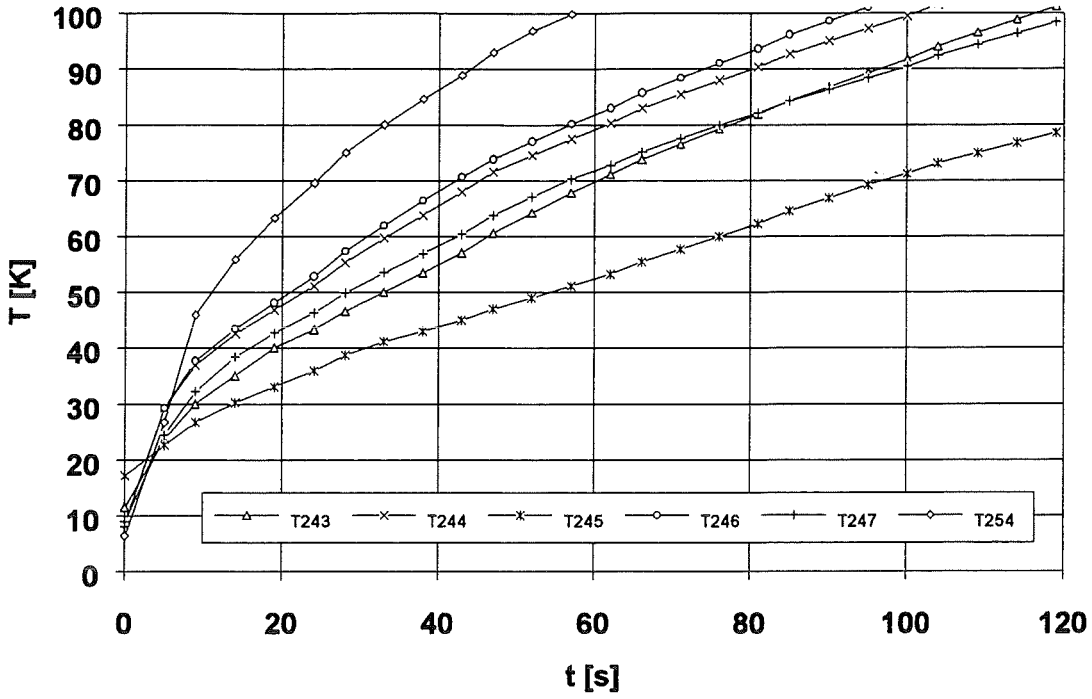

Figure E1: Heating curves for 1250 W electric power (unloaded panel, full heating).

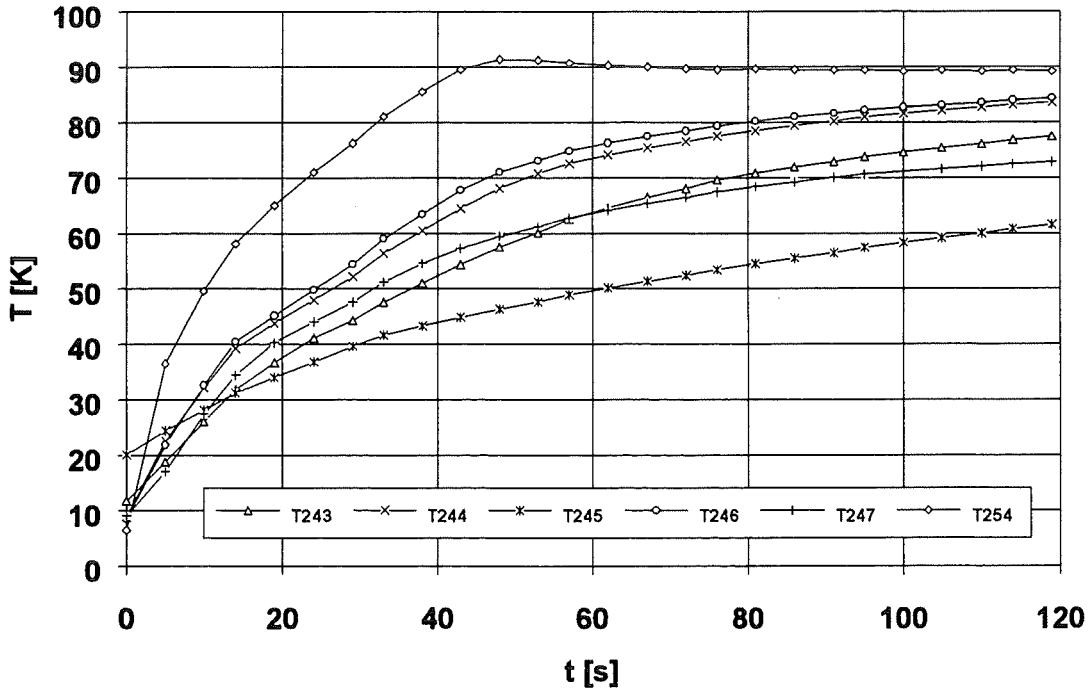

Figure E2: Heating curves for 1250 W electric power (unloaded panel, controlled heating).

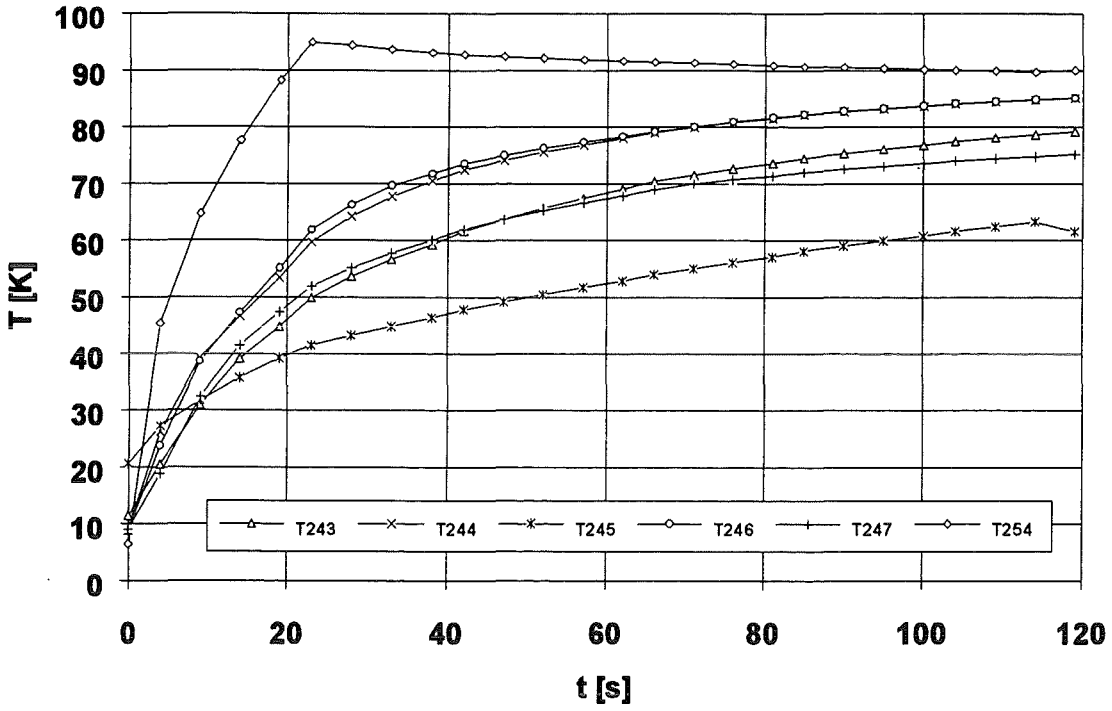

Figure E3: Heating curves for 3070 W electric power (unloaded panel, controlled heating).

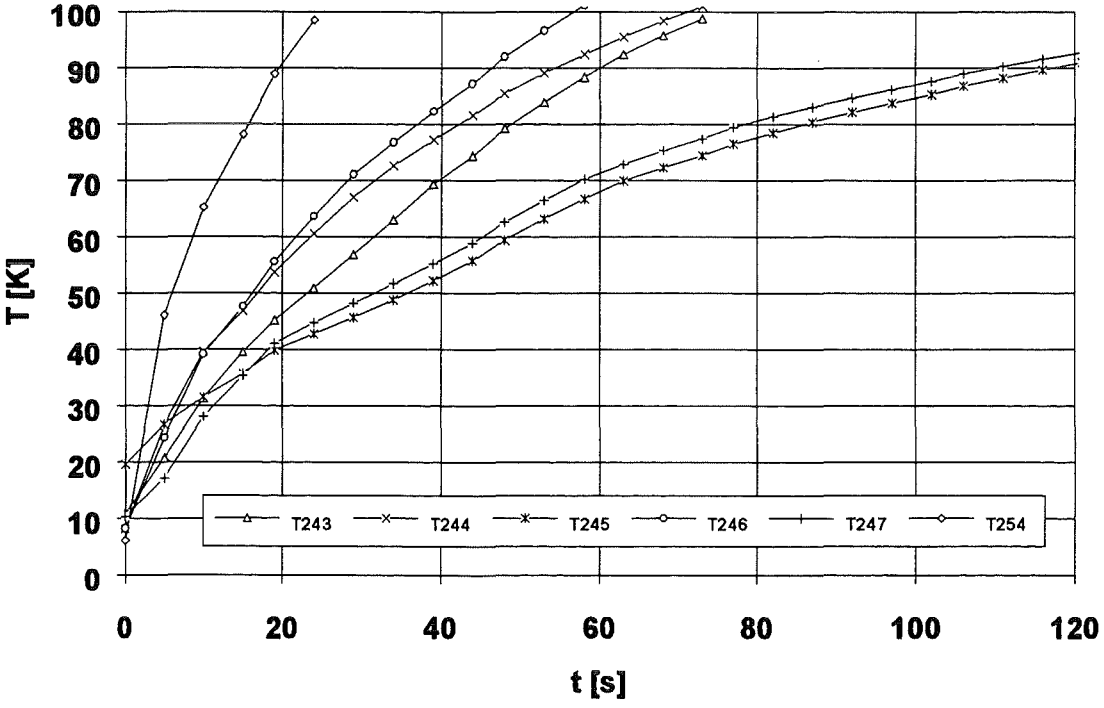

Figure E4: Heating curves for 3070 W electric power (unloaded panel, full heating).

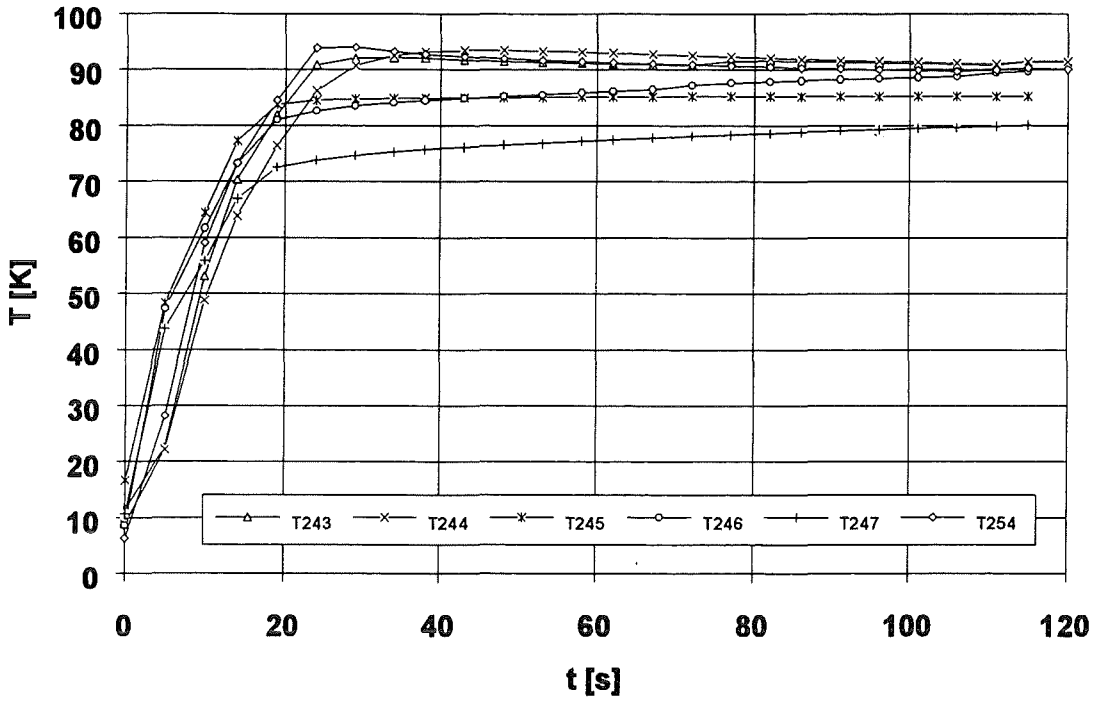

Figure E5: Heating curves for 3070 W electric power (loaded panel, controlled heating).